Investigations on Micronozzle for Satellite Propulsion and Gas Mixture Separation

A thesis submitted

in partial fulfillment for the award of the degree of

Doctor of Philosophy

by

Manu K Sukesan

Department of Aerospace Engineering

Indian Institute of Space Science and Technology

Thiruvananthapuram, India

December 2023

Certificate

This is to certify that the thesis titled ***Investigations on Micronozzle for Satellite Propulsion and Gas Mixture Separation*** submitted by **Manu K Sukesan**, to the Indian Institute of Space Science and Technology, Thiruvananthapuram, in partial fulfillment for the award of the degree of **Doctor of Philosophy** is a bona fide record of the original work carried out by him under my supervision. The contents of this thesis, in full or in parts, have not been submitted to any other Institute or University for the award of any degree or diploma.

Dr. Shine S R
Research Supervisor,
Associate Professor,
Department of Aerospace Engineering,
IIST

Dr. Deepu M
Professor & Head,
Department of Aerospace Engineering,
IIST

Place:IIST, Thiruvananthapuram
Date: December 2023

Declaration

I declare that this thesis titled ***Investigations on Micronozzle for Satellite Propulsion and Gas Mixture Separation*** submitted in partial fulfillment for the award of the degree of **Doctor of Philosophy** is a record of the original work carried out by me under the supervision of **Dr. Shine S R**, and has not formed the basis for the award of any degree, diploma, associateship, fellowship, or other titles in this or any other Institution or University of higher learning. In keeping with the ethical practice in reporting scientific information, due acknowledgments have been made wherever the findings of others have been cited.

Place: Thiruvananthapuram
Date: December 2023

Manu K Sukesan
(SC19D029)

This thesis is dedicated to my parents . . .

Acknowledgements

I would like to express my sincere gratitude and appreciation to all those who have supported and contributed to the completion of this Ph.D. thesis.

First and foremost, I am deeply indebted to my supervisor, Dr. Shine S. R, for his unwavering guidance, invaluable insights, and constant encouragement throughout this research endeavor. His expertise and mentorship have been instrumental in shaping the direction of my work and enhancing its quality.

I extend my heartfelt thanks to the members of my Ph.D. committee, Dr. Aravind Vaidyanathan, Dr. Pradeep Kumar, Dr. Mahesh S, and Dr. E. Natarajan, for their critical feedback, constructive suggestions, and thoughtful input during the evaluation of this project. Their expertise in their respective fields has significantly enriched my research.

I would also like to acknowledge the support and assistance provided by the faculty members of aerospace Engineering at IIST. Their commitment to academic excellence and dedication to nurturing young researchers have played a pivotal role in my academic growth.

My gratitude also goes to the Indian Institute of Space Science and Technology for providing access to their state-of-the-art facilities, resources, and research materials. The institution's infrastructure and technical support have been essential in conducting experiments and gathering data for this thesis.

I express my sincere gratitude to Dr. Sooraj, Prakash, and Sarath for their invaluable assistance in manufacturing the micronozzle. Their expertise and dedication played a vital role in the success of this project.

I am also thankful to Yadhu Krishna, Anbarashan, Dhinesh, Sujin, Bipin, and Vinil for their significant contributions to conducting the experiments. Their support and collaboration were essential in gathering and analyzing the data, leading to meaningful insights and findings.

I would like to thank my colleagues and fellow Ph.D. students Hari, Chithra, Ashok, Sarath, Nibin, Nithin, Sajith, Shyam, Shiyas, Prabith, Ajin, Anjuna, Aswathy, Soumya and Abhijith for their camaraderie, stimulating discussions, and intellectual collaboration. Their diverse perspectives and shared experiences have contributed significantly to the development of my ideas.

To Renjith, Resmi, James, Jerin, and Nikhil—your unwavering friendship and support have been a beacon of light throughout my doctoral odyssey. Together, we have scaled the peaks of knowledge, shared laughter, and camaraderie amidst exhilarating trekking adventures, nourished each other during shared meals, and embarked on enriching journeys to uncharted realms. Your presence has turned this academic pursuit into an unforgettable symphony of cherished memories.

Lastly, I want to express my heartfelt appreciation to my family and friends for their unwavering support, patience, and understanding throughout my Ph.D. journey. Their constant encouragement and belief in my abilities have been a source of strength and motivation.

In conclusion, I am indebted to all those mentioned above, as well as countless others who have contributed to my academic and personal growth. Their support, encouragement, and expertise have played a pivotal role in the successful completion of this Ph.D. thesis.

Manu K Sukesan

Abstract

Micronozzles operating with vacuum exit conditions find applications in satellite propulsion systems and aerodynamic separation processes. Research on flow characteristics of micronozzles is currently dominated by micro-thruster applications, followed by its use for gas mixture separation. Uniformity in the flow structure to obtain optimum thruster performance is the prime objective of the former, while the latter demands highly non-uniform species distribution of the flowing mixture. The literature review reveals that as the length scales are of the order of micrometres, carefully built apparatus and measurement systems are required to obtain data reasonably. Due to the scarcity of experimental data concerning flow parameters, a new experimental arrangement is developed using Interferometric Rayleigh scattering to measure the exit velocity of the nozzle. The generated experimental data is used along with literature data to validate the computational models developed in the current work. Flow regimes from the nozzle throat to the nozzle exit can change from near-continuum to rarefied, and therefore both continuum and kinetic approaches have been used for computational simulations. The classical N-S with linear slip model, DSMC method, and a hybrid N-S/DSMC based on the continuum breakdown concept are employed for the numerical simulations. The effect of divergence half angle, throat depth, and expansion ratio are analysed in detail to address the conflicting findings reported in the present literature. Results show an optimum divergence angle and length, maximizing the performance for a specific operating condition and nozzle size. It is noted that the inconsistencies in the literature are mainly due to exploratory efforts of small data sets. Re is very low as the nozzle size decreases to the nano-scale, and the subsonic layer fully occupies the divergent nozzle section even at very high-pressure differences. The results show that the performance is significantly influenced by the wall's thermal conditions. The study highlights the differences in flow behaviour between micro and nano-scale nozzles at various operating conditions. Based on numerical data obtained in this work, a new correlation is proposed to predict the thrust per unit width for micronozzles. A numerical investigation of the aerodynamic separation process associated with converging-diverging 2-D planar micronozzles shows that the enrichment of the heavier/lighter species near the axis/wall is significantly affected by the nozzle size. The aerodynamic separation effect is created mainly by (i) streamwise separation produced by the velocity slip between species

and (ii) lateral separation created by the curving of streamlines. The streamwise separation effect is higher in smaller nozzles creating heavier species concentration at the axis. The lateral separation effect increased with increased throat size. The result is a higher, lighter species concentration in the peripheral regions of the bigger nozzle. The lateral separation effect is found to be influenced by the nozzle divergent section shape. The divergent section with trumpet shape, truncated bell, and conical with high divergence are preferred for higher species separation performance. The results show that the presence of a heavier carrier gas deteriorates the separation performance. The backpressure conditions at the nozzle exit play a significant role in the curvature of streamlines at the nozzle lip. For curved micronozzles, streamwise separation, lateral separation, mass diffusion, and thermal diffusion can affect the separation performance. Further influencing the separation performance are factors such as the nozzle shape, wall temperature conditions, molecular mass ratio, and inlet mole fraction of the species. The results of this research will aid in the creation of improved designs for micronozzles utilized in satellite propulsion and aerodynamic separation processes.

Contents

List of Figures

List of Tables

Abbreviations

BGK	Bhatnagar-Gross-Krook
CLL	Cercignani Lampis Lord
CT	Computerized Tomography
DSMC	Direct Simulation Monte Carlo
EDM	Electrical Discharge Machining
ESBGK	Ellipsoidal statistical BGK
FP	Fokker Plank
HPIV	Holographic PIV
ISBT	Intelligent SBT
L-B	Larsen-Borgnakke
LD	Low Diffusion
LIF	Laser Induced Fluorescence
LVDT	Linear Variable Differential Transformer
MEMS	Microelectromechanical Systems
MTV	Particle Tagging Velocimetry
NEAC	Normal Energy Accommodation coefficient
N-S	Navier Stokes
NTC	No Time Counter
PIV	Particle Image Velocimetry
PSMF	Pressure Sensitive Molecular Film
PSP	Pressure Sensitive Paint
PTV	Particle Tracking Velocimetry
SBT	Simplified Bernoulli Trial
SPIV	Stereo PIV
TAS	Transient Adaptive Sub cell
TC	Time Counter
TMAC	Tangential Momentum Accommodation Coefficient

VHS	Variable Hard Sphere
VIPA	Virtually Imaged Phased Array
VSC	Virtual sub cell
VSS	Variable Soft Sphere

Nomenclature

A	=	separation factor
AR	=	aspect ratio of the throat,h/w
$\vec{c}$	=	mean thermal speed, ms^{-1}
c_r	=	relative velocity, ms^{-1}
D_{ab}	=	Mass diffusion coefficient, m^2/s
d	=	diameter, *m*
ER	=	Expansion ratio, h_e/h_t
E	=	total energy, $J\ Kg^{-1}$
$\vec{F}$	=	external force acting on the molecule, *N*
f	=	velocity distribution function
g	=	gravitational acceleration, $9.81\ ms^{-2}$
H	=	enthalpy, $J\ Kg^{-1}$
h	=	height, *m*
I_s	=	specific impulse, *s*
K_B	=	Boltzmann constant, $m^2\ kg\ s^{-2}\ K^{-1}$
K_c	=	thermal conductivity, $Wm^{-1}\ K^{-1}$
Kn	=	Knudsen number
L	=	nozzle length, *m*
L_c	=	convergent section length, *m*
L_c	=	characteristic length length, *m*
L_d	=	divergent section length, *m*
L_{bottom}	=	bottom wall divergent length, *m*
L_{top}	=	top wall divergent length, *m*
M	=	Mach number
$\dot{m}$	=	mass flow rate Kgs^{-1}
N	=	Number of molecules
n	=	number density, m^{-3}
$\vec{n}$	=	normal direction

P = static pressure, *Pa*

P_0 = settling chamber pressure, *kPa*

P_b = receiver chamber pressure, *kPa*

Pr = Prandtl number

Re = Reynolds number

R = specific gas constant, *J* kg^{-1} K^{-1}

R_t = Radius of nozzle throat, *m*

r = radius, *m*

T = temperature, *K*

T_h = thrust, *N*

t = time, *s*

u = axial velocity, ms^{-1}

V = velocity vector, ms^{-1}

V_c = cell volume, m^3

v = y velocity, ms^{-1}

w = width, *m*

X = mole fraction fraction

x = axial distance, *m*

θ_h = Heavy fraction partial cut

θ_l = Light fraction partial cut

Greek

γ = ratio of specific heat

θ = Angle, $^\circ$

λ = mean free path for the gas,*m*

μ = dynamic viscosity,$kgm^{-1}s^{-1}$

ρ = density, kgm^{-3}

σ = diffuse reflection fraction at the wall

σ = collision cross section,m^2

σ_T = thermal accommodation coefficient

σ_u = tangential momentum accommodation coefficient

τ = viscous stress tensor, *Pa*

Subscripts

Ar	=	Argon
c	=	cell
d	=	divergent
e	=	nozzle exit
g	=	gas
He	=	Helium
i	=	nozzle inlet
$st,0$	=	stagnation
t	=	throat
w	=	wall

Chapter 1
Introduction

This study aims to optimize micronozzle designs for satellite propulsion and species separation applications by examining various geometrical and flow parameters and their impact on micronozzle performance. This research expands the investigation to include micronozzle clusters for thruster applications and the species separation analysis from linear nozzles with different divergent shapes to curved nozzles. The ultimate goal is to improve the performance of micronozzles in satellite thrusters and species separation, contributing to advancements in micro propulsion systems.

This chapter focuses on the definition of a micronozzle and its differentiation from conventional nozzles. The different shapes of micronozzles currently in use are reviewed, and an overview of their various applications is provided. Additionally, the chapter discusses the research motivation and outlines the scope of the thesis.

1.1 Background

The advancements in miniaturization and microtechnology have made it possible to create micronozzle designs that can be used in various applications. Micronozzles have applications ranging from satellite propulsion to biomedical fields. The micro-propulsion system's effectiveness and performance are greatly influenced by the size, shape, and flow features of the micro nozzle. In recent years, advancements in fabrication methods have enabled the production of micronozzles with high precision and surface finish, even at extremely small sizes. The exact size range of micro nozzles can vary greatly and has not been well defined in previous studies. Micro nozzles can range in size from micrometres to millimetres, depending on the specific application and the fabrication method used.

Numerical simulations are often used to study the flow through micronozzles because

of the challenges associated with experimental measurements at such small scales. These simulations can be used to optimize the design of micronozzles and improve their performance, which can enable new applications and improve existing ones. The flow through micronozzles may be multi-scale, including continuum, slip, transition, and rarefied gas regions. Due to their small size, the flow through micronozzles is often highly influenced by viscous and rarefaction effects, which can make their behaviour difficult to predict. The development of high-performance and reliable micronozzles is a critical area of research with various potential applications. By optimizing the nozzle design and performance, researchers can unlock new capabilities and enable more efficient and effective operation of various systems.

1.2 Conventional nozzle Vs Micronozzle

There is no clear definition in the literature specifying the exact size of a nozzle that can be considered a micronozzle. However, the researchers have considered the nozzles as micronozzles when a small nozzle scale and operating conditions combine to give throat Reynolds numbers between 10 and 10^3. In this Re range, the effect of the viscous boundary layer, the transition flow characteristics, slip at the wall, etc. must be considered. At length scales on the order of micrometers, the viscous stress contribution to thrust is not negligible,and the conventional methods of thrust calculation need not be accurate. In short, micronozzles differ from traditional nozzles primarily because of the unique flow conditions they create, which are characterized by low Reynolds numbers and supersonic Mach numbers.

Conventional nozzles are simpler to fabricate than micronozzles, making them more suitable for complex shapes like bell nozzles. On the other hand, conical shapes are preferable for micronozzles, as they yield satisfactory results with simpler designs. The small size of micronozzles, comparable to the molecular free path of the flow, means that the flow characteristics are influenced by a dimensionless Knudsen number (Kn). In contrast, the larger size of conventional nozzles makes the flow independent of Kn. Micronozzles are commonly employed in applications requiring precise control and high accuracy, while conventional nozzles are utilized in situations where precision is less critical and a broader range of flow rates is necessary. Due to their smaller size and higher precision, micronozzles offer superior accuracy and control over flow compared to conventional nozzles. The major differences between micro and conventional nozzles are illustrated in Table 1.1.

Table 1.1: Comparison of micro and conventional nozzles

Micronozzle		Conventional nozzle
Conical/linear	Most preferred divergent section shape	Bell shape
10-10^3	Re_t	>>1000
Present.Flow depends Kn, High Kn	Rarefaction effects	Not present.Kn are very low
Predominant	Viscous effects	Negligible
Mostly axial	Flow direction	Significant radial flow component
Direct Simulation Monte Carlo (DSMC) method	Preferred simulation method	Continuum approach

1.3 Micronozzle shapes

An idealized nozzle profile provides the area required for the supersonic flow expansion and aligns the flow axially at the exit. In traditional designs, a bell-shaped contour accomplishes this and establishes isentropic flow conditions. The theoretical profile is obtained based on inviscid flow theory and, therefore, can't be helpful for the micronozzle flow with strong boundary layers. At the microscale, contoured nozzle fabrication is also difficult. Initial micronozzle research focused on converging-diverging nozzles (or a de Laval nozzle). This is characterized by a divergence angle θ_d for the supersonic section. Most of the studies on micronozzles are with 2D/3D conical nozzles with varying divergent sections in terms of divergence angle and length. Other shapes are aerospike designs, bell nozzles, trumpet [2], [3], and plug nozzles. Zilic et al. [4] proposed an aerospike design that could handle a wide range of ambient back pressures. A truncated spike is usually preferred in micronozzles, as most of the thrust generated is over the first quarter of the spike. This initiated the plug (truncated spike) nozzle designs. 2D linear aerospikes with different geometries and surface roughness having a throat height of 0.25 mm were studied by Giovannini and Abhari [5]. The thrust observed was 35% lower than that obtained by ideal calculations; however, corrections in geometry could increase it by 20%. The spike design is usually based on the method of Angelino [6] or standard shapes such as linear, parabolic, etc. The various geometries used, along with their terminology, are shown in figure 1.1.

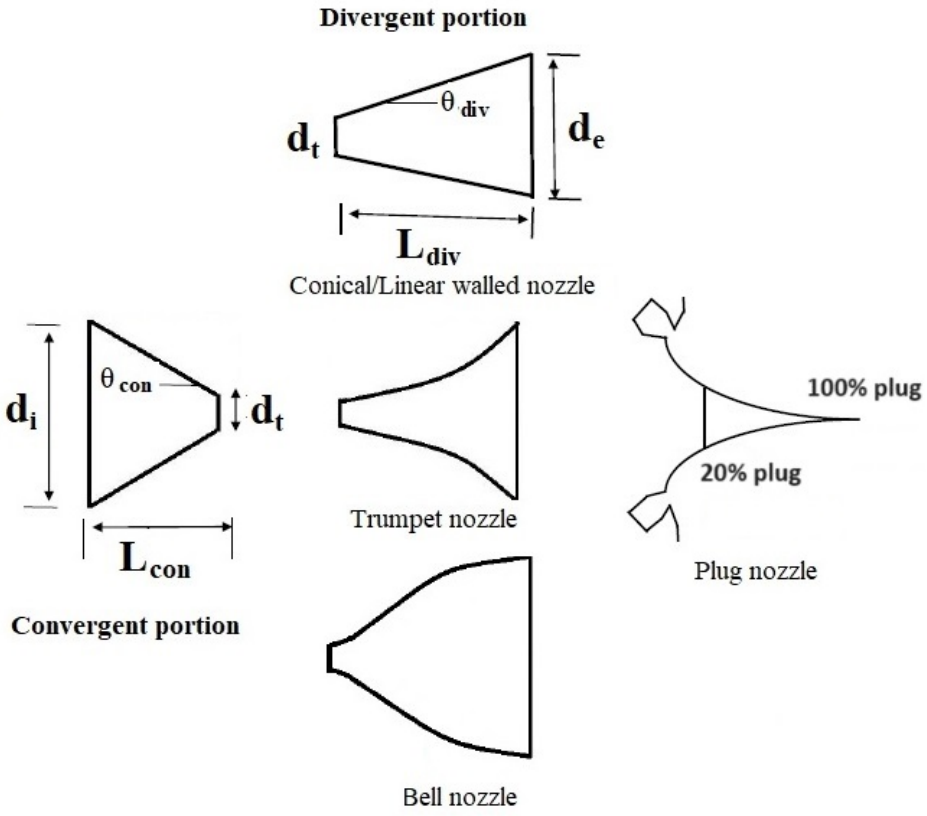

Figure 1.1: Various geometries of micronozzles[2]

1.4 Motivation

It is predicted that satellite activities in the coming decade may include mega-constellations of small satellites. The design of such a satellite system requires secondary propulsion systems having micronozzles with high specific impulse and small thrust forces [7]. Micronozzles are needed for maintaining a proper attitude and minor corrections in the trajectory of orbiting satellites and deep-space planetary probes. Another application of a supersonic micronozzle is in the aerodynamic mixture separation of isotopes/chemical species from gas mixtures [8]. Few studies have demonstrated the ability of micronozzles to separate gas mixtures when working under rarefied conditions [9]. The increased demand for Cube Satellite applications and the need for real-time fast-response sensors for monitoring pollutants and toxic releases have created interest in micronozzles operating under multi-scale

flow regimes. Although both applications require a micronozzle that operates with high efficiency, the characteristics such as size, shape, and flow pattern may vary between the two applications. A micronozzle that performs effectively for satellite propulsion may not be suitable for species separation. The current research aims to evaluate the performance of the micronozzle in both applications - satellite propulsion systems and binary mixture separation processes.

1.5 Applications of micronozzle

The demand for micro-propulsion systems has increased as a result of the rising use of cube- and nano-satellites, necessitating the improvement of micronozzle design and efficiency. The micronozzles are arranged in a cluster arrangement to achieve the desired thrust level. For such applications, uniformity in the flow structure to obtain the optimum thruster performance is the prime objective. Another application of micronozzles is species separation using an aerodynamic separation process. This technique is suggested for the immediate detection of volatile and semi-volatile pollutants and toxic releases, where rapid sensor response is essential. Few investigations have shown that micronozzles can effectively separate gas mixtures when operating in rarefied environments at supersonic speed. Other applications of micro nozzles include inkjet printing, aerosol generation, microfluidics, chemical analysis, fuel injection, semiconductor manufacturing, and mass spectrometry.

1.5.1 Satellite propulsion systems

Micro spacecraft utilization in commercial and governmental applications has been fast growing in the last decade due to its applicability for various space applications, such as education, Earth remote sensing, science, and Mars mission for relay communications and defense. It is estimated that around 1000 such satellites will be launched by the year 2022 [10]. Some of the key statistics in this regard include the launch of 84 CubeSats from ISS in 2013, 37 launches by Dnper in 2014, the launch of 101 Cubesats in a single mission involving India's PSLV in 2016, etc. The microsatellites' capabilities mainly depend on the micro- to milli-Newton range thrust-producing capacity of micro propulsion systems [11]. Propulsion systems enable the capabilities such as attitude maneuvers, including reaction wheel desaturation, attitude control, or compensation of small perturbations; ability to change the orbit, which allows station keeping or orbit transfers for formation flying or

removal of space debris. An example of a unique CubeSat application proposed recently includes the concept of reconfigurable satellite constellations for obtaining timely and targeted data for high-quality weather forecasting [12]. Micronozzle offers very fine control over the thrust requirement of microsatellites and therefore became a focus in microsatellite research. During the space operation, the flow may pass through all regimes of the continuum to free molecular flow [13]. The plume from micronozzles employed for satellite attitude control or orbit transfer maneuvers interact with the deep space environment and may cause adverse disturbances in torque, thermal loads, and contamination. Therefore micronozzle exhaust flow behavior in a vacuum space condition has been a topic of interest for space agencies.

1.5.2 Aerodynamic species separation

Real-time detection of volatile, semi-volatile pollutants, toxic releases, etc., requires a fast response of the sensors. The separation process of a binary gas mixture utilizing the supersonic outflow through a micronozzle into the vacuum is generally called aerodynamic separation. This process possesses the advantage of fast response, small size, etc., though limited by micro-fabrication and rarefaction constraints. However, the compatibility of aerodynamic mixture separation for continuous real-time applications is to be investigated further.

Various methods such as gas chromatography, sorbent beds, cryogenic accretion of materials on a surface, usage of the selectively permeable membrane, etc., have been used to increase the sensitivity of chemical sensors, but with limitations such as high response time or increased time between measurements [14]. Current requirements in medical, industrial, agricultural, transportation, safety, and environmental monitoring applications use solid-state gas sensors as the core enabling technology [15]. Solid state sensors work on the principle of the reaction of the gas species with the sensor element and the generation of an electric signal. The sensitivity, selectivity, response time, and stability of the sensor can be enhanced by increasing the concentration of the species of interest in the mixture. Another requirement of the current sensing technology is miniaturization, which enables sophisticated instruments in the field . Microdevices provide advantages such as fast response, high sensitivity, low power consumption, environmental friendliness, and affordability of mobile monitoring [16].

1.6 Thesis scope

Micronozzles come in a variety of shapes and sizes, and each application requires an optimized micro nozzle for maximum efficiency. The flow through a micronozzle is significantly influenced by its dimensions, and even small changes can result in considerable variations in flow structures. Therefore, developing an optimized nozzle design can maximize the specific efficiency or thrust per unit mass of fuel, which is crucial for the long-term operation of satellites and other space equipment. One issue with space equipment is that they may stop working when they run out of propellant, even if other components are still functional. Therefore, designing an optimized nozzle that provides maximum efficiency can help extend the lifespan of a satellite. Additionally, the exhaust gas produced by the nozzle can contaminate solar panels and other sensitive components, which can affect the overall performance of the equipment. Thus, careful consideration of the materials and design of the nozzle is essential to minimize negative impacts on the system's performance. The compatibility of aerodynamic mixture separation for continuous real-time applications is to be investigated further. Bykov and Zakharov [17] noted that the action of pressure gradients and the conversion of thermal energy into kinetic energy of the particle caused the separation, which might be more significant in a nozzle.

Therefore the current study is trying to develop the optimum size and shape of the micro nozzle for applications such as satellite propulsion and species separation. Different geometrical and flow parameters and their influence on the micronozzle performance for both applications need to be studied in detail. Studies have been conducted with different geometrical and flow parameters on a single nozzle and this study is extended to a micronozzles in the cluster arrangement for thruster application. The species separation study on the linear nozzle with various divergent shape is extended to the curved nozzle. Overall, this research can help to improve the performance of micronozzles for satellite thruster and species separation applications.

1.7 Thesis outline

The structure of the thesis is as follows.

Chapter 1 provides an overview of the study, covering aspects such as the background, distinguishing features of the micronozzle compared to traditional nozzles, and its potential

applications. Additionally, this chapter delves into the scope of the thesis and the underlying motivations driving the research.

Chapter 2 focuses on the previous studies conducted on the micronozzle experimentally and numerically. Different experimental thrust, pressure, and velocity measurement techniques, and numerical approaches like Navier Stokes, Direct Simulation Monte Carlo (DSMC), and hybrid method are described. The conclusions from the literature review and the objectives drawn for the current study are also discussed.

Chapter 3 will narrate the current experimental methodology and setup to measure the nozzle exit velocity. It also describes the numerical techniques used to study the flow structures and species separation in micronozzles like Navier Stokes with Maxwell first order slip boundary conditions, implementation of the hybrid method, and the molecular method DSMC.

The use of linear micronozzle for the thruster application is described in Chapter 4. Various geometrical effects like variation in throat height, divergent length, and divergent angle were studied along with variations in flow parameter effects like back pressure and wall temperature. The study also investigates the utilization of micronozzles arranged in a cluster, examining the effects of the varying pitch in the configuration of the nozzle array.

Chapter 5 is devoted to the study of species separation on a linear nozzle by varying throat height, divergent angle, and back pressure. The effect of carrier gas on species separation is also studied. These results are compared with bell and trumpet nozzle configurations.

The effect of curved divergent section on species separation is described in chapter 6. The study explores the variation of the divergent curve radius and the changes in wall temperatures. The back pressure effect is also studied and included in this chapter. A comparison of the effectiveness of linear and curved micronozzle designs in separating species is also described.

Chapter 7 outlines the conclusions drawn from the thesis research and describes future works.

Chapter 2

Literature Review and Objectives

This chapter reviews research on micronozzles used for satellite attitude control, deep space probes, and mixture separation. It provides a concise summary of the experimental techniques employed and advancements in numerical methods. It also examines the influence of various parameters such as size, shape, expansion ratio, surface roughness, Reynolds number, wall heat transfer, and others. The conclusion derived from the literature review is presented, followed by the objectives of the current study.

This chapter is based on

1. M.K. Sukesan, and S. R. Shine. "Micronozzle for satellite propulsion and mixture separation: a review." *Journal of Thermal Analysis and Calorimetry* (2023): 1-34, https://doi.org/10.1007/s10973-023-12227-9

2.1 Introduction

For the last two decades, research on micronozzles has primarily focused on understanding flow features and improving performance. Due to the high cost associated with comprehensive experimental studies requiring high temporal and spatial resolution, most research in this field relies on numerical simulations. The studies are categorized based on the techniques employed, including experimental and simulation methods. Since these devices operate in rarefied gas flow regimes, methods such as Boltzmann's equation via the lattice Boltzmann method, the direct simulation Monte Carlo (DSMC) method, and augmented Burnett equations are utilized to accurately predict rarefied flow characteristics. Experimental studies mainly focus on pressure and thrust measurements, as well as flow visualization

2.2 Experimental techniques

Reported experiments differ in principle, measured quantities, configurations, and cost. The small-scale nozzle experiments began with Rothe's [18] E-beam measurement of flows with a nozzle of 5 mm throat. Micronozzles required for micro propulsion applications are developed through microelectromechanical Systems (MEMS) and have lower dimensions. Most micronozzle experiments focused on thrust measurements, the most critical requirement in thruster performance characterization. Though difficult to measure, the considerable effort can be seen in the measurement of thrust, as the success rate of a mission directly depends on the thruster's performance. The optical technique is also a preferred experimental method in micronozzles as it does not perturb the flow field, leaving the parameters undergoing measurement unchanged. Due to the difficulty in fabricating supersonic micronozzles and the challenges of performing experiments, only a few reported flow, and velocity measurements. Different experimental techniques used to study flow features inside and outside the micronozzles are summarised in Fig. 2.1. It is observed that experimental data describing flow features inside micronozzles is relatively small compared to data regarding the jets outside orifices, nozzles, etc. In general, the configurations used for various studies differ significantly, and therefore difficult to draw generic conclusions. Thrust, pressure distributions, and visualization of the flow field are the primary focus of most studies and therefore are grouped here accordingly. Usually, the equipment used for experimentation includes a gas supply setup consisting of storage tanks, valves, pressure and temperature sensors, flow sensors, and a control system. The test setup is located in a vacuum chamber that is considerably larger than the micronozzle test stands to minimize the impact of the gas release on back pressure during testing. The back pressure conditions are adjusted by varying the pressure within the vacuum chamber. The thrust measuring experiments are carried out by placing the thrust test benches alongside the micronozzle test stand. The pressure measurements are done using wall pressure taps at various nozzle locations. When PSP techniques are used, micronozzles are fabricated so that the painted side might become the inner wall. The experimental setup using PSP includes an excitation light source and a charge-coupled device (CCD) camera. The flow can be visualized by exposing a fluorescing dye dissolved in the fluid to laser irradiation and using a camera to capture the resulting fluorescence signals. Many researchers use this imaging technique to emphasize the flow characteristics within and outside micronozzles.

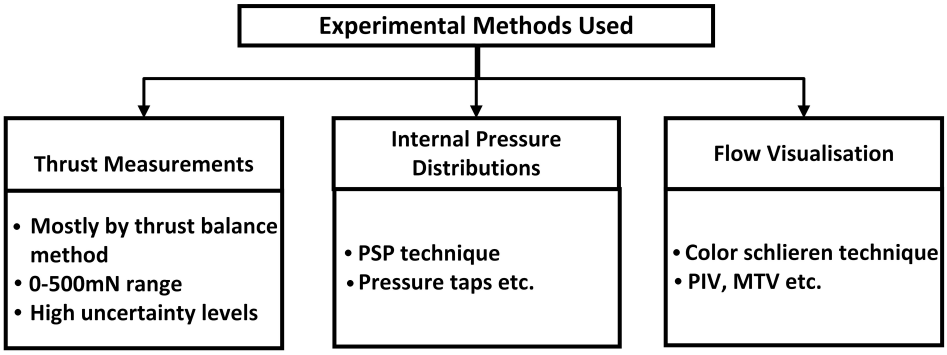

Figure 2.1: Various techniques used for micronozzle experimentation

2.2.1 Thrust measurements

One of the earlier experiments was that of Spisz et al. [19], who measured the thrust of convergent-divergent (CD) nozzles of throat area ≈ 1 mm^2 using a four-point suspension platform-type thrust stand with a differential transformer immersed in an oil bath as the sensing element. It was noted that large area ratios were not necessary for achieving the highest thrust for low Re flows. Murch et al. [20] used analytic and experimental methods to examine the thrust produced by CD nozzles at a *Re* of 600-3000. Conical nozzles of various expander angles, horn, and bell geometries were studied with an expansion ratio ranging from 1-200. The performance of conical nozzles with various divergent angles, bell, and trumpet-shaped nozzles was experimentally measured by Whalen [21]. The study could not deduce a precise prediction of the ideal nozzle as all measurements fall within experimental uncertainty. Reed [22] used an inverted and torsional pendulum thrust stand for measuring thrust produced by micronozzles of area ratio from 1 to 25. Quantitative analysis of the errors could not be established in the study. Bruccoleri et al. [23] tested ten different 2-D supersonic nozzles at *Re* ranging from 150-2000, using an updated micro newton thrust stand developed by Mirczak [24]. No significant changes in performance were observed between geometries viz: 15° cone, ideal contour, truncated lengths, etc. They noticed a substantial drop in thrust efficiency at lower *Re* due to end wall boundary layers. Williams et al. [25] measured thrust developed by a conical de Laval micronozzle using a torsional thrust balance. Nozzle efficiency was measured for Re_t in the range of 60 – 500 for 300 K nitrogen. Williams et al. [26] further developed a torsional test stand with a resolution of approximately 4.8 μm. Bao-jun et al. [27] measured the thrust of 2D Laval nozzles (9 nozzles with different structural parameters and $h_t = 100, 200, and\ 400\ \mu m$) using a torsion bar and torsion angle measurement. The optimal performance was noted

Author	Measurement technique	Range	Uncertainty levels
Spisz et al. [19]	Four-point suspension platform-type	75-500 mN	$\pm$10 %
Whalen [21]	Flexible thrust stand with mounting plate, LVDT	2.2-8.9 mN	$\pm$5 %
Reed [22]	Inverted and torsional pendulum thrust stand	Not available	Not quantified
Bruccoleri et al. [23]	Torsional balance thrust measurement with LVDT	0-100 mN	$\approx$ $\pm$30%
Williams et al. [25]	Torsional thrust balance with laser displacement sensor	0.1-10 mN	$\pm$5 %
Williams et al. [26]	Torsional thrust balance	117-1070 μN	$\pm$1.5 %
Bao-jun et al. [27]	Torsion bar with torsion angle using a photoelectric sensor	0-30 mN	Not quantified
Nishii et al. [28]	Gravity pendulum-type thrust balance with LED displacement sensor	0-10 mN	$\pm$3 %

Table 2.1: Thrust measurements

for convergent and divergent half angles at 30 and 15°, respectively. Thrust measurements of a resistojet thruster with water vapor propellant were done by Nishii et al. [28] using a gravity pendulum-type thrust balance. Displacement from the balance position was measured using a LED displacement sensor and was used to correlate the thrust force. It was found that the degree of superheating and *Re* affected the specific impulse efficiency. When $Re>100$, the mass flow rate matched the rocket equation predictions, though the viscosity effect could not be completely ruled out. Table 2.1 summarises the various studies, measurement techniques used, the range of measurements made, and the uncertainty associated with the experimental measurements. The primary sources of errors include facility vibrations, thrust stand drift, fuel, electrical connection issues, errors in the signal acquisition system, etc. As the thrust stands of most of the studies were of considerable size, Seo et al. [29] proposed the concept of a micro-load cell based on the piezoresistive sensing method. The low temperature-sensitive strain gauge was used in the measurement range of 1-7 mN within 1% uncertainty.

The review shows the requirement of highly accurate, steady-state measurement techniques in the thrust range between 100 nN and 100 mN for studying micro propulsion systems. Various thrust measurement methods adopted include target-pendulum, inverted-

pendulum, hanging-pendulum, and torsional-pendulum thrust stand. The torsional type has been preferred for steady-state measurements. Conventionally, the thrusters are placed in vacuum chambers for experimentation; therefore, the requirement of a long arm for hanging pendulum type makes it unviable. The inverted type shows greater accuracy and high sensitivity and can be a suitable choice as it has a low thrust-to-power ratio. The calibration of these devices is also essential to obtain a sufficiently good resolution. Torsional balances can also be appropriate for dealing with micro-newton and impulse measurements. Various calibration methods proposed in the literature include Jamison et al. [30] with 86 μN resolution, Gamero-Castano [31] with 0.03 μN resolution, Pancotti et al., [32] who achieved impulses from 0.01 mN to 20 mN with the linearity of 0.52%, etc. These methods require numerical simulations and evaluation of various sources of errors. Polk et al. [33] have summarised the best practices followed for the design and calibration of pendulum-type thrust stands.

2.2.2 Pressure measurements

Hao et al. [34] measured the pressure distributions adjacent to the nozzle throat and mass flow rates and studied the dependence of pressure ratio P_o/P_b and the mass flux. The application of pressure/temperature-sensitive paint (PSP/TSP) for microchannel/micronozzle measurements was initiated in late 2000. Huang et al. [35] used the pressure-sensitive paint (PSP) technique to map the pressure distribution in a De Laval micronozzle of h_t=250 μm under various operating conditions. The shock waves were detected in the PSP results for high-pressure conditions only. Nagai et al. [[36] also used the PSP surface as the inner wall of the nozzle and captured the pressure distribution inside a 2D micronozzle of h_t250 μm. An exit *M* of 4 was achieved during the experiments, and it was observed that boundary layer growth significantly affected the pressure distributions inside the nozzle. Matsuda et al. [37] applied pressure-sensitive molecular film (PSMF) to obtain pressure distribution inside micronozzles of w_t = 103 and 48 μm. The measured distributions, which showed the symmetrical nature of the nozzle center line, captured the sharp drop near the throat but had noisier data at the throat upstream region compared to the downstream region. Namura and Toriyama [38] measured pressure on the side wall of a 2D micronozzle of w_t = 100 μm using pressure taps of 5 μm diameter. The measurements were for an exit *M* of 1.37 at a plenum chamber pressure of 307 kPa. Giovannini and Abhari [5] measured total pressure downstream of the throat of a linear aerospike nozzle using a sting probe and capacitive pressure sensors. Measurements were done in two planes perpendicular to

each other. Measured values were modified using a correction procedure for accounting for errors due to non-equilibrium and rarefaction effects on the probe. Gomez and Groll [39] measured pressure difference and mass flow across a Laval nozzle of d_t =.9 mm for various gases such as xenon, argon, krypton, and neon. Timofeev and Aniskin [40] measured the supersonic core length of jets emanating from rectangular micro-nozzles (Throat dimensions: 119×135 and 927×2185 μm) using pitot tubes.

The PSP technique has been used by many in the current scenario. Still, its accuracy depends upon the binder and dye used as well as the coating procedure, amount of additives, etc. There could be limitations in the optimum pressure range based on the binder used. Anodized aluminum or trimethylsilyl-propanoic acid-based polymer PSP are recommended for low-pressure conditions [41]. Compared to the conventional PSP method, PSMF has high-pressure sensitivity and low surface roughness ($\approx$1 nm). However, the method has the disadvantages such as low luminescent intensity, low signal-to-noise ratio, etc. Matsuda et al. [37] inserted pure AA layers between PSMF and the substrate as a spacer to enhance the luminescent intensity. It was observed that this method produced high spatial resolution for micro-scale measurements having a characteristic length greater than 50 μm.

2.2.3 Optical methods

Nowadays, optical diagnostic tools developed using lasers have a major impact on experimental flow analysis. Irradiation using a laser source to a fluorescing dye dissolved in the fluid flow and the collection of fluorescence signals by a camera allows visualization of the flow. This imaging technique is used by many to highlight the flow features inside and outside the micronozzles. The studies describing the flow features inside and outside the nozzle are described below. Rothe [18] applied the electron beam technique to study conical nozzles of $d_t = 5 \; and \; 10mm$. This technique allowed photographing different regions of the flow by moving the electron beam relative to the flow field. Photographs revealed the gas density variation, which is proportional to the beam luminescence. Nozzle inner measurements were accomplished by allowing the electron beam to reach the interior through the drilled holes at the top wall of the nozzle. Rothe [18] noted the existence of an inviscid core in the flow range of $500 < Re < 1000$. For $Re \approx 100$, the exit flow was subsonic, substantiating earlier observations of an embedded supersonic bubble in the expanding flow. The experiments indicated flow separation at over-expanded conditions

but failed to notice any changes during under-expanded conditions. The coherent anti-Stokes Raman scattering technique was used by Boyd et al. [42] to measure the velocity and the translational temperature at various locations of a conical CD nozzle of r_t= 0.66 mm. Spatial concentration maps of various species in a hydrazine resistojet were obtained by this method and were useful in creating experimental data for comparison with Monte Carlo simulations. Broc et al. [43] used laser-induced fluorescence technique (LIF) to measure the temperature and density of cold NO_2 supersonic expansions through a conical CD nozzle of r_t= 2 mm. NO_2 was used as a tracer in an O_2 main flow. Experiments were performed under a wide range of under-expanded free jet flow conditions. It was noticed that statistical errors caused by the error in intensity measurements of the LIF spectrum, the thermal drift of the dye laser bandwidth and/or wavelength, condensation of NO, and finite laser beam cross-section could affect the accuracy of measurements. Choudhuri et al. [44] used Color Schlieren Defectometry to visualize flow inside micronozzles of conical (15° and 20°), bell, and trumpet-shaped diverging sections. The performance of the lower divergence angle (15°) nozzle was superior as the flow remained attached to the wall compared to other geometries. Lempert et al. [45] demonstrated the application of acetone-based Molecular Tagging Velocimetry (MTV) in the quantitative measurement of supersonic velocity jets from a nozzle of 1 mm exit diameter. It was noted that at low densities, velocity measurement accuracy was poor due to mass diffusion, and the method might not be suitable for slip and transition flows. In addition, the shorter life of Acetone laser-induced fluorescence at low pressures was also a matter of concern for the data obtained. Handa et al. [46] obtained the number density variation along a 2-D micronozzle (h_t = 286 μm) centreline using laser-induced fluorescence (LIF) for *Re* of 618-5560. The experimental results were used to validate the computational model developed using N-S equations. Nazari et al. [47] used 3D computerized tomography (CT) to obtain density distributions of micro jets emanating from CD (Laval) circular ($d_t = 922\mu m$) and square micronozzles ($w_t = 850\mu m$). Shock-cell structure, spacing, and supersonic core length of expanded, over-expanded, and under-expanded jets into the ambient were obtained. Rainbow schlieren deflectometry, along with the computed tomography, was used by Maeda et al. [48] to obtain density fields of a free jet of a square Laval micronozzle. The shock shell structure was well captured, and efficient use of schlieren CT for obtaining a density contour plot was demonstrated. Kozlov et al. [49] used a Tepler device and digital camera to obtain shadow images of jets emanating from a CD Laval nozzle ($d_t = 0.45mm$). Nozzle exit flame detachment, shock cells, and specific flow features close to the nozzle exit ("bottleneck flame region") were noticed for the hydrogen micro jet. The various flow vi-

Author	Nozzle details	Visualisation technique used
Rothe [18]	Conical, d_t =5 & 2.5 mm	Electron-beam fluorescence technique for measuring ρ and T
Boyd et al. [42]	Conical, d_t =0.66 ϵ=114	Axial velocity and translational temperature using coherent anti-Stokes Raman scattering
Broc et al. [43]	Conical, d_t =2	2D rotational temperature and density field measured by laser-induced fluorescence (LIF)
Choudhuri et al. [44]	conical, bell, and trumpet w_t =380 μm , ϵ= 25	Color Schlieren Deflectometry to visualize the flow
Lempert et al. [45]	d= 1 mm, straight nozzle	Acetone-based Molecular Tagging Velocimetry
Handa et al. [46]	h_t = 286 & 500 μm, w_t = 5000μm CD rectangular nozzle	number density distribution along the nozzle using the laser-induced fluorescence (LIF)
Maeda et al. [48]	$h_t = 1mm$ 2D Lavel nozzle	Density fields obtained by rainbow schlieren deflectometry
Kozlov et al. [49]	$d_t = 0.45mm$ CD Lavel nozzle	Shadow patterns using a Tepler device and digital camera
Nazari et al. [47]	round $d_t = 922\mu m$ and square $w_t = 850\mu m$ CD Lavel	3D computerized tomography (CT)

Table 2.2: Summary of micronozzle experiments using optical techniques

sualization experiments are summarised in Table 2.2 to get a quick overview of the various methods and configurations used.

Since visual observations will provide a more comprehensive view of the flow fields, the current trend is to use advanced techniques for flow visualization. In association with optical techniques, high-speed photography is the key technique used in recent experiments. The optical techniques have to deal with the small dimensions of the micronozzles, especially while using them for internal flow and the nozzle exit. Another issue is the in-vacuum measurement of the exhaust plume structure, where method such as Raman scattering is impossible below 200 mTorr. Schlieren imaging technique has been the

standard for visualizing density gradients; however, image noise due to random variation of brightness can significantly reduce the quality of the image and quantitative data. Recently multiple-source Schlieren system has been proposed to overcome this limitation. Nazari et al. [50] have proposed "inverse process" and "multi-path integration" techniques for image-noise reduction. Settles and Hargather [51] provide a recent review on the developments in schlieren and shadowgraph techniques. Micro particle image velocimetry (μPIV) is another technique used recently and is preferred as the micro-scale fluid mechanics avoid Brownian motion at high seeding density. The primary issue with this technique is the requirement of tiny seed particles which can follow the fluid flow without impacting and clogging the device. The seed particles should be sufficiently large to ensure practical imaging and decrease the effect of Brownian motion. Currently, a local resolution of 1 μm can be achieved, though, using small seed particles, this constraint can be decreased to a factor of 2 to 4. The camera's sensitivity/ quantum efficiency is another factor determining the image quality. Intensified charge-coupled devices (CCD) or double-shutter cameras are used to overcome this. The use of advanced flow visualization techniques such as three-dimensional (3D) particle tracking velocimetry (3D-PTV), tomographic PIV, holographic PIV (HPIV) technique, and stereo PIV (SPIV), etc., are the current trend and expected to dominate the investigation of complex flow phenomena. Stereo PIV measurements have the advantage of higher in-plane spatial resolution than 3D-PTV and tomographic PIV methods. However, PIV is usually recommended when a high feeding and particle image density are available. When the feeding density is lower, as, in micronozzles, PTV has the advantage of greater accuracy but is vulnerable to a long exposure time. With more advanced high-performance hardware, novel seeding particles, new processing, and data assimilation techniques, these methods may provide velocity, acceleration, and even pressure for every seeding particle. Therefore these methods will form state-of-the-art visualization techniques for the future.

2.3 Numerical methods

The computational analysis of micronozzles has gained popularity due to the difficulty of assessing the internal flow at the micro-scale experimentally. The limitation for experimentation is caused by factors such as the micro/nano-scales, low-pressure conditions existing in thruster exit, and the various uncertainties associated with each technique. As the nozzle exit pressure decreases, the continuum hypothesis is initially broken at the solid boundaries with discontinuity of velocity, and the temperature field appears at the solid boundary. For

space applications, the degree of rarefaction is severe; the flow may be extended to the free molecular regime. One of the convenient methods proposed in the literature to characterize the rarefied gas effect is to use the Knudson number, *Kn* =λ/L, which depends on the mean free path and a characteristic length. In micronozzles, the characteristic length can be the throat dimension. Flow regimes are based on the *Kn* with $0.001 > Kn$-continuum regime, $0.1 > Kn > 0.001$-slip regime, $10 > Kn > 0.1$-transition regime, and $Kn > 10$-free molecular flow; though these limits are not fixed, but can be considered as a reference order [52]. Thus the major challenge faced in the simulation of micronozzles is considering the wide range of *Kn* present in the flow field. Therefore various techniques have been employed to determine the flow field inside and outside the nozzle, performance, efficiency, and plume characteristics. The numerical simulations were initially carried out in the framework of Navier–Stokes equations to obtain the gas dynamic features ([53], [54], [55], [56]). These studies revealed the effect of throat dimensions on discharge coefficients, the boundary layer effects on the divergent part, and the mixing characteristics of the jet. However, when the throat dimension and flow rates are $< 1mm$ and $10m/s$, respectively *Kn* will become appreciable, and the application of N-S equations becomes questionable. Flow regimes at the nozzle throat to the nozzle exit can change from near-continuum to rarefied, and therefore both continuum and kinetic approaches have been used.

The methods based on the kinetic theory of gases are expressed using Boltzmann's equation [57]. Different equations used to simulate rarefied flows are (i) the linearized kinetic equations, [58], [59] (ii) the higher-order governing equations such as Burnett [60] and moment equations [61],[62], (iii) Boltzmann's equation via the lattice Boltzmann method ([63],[64], and (iv) molecular-based DSMC method [52], [65], [66]), etc. Fig.2.2 summarises the various approaches used in the micronozzle simulation based on the kn.

2.3.1 Simulations based on Navier-Stokes

Since methods based on kinetic theory demand substantial computational resources, N-S solvers and a velocity slip model for the wall have been suggested as an alternative approach. The wall conditions may be first order [67], second order or higher order slip-flow ([68], [69]). The concept of these methods is that for rarefied gas, the fluid velocity near the wall will differ from that of the wall. The gas velocity near the wall is described by the velocity of the wall and the gas, which is within a distance of the mean free path. At

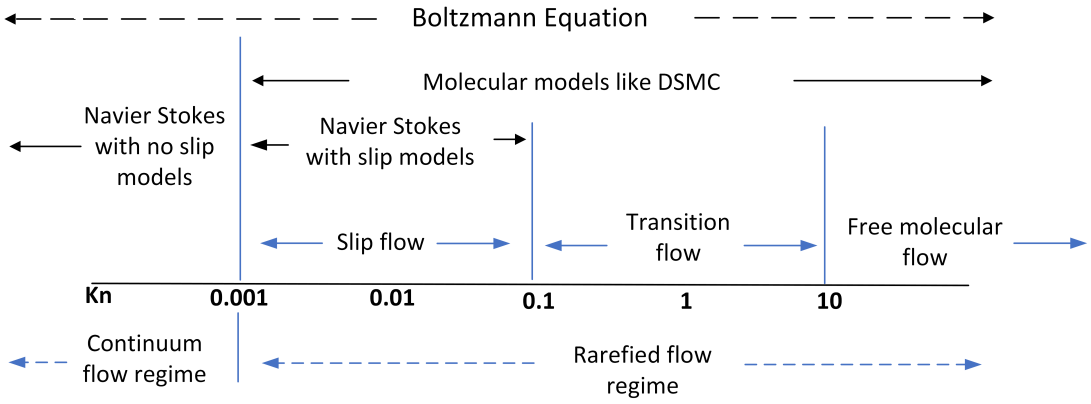

Figure 2.2: Comparison of various simulation techniques

low pressures, the mean free path is big, and the velocity jump is not negligible. When the gas is slightly rarefied, the velocity jump can be assumed to be linearly proportional to normal velocity gradients [68]. This may be highly non-linear at very low pressures, which requires higher-order slip boundary conditions. The slip conditions proposed are based on gas-solid interaction theories developed, such as Maxwell scattering theory, Langmuir adsorption theory, the Maxwell-Langmuir hybrid theory, etc. Maxwell theory considers the specular and diffuse reflection at the wall surface. [67] proposed that velocity slip is proportional to the fraction of diffusively reflecting molecules (σ) and obtained the velocity at the wall. This is formally obtained from developing Boltzmann equations into an infinite series and approximating it to first order. Langmuir theory [70]considers gas adsorption at the wall surface. Table 2.3 shows the proposed first-order slip and jump models. A study by Le et al. [71] showed that Maxwell and Langmuir models could predict slip flow regimes accurately, whereas the Langmuir slip model is valid for the transition regime.

The second order slip is applicable at lower pressures than the first order and is shown to be consistent along with N-S [68]. Second-order models [75], [68] proposed have boundary conditions supplemented by terms involving second-order velocity gradients in the normal direction, though they differ by the value of coefficients. With second-order boundary conditions, the flow is not generally governed by N-S equations, and one is expected to solve the Burnett equations [69]. However, N-S equations have been used to describe the flow as it makes the problem solvable by defining effective coefficients. Another approach suggested for transition flow regimes is the modification of N-S equations by including additional terms such as volume diffusion [76, 77] or self-mass diffusion [78].

No	Author	Theory	Model name	Proposed velocity & temperature jump conditions
1	Maxwell [67]	Maxwell	Maxwell	$u_s = C_l\lambda\frac{\partial u_x}{\partial n} + u_w$, $C_l = \alpha(\frac{2-\sigma_v}{\sigma_v})$, $T_s = \frac{2-\alpha}{\alpha}\frac{2\gamma}{(\gamma+1)P_r}\lambda\frac{\partial T}{\partial n} + T_w$
2	Bahukudumbi [72]		Max B	$C_l = 1.2977+$ $0.71851tan^{-1}(-1.17488Kn^{0.58642})$
3	Agrawal and Prabhu [73]		Max A	C_l=1.13 when $Kn \leq 0.1$ and C_l=1.7 when $0.1 \leq Kn \leq 8.3$
4	Myong et al. [70]	Langmuir	Langmuir	$u = \alpha u_w + (1-\alpha)u_g$, $T = \alpha T_w + (1-\alpha)T_g$, $\alpha = \frac{\beta p}{1+\beta p}$, $\beta = \frac{A_m\lambda}{R_u T_w}exp(\frac{D_e}{R_u T_w})$,
5	Le et al. [74]	Langmuir -Maxwell	L-M	$u_s = (\frac{1}{1-\alpha})\lambda\frac{\partial u_x}{\partial n}$, $T_0 - T_w = (\frac{1}{1-\alpha})\frac{2\gamma}{(\gamma+1)P_r}\lambda\frac{\partial T}{\partial n}$

Table 2.3: Various slip and jump models proposed

Bayt et al. [79] used first-order slip boundary conditions along with N-S equations and compared experimental mass flow rates from micro Laval nozzles of throat dimensions 20-30 μm. Deviations were around 7% for throat *Re* of 500. Moríñigo and Hermida-Quesada [80] suggested that local *Kn* could vary from nozzle throat to the lip and be based on the local Knudsen layer and local nozzle diameter. This definition would bring *Kn* within moderate ranges ($Kn \sim$ 0.3-0.4) in most of the nozzle cross-section and argued that an N-S solver along with a second-order slip model could be implemented for the numerical simulation of micro-devices. They implemented second order Knudsen layer slip model ([81]) along with N-S equations and found that the model predictions were in good agreement with DSMC solutions of Alexeenko et al. [82], [83]. The thrust and specific impulse variation were within 6% and 9%, respectively. Mass flow predictions by Hao et al. [34] from NS simulations for a 20μm throat nozzle were in good agreement with the experimental results. Nagai et al. [36] used the N-S equation along with *q-w* two-equation turbulence model ([84]) and no-slip boundary conditions to simulate flow through micro nozzles of h_t= 250 μm for chamber pressure varying from 7 kPa to 100 kPa. There was reasonable agreement between computational results and experimental data at higher chamber pressures but differed greatly at lower chamber pressure. 2D simulations could not predict the *M* distributions within the reasonable limit in all cases. Louisos and Hitt [85] pointed out that 2D simulations overpredicted efficiency and performance as they did not account for

subsonic layer growth near the side walls and corner effects. They numerically analyzed mono-propellant-based micronozzles for various depths (25-400 μm) and throat *Re* (15-800) using a continuum model with no slip and first-order slip conditions. The authors argued that there was a lack of literature data for the mono-propellant nozzles as the comparisons with DSMC/experimental data [65] were not encouraging. N-S equation along with first order Maxwell velocity slip model was used by Yan et al. [86] to study the effect of a rough surface in a micronozzle having an exit *Kn* in the range of 0.0037-0.037. Singh and Kumar [87] employed a similar computational strategy to investigate the geometrical effects, area ratio, and divergence angle.

The above studies demonstrate that slip boundary conditions can extend the N-S approach's applicability for higher *Kn*. Linear slip models seem to be a good approximation over the range of $10^{-3} < Kn < 10^{-1}$. Higher-order slip models could match up to *Kn*$\approx$1. Second-order conditions corrected with diffusive reflections at the wall and the inter-particle diffusion have been proposed recently [88] to extend the applicability of N-S for the region $Kn \geq$1.

2.3.2 DSMC Method

Direct simulation Monte Carlo (DSMC) proposed by Bird [52] describes the discrete nature of the gas through the statistical approach of the Boltzmann equation. This is described as a particle method in which uncoupling the particles and their collisions are used to model gas physics. The process reproduces the governing Boltzmann equation through Lagrangian tracking and binary collision among a group of particles that represents atoms or molecules. The method involves breaking the computational domain into grid cells and independently simulating the collisions of the particles in each cell. Generally, the cell size should be smaller than the characteristic length scales to avoid non-physical diffusion effects. The cell size required for DSMC will be comparable to the mean free path near and upstream of the nozzle throat where high-density flow exists. The time step selected should be less than the mean collision time to allow the decoupling of the collision and advection process. In addition, there is an increase in the collision frequency of particles in each time step. One of the major drawbacks cited for the DSMC method is its high computational cost due to the reasons cited above. In the very first paper of Bird [89], 500 particles were simulated for 30,000 collisions per hour. Currently, more than 10^{10} collision events per hour calculation is possible [90], and therefore DSMC is being preferred by many for the

simulation of complex flows. The various steps involved are (i) setting up initial conditions, (ii)indexing and moving the particles, (iii) allowing the collision of particles based on selected collision models, and (iv) calculating the thermodynamic properties of the cells based on particles present within the cells. Chung et al. [91] showed that results from DSMC simulations were highly influenced by the choice of collision models, gas/surface interaction model, the energy exchange model, dependence of viscosity with temperature, etc. Therefore the proper selection of these methods based on the propellant and surface materials is a very important step for deriving accurate results.

In the DSMC method, two separate stages: free molecular motion and intermolecular collision, have to be modeled in every grid cell and time step. Collision schemes proposed in literature originate from the Boltzmann equations or the Kac stochastic model. The former uses the principles from the classic kinetic theory, while the latter is derived from the Kac model using mathematical operations. Initially "Time Counter" collision scheme was proposed by Bird [92], which considered the maximum number of collisions per time step. This method requires at least 20-30 particles per cell to obtain good results. The other improved schemes proposed in the literature in this category are "Null-Collision" [93], "Ballot-Box" [94], "Modified-Nanbu" [95], "Majorant Collision Frequency" [96], "No Time Counter (NTC)"[5][52] etc. All these methods are based on the Boltzmann equation and check the number of particle pairs for a collision based on the estimate of the maximum collision frequency in cells. Actual collisions will then be determined based on an acceptance-rejection criterion. As this method is subjected to errors such as statistical noise, repeated collisions, and dependence on the number of particles per cell, Belotserkovskii and Yanitskii [97] and Yanitskiy [94] proposed schemes which considered a collision probability function. Bernoulli-Trials collision scheme (BT)[93] and a simplified variant of the Bernoulli Trials scheme(SBT) [98] were then introduced to avoid the repeated collisions. Out of these methods, the SBT scheme offers higher computational efficiency [99]. Other methods introduced are the virtual sub-cell (VSC) method by LeBeau et al. [100], and Bird [101], the transient adaptive sub-cell (TAS) scheme. VSC scheme performs $O(N^2)$ operations to find the nearest neighbor of N simulators for collision. In the TAS scheme, collision cells are subdivided into sub-cells from which collision pairs are selected. An intelligent SBT (ISBT) variant was introduced by Goshayeshi et al. [102] in which a collision scheme was provided with a semi-cognition of distance. A detailed summary of various collision models proposed for the DSMC methods was described by Roohi and Stefanov [99]. SBT and NTC schemes for the micro and nano nozzle flow were com-

pared by Saadati and Roohi [103]. Both schemes showed good agreement, though NTC required five times the number of particles per cell compared to SBT to obtain accurate values of all flow properties. Table 2.4 summarises the various collision models used and the major observations.

The intermolecular interactions are fundamental to the DSMC method, so the selection of the gas collision model is crucial to predict the phenomenon. Inelastic and elastic collision models such as variable hard sphere (VHS, Larsen–Borgnakke (LB) collision models, etc., are used. Initial DSMC simulations on micronozzle flow used collision models such as the variable hard sphere (VHS) model ([91]; [104]; [105], [65]) or variable soft sphere (VSS) model ([106]; [107]; [39]) in which only the repulsive interaction between the molecules was considered. The gas temperature in micronozzle simulations may not be very high; therefore, attractive forces between molecules may exist. A generalized soft sphere (GSS) model in which attractive forces were considered was used by Wang and Li [108] in their micronozzle simulations for moderate and low temperatures. The energy exchange between the translational and internal modes was implemented through the Borgnakke-Larsen (BL) [109] model. Chung et al. [91] also implemented the BL model along with the energy exchange probability of Boyd for the calculation of rotational energy exchange. The interaction between gas molecules and the nozzle wall is handled using the accommodation coefficient. The specular reflection at the wall corresponds to full slip condition and no accommodation, whereas diffuse reflection corresponds to no slip and complete accommodation. In general, accommodation coefficients depend on Knudsen number, gas temperature, gas-wall combination, the incident angle and velocity of gas molecules, and surface temperature. As a result, micronozzle flow may occur with an incomplete accommodation coefficient. ([110], [111], [112]). The diffuse model and the Maxwell model of reflection have been used for modeling gas-surface interactions in micronozzles. Maxwell's model does not consider accommodation in the normal direction but accounts for the tangential momentum accommodation coefficient (TMAC). Cercignani-Lampis-Lord (CLL) model considers both the normal energy accommodation coefficient (NEAC) and TMAC. Various gas-surface interaction models, including different levels of accommodation, were implemented by Boyd et al. [113]. The diffuse reflection predictions were closer to the experimental data. Specular reflection, adiabatic wall, diffuse reflection with various thermal accommodations, and a combination of all three models were implemented by Chung et al. [91]. Alexeenko et al. [106] used the Maxwell model with different TMAC values and found that specific impulse varied by 18% for TMAC change of 0 to 1 for high-temperature nozzles.

Low-temperature nozzle sensitivity was even higher for TMAC values less than 0.5. CLL molecule surface reflection model was implemented by Yang [114] for high-temperature gas flows in micronozzles. Watvisave et al. [115] varied the tangential and normal accommodation coefficient from 0.1 to 0.9 in steps of 0.2. The results showed that the exit plane *M* was more influenced by variation of TMAC compared to NEAC, whereas the wall temperature was more affected by NEAC. Considerable velocity slip was observed for both incomplete and complete accommodation. Gomez and Grroll [39] implemented the Maxwell model and the specular reflection model for flows with various gases such as xenon, argon, krypton, and neon. The Maxwell model pressure predictions were closer ($\approx 8\%$) compared to the higher deviations (varied from 23% to 41%) observed with the specular model with respect to the experimental data. The lack of momentum transport between particles and nozzle walls in the specular model created a lower pressure drop across the nozzle. Maxwell model predictions were in excellent agreement, especially at low mass flow rates.

Studies by Boyd et al. [42] have shown that the DSMC technique offers better results under rarefied conditions. However, the method is subjected to limitations owing to the simulation of the interaction of molecules. Boyd et al. [42] observed that the specific impulse predicted is within $\pm 5\%$ of the experimental data for pure hydrogen, pure nitrogen, and their mixtures. The comparisons were for a conical nozzle of r_t= 0.66 mm and gave confidence in using the DSMC method for the study of small nozzles. Alexeenkov et al. [116] used the solution of N-S equations and the DSMC method to study the flow from a micronozzle of r_t= 0.2 mm. The solution from both methods agreed well inside the nozzle region and at the core flow region of the exit jet. It is observed that at the nozzle lip, due to high flow rarefaction and rapid expansion, the continuum method failed to capture the flow features. Similar studies were conducted by Titov and Levin [117] and showed that the DSMC method was possible though computationally expensive. Shen et al. [118] observed that regulation of boundary conditions at inlet and outlet and large sample size demand limit the uses of the DSMC method in the simulation of long microchannels. DSMC with unstructured grids were used by Darbandi and Roohi [119] to simulate a wide variety of rarefaction regimes corresponding to micro (h_t=15 μm)and nano (h_t=40 nm) CD nozzles. They suggested that establishing supersonic flow in nano nozzles was impossible as *Kn* at the inlet was high. Since the viscous forces dominated, kinetic energy dissipation was high, and the flow could neither be choked at the nozzle throat nor accelerated in the divergent section.

Table 2.4: Various collision models and their outcome

Sl no	Author	Collision Model	Findings
1	Bird [92]	Time counter (TC)	Accurately predicted the results but requires at least 20-30 or more particles per cell.
2	Bird and Brady [52]	No Time Counter (NTC)	NTC scheme is an efficient method for modeling intermolecular collision if a sufficient number of particles in the cell are employed.
3	Koura [93]	Null Collision (NC)	The computation time of NC is comparable to TC and it overcomes the principle fault in TC and difficulties in collision frequency (CF) technique.
4	Nanbu [95]	Modified Nanbu Technique	The results indicate that if the number of simulated molecules is chosen properly, this technique will produce the exact solution of Boltzmann equation.
5	Ivanov [96]	Majorant Collision Frequency	Accurately predicted the results.
6	Yanitskiy [94]	Ballot-Box	The scheme cannot prevent repeated collisions within a timestep.
7	LeBeau et. al.[100]	virtual sub-cells	Virtual sub-cells appear to provide significant benefits that could be leveraged to reduce the computational burden.
8	Stefanov [98]	Simplified Bernoulli Trials (SBT)	Accurate results has been obtained with small number of particle per cell compared to NTC algorithm.
9	Saadati and Roohi [99]	SBT and NTC	Both schemes showed good agreement though NTC required five times the number of particles per cell compared to SBT to obtain accurate values of all flow properties.

10	Chung et. al. [91]	No Time Counter (NTC)	Proper choice of the simulation parameters is important for accurate result.
11	Goshayeshi et. al. [102]	Intelligent SBT on transient adaptive subcells (ISBT-TAS)	ISBT-TAS is found to be producing accurate results similar to SBT-TAS with the least possible sample size and also can reduce the mean collision separation by 25-32%.

Lijo et al. [120] used continuum and DSMC methods to compare flow through normal and micronozzles, respectively. For the normal nozzle, a scale-up version (1000 times) of the micronozzle was considered. The variable hard sphere model, Bird's no-time counter method, and the inelastic collision model of Borgnakke and Larsen were used to model the molecular collision kinetics, collision pair selection, and the energy exchange between translational and internal modes, respectively. Holman and Osborn ([121], and [122]) measured thrust developed by various micronozzle geometries in the *Re* range of 60-800 and compared the DSMC-based hypersonic aerothermodynamics particle (HAP) code [123]. The various physical models implemented in the code were the no-time-counter(NTC) scheme of Bird for collision-pair selection, the variable-hard-sphere (VHS) model, the Maxwell model for gas-surface interaction, and the harmonic oscillator model for discretized vibrational energy distributions in a vibrationally excited diatomic gas. Rotational-translational and vibrational-translational energy exchange was modeled using the Larsen-Borgnakke scheme. The NFS scheme of Ivanov and the scheme of Baganoff and McDonald [124] had also been implemented as an alternative to the NTC collision model. Overall, simulations were able to predict the thrust within the experimental uncertainty. Sabouri and Darbandi [9] studied the rarefied flow of Ar-He mixture through a CD micronozzle in the range of *Kn*=0.003-1.454 for the inlet. DSMC method was employed along with VSS molecular model and fully diffuse wall boundary condition. Reliable predictions for the mass flow rates vs pressure difference were obtained from the DSMC solver in comparison with the experimental data. VHS particle collision model, NTC collision technique, gas surfaces interaction models such as the CLL model and the Maxwell model with 600000 collision cells were used by Giovannini and Abhari [5] to simulate 2D aerospike nozzles. The parameters of the CLL model, such as accommodation coefficient α_n for the normal kinetic energy and the accommodation coefficient for the tangential momentum σ_t, were varied for comparing the computational and experimental results. The results showed that simulations with σ_t = 0.875 and α_n =1 were very close to the experimental results with the deviation in maximum horizontal velocity within 2% and thickness of kinetic boundary layer within 5%. Suggested σ_t value (0.9) was very similar to the observations by Padilla and Boyd [125]. Table 2.5 summarises the important studies on micronozzle flow with the DSMC method and their key findings.

It is now very well established that the DSMC approach is accurate enough for various micronozzle simulations. However, it suffers from the high computational cost, especially at low *M* and *Kn* number conditions. The massive computational cost is due to the stiffness of the collision operator in the near hydrodynamic regimes. As many particles have similar

Table 2.5: Various Methodologies adopted and their outcome

Sl No	Author	Collision Model	Collision Algorithm	Species	Findings
1	Boyd et.al. [113]	VHS	Not mentioned in the paper	Nitrogen	DSMC method accurately predicted the flow characteristics of low density expanding flows
2	Alexeenkov et al.[116]	VSS	Majorant frequency collision	Nitrogen	The flow was found to be weakly dependent on accommodation coefficient in the range 0.8 to 1 but changes significantly when is less than 0.5.
3	Darbandi and Roohi [119]	VHS	NTC	Nitrogen	The results from the unstructured DSMC solver indicates that it is impossible to establish supersonic flow in nano nozzles as soon as the inlet Knudsen number exceeds a high value due to strong viscous force appearance.
4	Lijo et.al.[120]	VHS	NTC	Nitrogen	At the microscale, boundary-layer separation phenomena have been found to be less pronounced and the shock detection parameter gave an indication that the DSMC shock is much thicker

5	Holman and Osborn [121]	VHS	NTC	Nitrogen	The DSMC code HAP (hypersonic aerothermodynamics particle) predicted the thrust well.
6	Sabouri and Darbandi[9]	VSS	NTC	Argon and Helium	DSMC method can be used to study the species separation in a micronozzle.
7	Giovannini and Abhari [5]	VHS	NTC	Argon	The results show that the flow can be affected by the shape of the surface, but the surface topography does not influence the growth of the kinetic boundary layer.
8	Virgile et. al. [126]	VHS	NTC	Nitrogen	The hybrid methodology shows good agreement with micro-thruster available data and its optimization allows a significant computational cost decrease.

properties, statistical accuracy can be maintained using fewer particles at a lower computational cost. The method can directly treat molecular mass, heat, and momentum transport through molecular motion and collision, avoiding explicit modeling. Therefore this is well suited for non-equilibrium problems also. With the prospect of increased HPC capabilities and quantum computing, DSMC is a feasible and reliable approach for micronozzle simulations.

2.3.3 Navier-Stokes DSMC Comparisons

In micronozzles, the nature of the flow depends on the *Kn* and is used to determine the appropriate method: statistical or continuum mechanics for simulation. Various *Kn* definitions describe the validity of the continuum model for micronozzle flow: average *Kn*, throat *Kn*, and local *Kn*, though the throat *Kn* is preferred mostly. However, it is observed that the continuum model can be applied to a wider *Kn* range when integrated quantities such as mass flow rate or thrust are the main focus of the study, rather than field properties such as velocity/*M* contours. The general understanding is (i) for *Kn* $<10^{-3}$, flow can be considered as a continuum and can be accurately modeled by N-S equations [127], and (ii) for $10^{-3}< kn <$0.1 (slip) and $0.1 < Kn < 10$ (transition), the validity of N-S equations is not guaranteed [9]. Since DSMC is valid for all *Kn* regimes [127], the comparison of results from both continuum-based N-S and DSMC simulations for micronozzle flows is available. Alexeenko et al. [82] compared micronozzle flow with throat *Kn* on 0.005 and *Re* of 200. Differences were observed at the nozzle lip, but thrust output was in good agreement. Liu et al. [128] used both the continuum method with slip boundary conditions and the DSMC method to simulate a 2D CD micronozzle of 30 μm throat width. The continuum method predicted the boundary layer inside the nozzle well, though DSMC was preferred for the nozzle exit flow near the tip region. Clear deviations between the model predictions started at a *Kn* of around 0.045. Xie [13] simulated the flow from the micronozzle of h_t= 0.2 mm using DSMC and N-S equations with slip boundary conditions. DSMC predicted well with the near-sonic flows, whereas the continuum approach failed even when *Kn* is lower than 0.01. La Torre et al. [129] compared both methods at throat *Kn* of 0.008-0.125. N-S results over-predicted the exit pressure and under-predicted the exit velocity, due to which the thrust predictions were within a 3% match. Hao et al.'s [34] slip-based N-S model predictions were compared by Lijo et al. [120] with the DSMC simulations and observed that the DSMC method produced better results. Gomez and Groll [39] compared experimental results, DSMC, and no-slip continuum-based simulations for various *Re* (8-256) and *Kn*

(0.33-0.02) for a Laval nozzle of d_t=0.9 mm. N-S results were closer to the experimental data for $Kn < 0.05$, whereas DSMC described the results more accurately in the range of $Kn > 0.1$. Rafi et al. [130] used non-linear implicit schemes based on finite volume N-S solver and DSMC with NTC collision sampling and VHS model to simulate 2D micronozzles. Good agreement between the numerical and experimental results of Boyd et al. [113] and Rothe [18] was noticed. The effect of divergence angle, nozzle wall temperature, and interaction of plumes were studied. Navier Stokes with a first-order Maxwell slip model and DSMC was employed by De Giorgi et al. [131] to study water and nitrogen flow inside planar configuration of 150 and 120 μm. Preconditioned Conjugate Gradient/Diagonal Incomplete Cholesky scheme was used for solving the governing equations. N-S was used for simulating high-pressure supersonic expansion and DSMC for low-pressure/transitional regimes. No direct comparison between the two approaches was not made. Chocking of the flow was observed due to rapid expansion near the exit. High rarefaction resulted in the loss of specific impulse of about 31.5% and 29% for water and nitrogen.

For micronozzle simulations, the high-density variations downstream of the throat will produce a rarefaction effect, mainly in the divergent portion of the nozzle. Therefore DSMC simulation is preferred in the portion of the domain where *Kn* is high. The Hybrid NS-DSMC solution technique involves identifying a coupling interface and transfer of macroscopic properties of the NS simulation to the particles of the DSMC simulation by a Dirichlet-type boundary condition. The coupling interface is based on the continuum breakdown concept. As seen from the above studies, this approach is followed by many.

2.3.4 Other kinetic approaches

Though the DSMC method produced very accurate results for highly rarefied flows [113], other methods based on kinetic approaches are also developed due to the high computational cost of the DSMC method. One of the approaches followed is to consider the deterministic solution of model kinetic equations. In this method, a relaxation-type term replaces the collision integral of the Boltzmann equation. Model kinetic equations considered are Bhatnagar–Gross–Krook (BGK) model,[132] ellipsoidal statistical BGK (ESBGK) model,[133] Shakhov model,[134] etc. Burt and Boyd [135] used the ESBGK model extending the methods described by [136]. The proposed method incorporated momentum and energy balance of monatomic and diatomic gas mixture while allowing the effects of rotational nonequilibrium. Results were compared with the experimental results of Rothe [18], and NS and DSMC simulations by Chung et al. [91]. The method produced simi-

lar results to N-S and DSMC simulations in the appropriate *Kn* ranges. It was noted that though the intermolecular collision calculations were neglected at transitional flow regimes, the ESBGK model showed good agreement with the computationally expensive DSMC method. BGK and ESBGK models were used by Kumar et al. [137] to simulate moderate and high *Re* nozzle flows. A finite volume scheme developed by Mieussens [138] was used in this study. It was observed that this method was more accurate than N-S solvers in the rarefied regime and more efficient than DSMC in the continuum regime. ESBGK model and DSMC were used by Shershnev and Kudryavtsev [139] to study the exit plume from a plane 2D micronozzle of h_t= 200μm. The kinetic equation was solved using the discrete ordinate method, the composite Simpson rule, the fifth-order WENO scheme, and the second-order Runge–Kutta TVD scheme for discretization of the space, evaluation of integrals, approximation of the convective terms, and time integration, respectively [140]. Good agreement was seen between the two approaches near the exit, though discrepancies started appearing farther downstream.

For transitional flow regimes, incorporating additional linear and non-linear stress and heat transfer terms can extend the continuum-based equations' validity range of the continuum-based equations [60]. These are known as Burnett equations and are the Chapman-Enskog expansion of the Boltzmann equations along with *Kn* [141]. Conventional Burnett equations augmented Burnett equations, and BGK-Burnett equations are the various forms available in literature [142]. San et al. [143] used an augmented Burnett equation for the numerical simulation of micro CD nozzles, and the results were compared with N-S and DSMC predictions. Third-order terms were added to the Burnett equation to obtain stable and second-order accurate solutions. The wall surface flow behavior is modeled using the first-order Maxwell-Smoluchowski slip boundary condition. Burnett and N-S solvers showed similar results in the continuum regime, and the difference between N-S and Burnett solutions increased with a reduction in throat size. Though the Burnett equation can extend the range of continuum-transition regime modeling, it suffers from major drawbacks. It exhibited numerical instabilities at high *Kn* [144] and violation of the second law of thermodynamics [145].

2.3.5 Hybrid particle approach

The combined CFD-DSMC hybrid approach may suffer from difficulties in information exchange at the interface as they are fundamentally distinct methods. Therefore, recent efforts have been made to develop particle-particle strategies. Particle-based continuum

models are suggested as an alternative method to overcome (i) the high computational cost occurring during DSMC simulations and (ii) the problems faced at the boundaries between DSMC and CFD when a coupled solver is used. Various particle-based methods such as Bhatnagar-Gross-Krook, (BGK), Fokker-Planck (FP), ellipsoidal statistical Bhatnagar-Gross-Krook (ESBGK), Fokker-Planck (ESFP) methods and the Low Diffusion (LD) method have been suggested recently as an alternative to Navier-Stokes based CFD. Pfeiffer et al. [146] used coupling of DSMC with three different particle models, such as ESBGK, ESFP, and the LD methods, to simulate the nozzle flow of throat diameter of 5 mm [18]. DSMC and the coupled ESBGK/ESFP produced good agreements near the nozzle throat and the downstream rotational temperature profiles. These schemes had a speed-up of four orders of magnitude compared to regular DSMC simulation. Fei and Jenny [147] used a second-order stochastic particle BGK (USPBGK) method along with DSMC to analyze argon gas plume flows out of a planar micronozzle of throat width of 200 μ m. Both methods use identical computational particles, and an equilibrium-breakdown criterion is used to switch between the two methods. The criterion is based on *Kn* and is easy to calculate with particle methods. The technique resulted in more accurate results in the continuum regime than the traditional BGK-DSMC hybrid method and reduced the computational cost. Pfeiffer [148] implemented a modified ESBGK model incorporating algorithms to introduce variable particle weightage at regions such as dense and low statistical samples. In this method, binary particle collisions are not calculated compared to DSMC; therefore, implementing various particle weightage in cells will not violate momentum and energy conservation. CD rectangular micronozzle having a nozzle cross-section of $10 \times 4\ \mu m$ was simulated for different pressure ratios. Comparison with DSMC simulation in the expansion region for higher densities showed that modified ESBGK has a significant advantage in terms of computational cost. The current literature on the hybrid particle approach seems promising and offers efficient simulations of multi-scale flows.

2.4 Effect of parameters

Micronozzles are characterized by lower thrust (1 μN-1 mN) and impulse, low-pressure operation, and smaller throat dimensions compared to conventional nozzles. The characteristic length being considered for this device is the throat dimension and the *Re* is defined as

$$Re = \dot{m}L/\mu A \tag{2.1}$$

Sl No.	Parameter	Effects
1	Surface roughness	Performance reduction: 1% roughness amplitude (based on) can cause a performance reduction of up to 10%. Significant increase in outlet turbulence intensity
2	*Re*	< 1000, Augmentation of wall boundary layer (BL),at 1 mN thrust level, loss is $\approx$1%; 30% outlet area covered by BL
3	Half divergence angle	Smaller area ratio and higher expansion angle preferred
4	Wall heat transfer	Reduction of the boundary layer and increased nozzle performance
5	Multi phase plume	Significant performance loss even for a small presence of droplets
6	Shape	Linear nozzle is preferred

Table 2.6: Summary of the effect of various parameters on micronozzle performance

where *L* is a characteristic length scale (e.g., the nozzle throat diameter). *Re* may be lower by many orders of magnitude ($Re \sim 10^1$-10^3) whereas surface-to-volume ratios be larger by many orders. This brings an extraordinary supersonic flow regime in the presence of strong viscous forces. This operational scenario leads to lower nozzle efficiency due to higher viscous losses in the subsonic layers near the wall. In addition, other effects, such as flow rarefaction and heat transfer, may also be present. The rarefaction effects introduce non-continuum (gas kinetic) effects. The significant viscous losses downstream of the nozzle throat and subsequent *M* decrease, temperature increase, etc., modifies the heat balance near the wall. This can create a large variation in fluid properties and *Kn* inside the nozzle both in streamwise and crosswise directions starting from the throat to the lip and outside. Rarefaction effects may be small near the throat. Still, as the gas suffers strong expansion, there can be moderate or high rarefied regimes at downstream locations based on various parameters such as surface roughness, size, expansion ratios, inlet conditions, etc. All these effects will cause significant performance degradations, which can not be predicted through traditional nozzle analysis. The major parameters identified are described below. The effects of these parameters are summarised in Table 2.6.

2.4.1 Micro-Nozzle geometry

An idealized nozzle profile provides the area required for the supersonic flow expansion and aligns the flow axially at the exit. In traditional designs, a bell-shaped contour accom-

plishes this and establishes isentropic flow conditions. The theoretical profile is obtained based on inviscid flow theory and, therefore, can't be helpful for the micronozzle flow with strong boundary layers. At the microscale, contoured nozzle fabrication is also difficult. Initial micronozzle research focused on converging-diverging nozzles (or a de Laval nozzle). This is characterized by a divergence angle θ_d for the supersonic section. Most of the studies on micronozzles are with 2D/3D conical nozzles with varying divergent sections in terms of divergence angle and length. Other shapes are aerospike designs, bell nozzles, trumpet [2], [3], and plug nozzles. Zilic et al. [4] proposed an aerospike design that could handle a wide range of ambient back pressures. A truncated spike is usually preferred in micronozzles, as most of the thrust generated is over the first quarter of the spike. This initiated the plug (truncated spike) nozzle designs. 2D linear aerospikes with different geometries and surface roughness having a throat height of 0.25 mm were studied by Giovannini and Abhari [5]. The thrust observed was 35% lower than that obtained by ideal calculations; however, corrections in geometry could increase it by 20%. The spike design is usually based on the method of Angelino [6] or standard shapes such as linear, parabolic, etc.

Choudhuri et al. [44] analyzed the performance of 2D micronozzles of 380 μm throat width and an expansion ratio of 25 having a conical, bell, and trumpet-shaped divergent sections. Conical nozzle with 15° half-divergence angle produced the highest thrust and specific impulse under various operating conditions. The study showed that the low divergence angle is preferred in micronozzles to create flow attachments toward the wall. The flow could not follow the highly divergent bell-shaped wall profile at higher chamber pressure, creating a significant drop in performance. The study also revealed the presence of asymmetric flow separation in the divergent section for all nozzles. Louisos and Hitt [149] numerically examined different bell expander configurations' thrust production and efficiency for various throat depths (25-200 μm). It was observed that the flow alignment of the bell configuration is shadowed by the increased viscous losses present. In the 3-D designs, viscous effects were more pronounced, and the subsonic layer growth around the surface was sufficiently higher. This caused severe degradation in the thrust and specific impulse efficiency.

Most of the studies related to micronozzle shapes are concentrated on micro thruster applications, and conical shapes are the preferred configuration. The priority of propulsion applications is to obtain a highly uniform flow and the highest thruster performance. Using a micronozzle for gas mixture separation demands a highly nonuniform distribution of the species in the flowing mixture.

2.4.1.1 Size, shape, and expansion ratio effects

Several studies on the effect of small changes in shape and geometrical parameres of micronozzles are available. Murch et al. [20] noted that for CD nozzles, the highest performance was for the 20° expander cone nozzles at a *Re* of 600-3000. Kim et al. [150] numerically analyzed conical nozzles of d_t =300μm having various expansion angles (0-50°) and nozzle length (600-4600 μm) to optimize the expansion angle for a given length. Simulations were done using compressible Navier-Stokes equations and Renormalization Group (RNG) k-ϵ turbulence model. An optimum half angle of around 25° and 30° was noticed for 2D axisymmetric and planar nozzles, respectively. Kim et al. [151] further investigated the effect of asymmetry on thrust by rotating the top and bottom surfaces of a 2D planar conical nozzle without changing the expansion angle. The sonic plane moved downstream without rotation but without any changes in thrust. La Torre [152] found that the performance of micronozzles with sharper throat and larger half angle was highest. He suggested that the divergent half angle for micronozzles should be higher than 15°, typically the optimized angle for large-scale nozzles. The effect of surface area to volume ratio on nozzle performance was also noticed by Rafi et al. [130]. Williams and Osborn [153] observed that micronozzles with smaller area ratios and larger half angles were more efficient. The area ratio needs to be optimally selected as it affects the isentropic expansion as well as the viscous losses. With a higher nozzle half-angle, the length of the nozzle can be reduced for a given area ratio, which reduces the boundary layer growth. Sokolov and Chernyshov [154] investigated various expander designs of CD de Laval nozzles and compared their performance. The various designs considered are conical nozzles with different expander angles and lengths, conical with cylindrical inserting, bottom with orifice, and cylindrical nozzles. The thrust produced by the conical nozzles was found to be the highest at $Re \approx 1000$. recirculation regions were developed inside cylindrical devices, which resulted in substantially lower thrust. Orifice configuration produced the lowest thrust at all flow conditions. Pearl [155] suggested that plug nozzles have reduced surface area compared to CD designs and could potentially improve performance at the microscale. Zilic et al. [4] observed substantial subsonic layers on the spike surfaces at low *Re*, which degraded the performance. Pearl [155] used shortened plugs with three different designs to examine the advantage of microscale plug designs. Numerical simulations were conducted for *Re*=80-640 using 2D N-S equations. Better performance for plug designs was noticed only during under-expanded conditions.

Ketsdever et al. [65] studied the effect of nozzle length and expansion angle. They

studied the variation of I_s as a function of axial distance from the throat and observed that shortening the nozzle resulted in higher axial velocities and a marginal increase in I_s. The half angle of the divergent section was varied from 20° to 40° for *Re*=60, and noticed that every 5° increase in angle resulted around 2% increase in I_s. Louisos and Hitt [85] varied the half angles from 15 to 45° for several nozzle depths. The expander angles showed an influence on performance only for nozzles <400 μm depth. For nozzles with depth <100 μm depth, 45 expanders exhibited the highest thrust as the increased expander angle aided in the viscus loss mitigation. Size and expansion ratio effects of micronozzles of w_t = 2 μm and 100 μm had been numerically investigated by San et al.[143]. Results obtained from N-S, DSMC, and augmented Burnett equation were compared for various expansion ratios 1.7:1, 3.4:1, and 6.8:1. The effect of different surface curvatures and surface discontinuities on the divergent section of a micronozzle of rectangular cross-section is investigated by Sebastião and Santos [156] using the DSMC method. Different shapes for the divergent section were obtained by changing the surface slope and curvature at the inflection point. Results showed that curvature of the divergent section had little effect on the aero-thermodynamic characteristics, though the discontinuities strongly affected the flow structure. However, there was no variation in specific impulse observed for all investigated cases. The changes were due to friction and heat transfer, mainly caused by the boundary layer growth and internal surface area variation associated with various curvatures [157]. Croteauv[158] studied various conical nozzle geometries for a range of half angles (θ_d=15°-60°)and area ratios (ϵ =5-100). The nozzle had a throat diameter of 1.5 mm. Half angles of 30° and an area ratio of 10 produced the highest thrust levels. Banuti et al. [159] tested a parabolic micronozzle having h_t = 90 μm using the monopropellant hydrazine. The length of the divergent section was found to be a critical design parameter, whereas the expansion ratio was irrelevant. The truncated nozzle produced higher thrust ($\approx 20\%$)) and specific impulse ($\approx 30\%$)) compared to the baseline configuration. Singh and Kumar [87] observed the boundary layer growth and decreased allowable flow area, mainly in the divergent part. The flow choking point shifted further downstream with a reduction in area ratio and a decrease in the nozzle divergence angle.

It is seen that the micronozzle performance is very sensitive to geometrical factors such as divergence angle, length, and shape. The primary issue is the build-up of the thick boundary layer, calling for an optimization involving the operating conditions, nozzle throat dimension, divergence angle, length of the divergence section, and expansion ratio.

2.4.2 Surface roughness effects

Initial studies by Ngalande et al. [66] could not observe a significant effect of wall surface effects for Re >100, though around 10% reduction in mass flow and thrust was noticed when Re <100. They used a conical De Laval nozzle of 1 mm r_t and triangular grooves of base 100 μm perpendicular to the main flow direction for creating surface roughness. Yan et al. [86] observed that the roughness of the divergent section could induce supersonic multi-waves, degrade performance, and fluctuation in flow parameters. Torre et al. [160] noted that the number and strength of these shocks depended on the amplitude and orientation of the roughness. These shocks created a reduction in overall velocity and total pressure. The larger roughness amplitudes caused stronger shocks and more significant pressure losses. A roughness amplitude of 1-2% of r_t was found to lead to a performance reduction of 18%. Cai et al. [161] attempted to relate the axial depth of cut associated with micro milling, internal surface roughness, and exit velocity of nozzles with 1 mm d_t. The velocity loss was around 5% when the critical depth of cut was 16% of d_t. Giovannini and Abhari [5] used different techniques to manufacture aerospike nozzles to obtain various surface roughness of the spike (milling with CNC machine to produce roughness average of 0.49 mum; EDM for 0.023 mum; and RP for 14.157μm). The variation in velocity was less than 2%, and kinetic boundary layer growth did not show any significant effect. Cai et al. [162] noticed that at specific ranges of surface roughness, performance variation of micronozzles is less significant compared to large-scale nozzles. For a nozzle of 1 mm throat diameter, the outlet average turbulence intensity varied from 15% to 22.7% during a relative roughness change of 0.12% to 3.84%, with a higher local variation near the wall.

It is clear that surface roughness affects the performance of the nozzles and the flow structure. However, there are heterogeneous findings on the severity of the effects. Therefore, the operating conditions of various studies are closely examined to address the conflicting results. The effect was severe while operating the micronozzle with higher pressure differences [162]. In addition, outlet velocity and thrust efficiency decreased with the reduction of nozzle size. Thus, the deterioration of performance with roughness is closely associated with the operating conditions and the decrease of the nozzle scale. The micronozzle performance is mainly affected by the flow features on the divergent section, as the viscous flow effects are more significant in this region. In addition, the rarefaction effect also plays a vital role here. Therefore in convergent-divergent micronozzles, the role of surface roughness at the divergent part is significant. In general, the height of the roughness

structure at the divergent section should be less than 1–2% of throat dimensions to minimize the effect, i.e., a 50–100 μm throat dimension corresponds to the roughness height of 0.5–1 μm.

2.4.3 Reynolds Number influence

The substantial effect of viscosity on internal flow features has been noticed previously in many studies. As the characteristic dimension decreases, *Re* is low, and a thicker boundary layer forms on the divergent section of the nozzles. Grisnik et al. [2] evaluated the performance of various micronozzles such as conical, bell, trumpet, and modified trumpet over a *Re* range of 500 to 9000. A significant decrease in specific impulse was noted at Re <1000. Similar trends were observed for the discharge coefficient with higher reduction for the bell and modified trumpet shape. Experimental studies by Bayt [163] and Choudhary et al. [44] established that for *Re*<1500, the specific impulse and nozzle efficiency decreased rapidly as *Re* decreased. Fully viscous flows were noticed around a *Re* of 1000, which resulted in a velocity decrease and augmentation of the wall boundary layer in the divergent section. Reed [22] demonstrated that nozzle dimensions and, therefore, throat *Re* directly affect thrust, impulse, and nozzle coefficient of discharge. Liu et al. [128] noticed an increase in efficiency and coefficient of discharge with the increase of *Re*. The rarefaction effects decreased with an increase in throat dimensions. Louisos and Hitt [85] studied the effect of *Re* by varying nozzle throat depth. The higher performance at high *Re* was attributed to the nozzle depth, and the relative magnitude of viscous losses scales inversely, and the relationship was linear. Torre et al. [160] noted that the performance loss due to viscous effects was high as 10% for micronozzles of 1 mN thrust level. They reported 30-50% coverage of the outlet area by the boundary layer for 1 to 0.1 mN micronozzles. Gomez and Groll [39] reported that the effect of the viscous boundary layer could be lowered by reducing the diffuser length and increasing the *Re*.

2.4.4 Thermal effects

Typically, micronozzles are fabricated into conductive substrates linked to the other parts of the spacecraft. Since firing time is less than 1 second in micro thruster applications, the substrate is approximated as a thermal source/sink of constant temperature for analysis. A lumped capacitance analysis by Kujawa et al. [164] suggested a temperature increase of 5% within the substrate. Conjugate heat transfer simulations by Alexeenko et al. [83]

showed that wall heat transfer greatly affected the flow field. Louisos investigated heat transfer effects in 2D, and 3D micronozzles and Hittc [165]. The numerical investigations indicated that heat transfer from the flow reduced the size of the boundary layer, caused the reduction of viscous effects, and increased nozzle performance. Heat loss resulted in lower wall temperature, decreased sonic velocity near the wall, and an increase in local M, which acted as the driving force in the reduction of boundary layer size. Rayleigh flow acceleration generated higher exit velocity and thrust. Williams and Osborn [153] noted that the increase in gas temperature could increase the viscosity and, therefore, the losses. However, as the flow changes from the continuum regime to the free molecular regime, an increase in temperature could result in a specific impulse increase. Williams noted this and Osborn [153] with nitrogen flow at 423 K and 523 K. Rafi et al. [130] analyzed the effect of nozzle wall temperatures and noticed variation in slip velocities and thermal boundary layer. The higher wall temperatures caused higher rarefaction and higher slip velocities. Heat flux levels were highest near the throat and decreased towards the nozzle exit. The studies above demonstrate that the micronozzle flow features and the associated performance are sensitive to the thermal conditions of the nozzle wall. The effect of electrically heated side walls on the performance of 2D micronozzles was numerically investigated by Hameed et al. [166]. Heating the side wall was effective with divergent part heating increased the thrust without significant pressure loss, while the convergent part heating resulted in decreased mass flow rate.

In summary, increased wall temperature causes an increase in slip velocity and temperature, near-wall rarefaction, and specific impulse.

2.4.5 Other effects

Greenfield et al. [167] noted that the incomplete chemical decomposition associated with micro propulsion systems could create multiphase flow conditions inside the nozzle. A nozzle flow analysis with a stream of discrete phases consisting of liquid droplets showed that the thrust reduction is significant. A drop of 19% was observed for a low volume fraction of 0.1% of submicron liquid droplets. Therefore multiphase flow might be a notable feature to be considered. This scenario is envisaged with the incomplete chemical decomposition of the monopropellant or bipropellant micro propulsion system. The gas flow may contain the dispersed phase of either solid particles or liquid droplets based on the fuel used. There is a possibility of H_2O condensation as the gas cools in the expander section. Therefore

studies on specific fuels, their combustion characteristics, and the features associated with the micro propulsion system are expected.

2.5 Major areas of application of C-D micronozzles expanding to vacuum

The two major applications of convergent-divergent micronozzles expanding to vacuum are satellite propulsion and aerodynamic gas separation. The micronozzle operates in both cases under a rarefied (slip/transitional) flow regime. The increased use of micro/nano satellites and CubeSats have propelled the first. In contrast, new applications such as portable gas sensors, μ-pre concentrators, etc., have caused renewed interest in the separation process using micronozzles. Specific work carried out in these areas is described in the following subsections.

2.5.1 Microsatellite applications

Propulsion systems enable the capabilities such as attitude maneuvers, including reaction wheel desaturation, attitude control, or compensation of small perturbations; ability to change the orbit, which allows station keeping or orbit transfers for formation flying or removal of space debris. An example of a unique CubeSat application proposed recently includes the concept of reconfigurable satellite constellations for obtaining timely and targeted data for high-quality weather forecasting [12].

The various propulsion systems proposed for micro and nanosatellite applications using nozzles are shown in Fig. 2.3. Among multiple technologies proposed, the cold gas propulsion system has the advantage of simplicity and reliability. A successful example is the European PRISMA satellite, fed by liquid butane. Butane and ammonia have been proposed in the case of liquid fuels as they reach the gaseous state on expansion. Solid propellant systems are more compact, but a low degree of flexibility and efficiency are the main drawbacks. Bipropellant hot gas thrusters are not preferred now due to the miniaturization problems of the associated subsystems. Another proposed technology is a water reservoir followed by electrolysis and combustion of resulting gases to produce thrust [168]. These systems include a converging-diverging nozzle to accelerate the exit flow and produce thrust. Micronozzle offers very fine control over the thrust requirement of microsatellites and therefore became a focus in microsatellite research. During the space

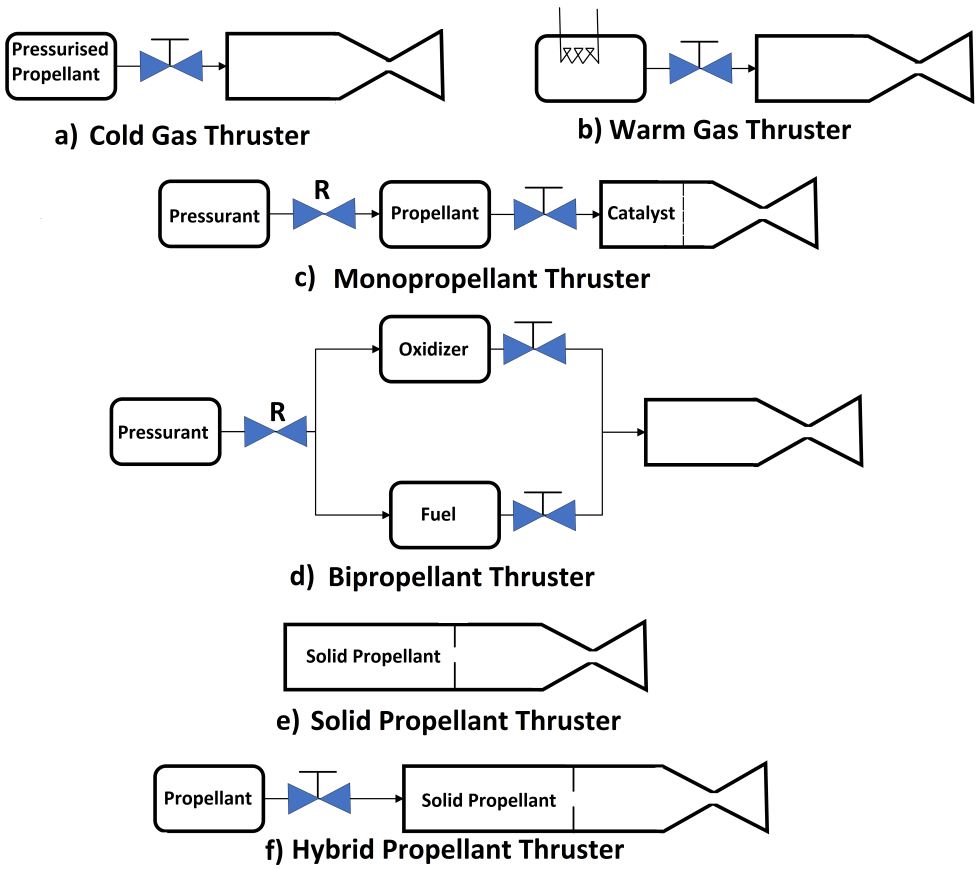

Figure 2.3: Propulsion systems proposed for micro and nanosatellites having micronozzles

operation, the flow may pass through all regimes of the continuum to free molecular flow [13]. The plume from micronozzles employed for satellite attitude control or orbit transfer maneuvers interact with the deep space environment and may cause adverse disturbances in torque, thermal loads, and contamination. Therefore micronozzle exhaust flow behavior in a vacuum space condition has been a topic of interest for space agencies. In a vacuum, the gas molecules expand freely in all directions and cause continuum, transition, and free molecular flow regimes, which led to the selection of the DSMC method as the natural choice for numerical analysis. Shershnev and Kudryavtsev [169] analyzed plumes from wedge-like micronozzles using an ellipsoidal statistical model and DSMC method. The discrepancies between the two approaches were within 2% under varying flow conditions. A typical, expected plume flow structure is shown in Fig. 2.4.

Lee et al. [170] numerically investigated a monopropellant thruster plume in a vacuum

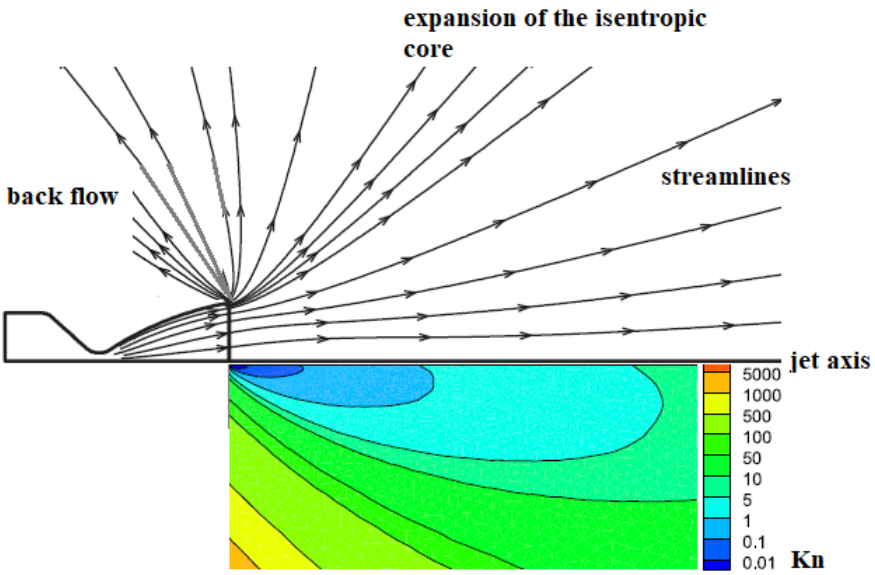

Figure 2.4: Plume flow regimes of thruster in vacuum

region using preconditioned N-S algorithm for the inside continuum region and DSMC methods for the exit regions. Velocity streamlines without backflow, an undesirable Mach disk far downstream of the nozzle exit, etc., contrary to the physics, were noted for the N-S method. This was not observed for the DSMC method, which showed turning the boundary layer at an angle greater than 90° creating a backflow region. Lee [171] studied the effect of the collision of plume particles on solar panels close to a satellite's monopropellant hydrazine thrusters. Severe plume impingement was noticed due to the panel's large surface area, resulting in a disturbance in force/torque and heat loads. Ivanov et al. [172] noted that backflow mass flow rates are less than 1% of the total mass flow rate for the micronozzles operating in a vacuum. They studied liquid fuel condensation and liquid film breakup using a hybrid N-S/DSMC approach and observed negligible droplet backflow around the nozzle lip. The low-density backflow was mainly caused by the intermolecular collisions in the plume peripheral zone. The viscosity effects dominated the rarefied regime, causing a decrease in M and an increase in temperature. Zhang et al. [173] studied the heat transfer effects of plume impingement for a 120 N thruster operating in a vacuum. It was found that the convective heat transfer is predominant within 35° cone angle and was similar to solar heat flux decrease on Earth's surface beyond a cone angle of 60°. Grabe et al. [174] discussed the difficulties of employing the DSMC method for predicting heat transfer by plume impingement. Lee [175] used the global kinetic model for simulating the combus-

tion process of a liquid propellant thruster and compared the plume behavior predicted by the chemical equilibrium reaction model. Differences were noticed in the absolute velocity, the spread of the plume, and species distributions and suggested that combustion modeling approaches could result in quite different behavior of the plume. A 10 N bipropellant thruster plume impingement on a geostationary satellite was analyzed by Chae and Baek [176] using the DSMC method. Uneven distribution of the plume gas composition was noticed due to sudden expansion in the vacuum. The most critical contaminant was H_2O, though the influence of plume impingement on sensitive surfaces was insignificant. Plume impingement of 10 N thruster and 400 N liquid apogee engines (LAE) of a geostationary orbit (GEO) satellite was compared by Lee [170] using a combined approach of computational fluid dynamics (CFD) and parallelized DSMC method. The temperature rise of the satellite platform and the solar panel adjacent to the LAE exit was noticed. The local heat flux was more than 16 W/m^2, but compared to the main plume flow, the backflow was much smaller.

Plume interaction from hydrogen/oxygen thrusters having a shrunken bell-nozzle profile was investigated by Wu et al. [177]. The separation distance was kept between 1 and 3 times the nozzle exit diameter, and the deflection angle varied from 0 to 20. Plume interaction shock, which resulted in a 3D secondary jet, was observed when the separation distance was less than two times the nozzle exit diameter. The secondary jet's compression was affected by separation distance and deflection angle. Grabe et al.[178] analyzed the interaction of plumes separated by 50 to 150 throat diameters. Interaction shocks were observed at the intersection plane, and the location of maximum mass flux along the intersection plane depended on the separation distance. An increase in backflow was predicted in highly focused plumes. Unsteady simulations of plume expansion from three thruster pulses at geostationary Earth orbit were carried out by Weaver and Boyd [179]. Time-dependent neutral plume expansions were modeled using simplifying assumptions such as free molecular flow and no charge exchange collisions. Steady-state operation of the plume was achieved 1 km downstream for a pulse of 1.4 s, whereas it was 20 km for a pulse of 9.9 s.

It is observed that numerical studies on micronozzles for satellite application are dominated by kinetic approaches, though few opted for a hybrid approach. The Hybrid NS-DSMC solution technique involves identifying a coupling interface and transfer of macroscopic properties of the NS simulation to the particles of the DSMC simulation by a

Dirichlet-type boundary condition based on local *Kn*. The primary objectives of such studies are (i) determination of the effect of backflow, (ii) fuel condensation and film breakup for the case of liquid propellant thruster, (iii) convective heat flux on side panels, and (iv) plume interaction in case of multiple thrusters. The studies show that the backflow effects, such as convective heat flux, fuel, and water contamination on side panels, may be considered in the overall mission design. A mission-specific analysis might be required as these effects mainly depend on thruster characteristics and configuration in multiple thruster schemes. Studies involving measurements from actual missions are yet to be reported.

2.5.2 Separation of gas mixtures

Aerodynamic mixture separation using expanding free jets from micronozzles was initially proposed by Reis and Fenn [180], Sherman [181] etc. Kogan [8] used a convergent-divergent nozzle with two curved walls on the divergent part to study the separation effects in a helium-argon mixture. Separation effects were increased with an increase in expansion and a decrease in settling chamber pressure. Separation micronozzle usually has curved walls resulting in curved streamlines and strong local pressure gradients. These devices were initially proposed for the separation of isotopes and later extended to applications such as chemical sensing devices [182]. It was observed that during the expansion of a binary mixture through the nozzle, a high species concentration of the heavier component is seen at the center of the jet. The enrichment is proportional to the pressure ratios across the nozzle, the gas composition, and the nozzle geometry. The concentration measured by a sampling tube increased from the nozzle exit to a maximum and then decreased to zero. Reis and Fenn [180] suggested that the detached shock wave in front of the sampling device played an important role in separation. Sabouri and Darbandi [9] used the Ar-He mixture to study micronozzles, providing a molecular mass ratio of around 10.

Kosyanchuk and Yakunchikov [183] studied the effect of geometrical features of the micronozzle, and gas selector position on the separation performance of argon–helium mixture using the event-driven molecular dynamics approach. Higher separation efficiency was found higher at higher exit velocities, curvatures, and higher speed ratios of the species. The separation was maximum at the exit with transitional and slip flow regimes. Kosyanchuk and Yakunchikov [184] observed high separation with a light carrier component and skimmer shape. The method of separation using the micronozzle may find

application in the real-time detection of toxic releases, volatile or semi-volatile pollutants, etc. The method is characterized by a fast response, small size, etc., though currently limited by fabrication and operational (exit vacuum condition) constraints. More research in this area is expected to emerge, and its implementation in sensors will be carried out soon.

2.6 Conclusions from the Literature Review

Literature review shows that micronozzles operating with vacuum exit conditions find applications in satellite propulsion systems and aerodynamic separation processes. Uniformity in the flow structure to obtain the optimum thruster performance is the prime objective of the former, while the latter demands highly non-uniform species distribution of the flowing mixture. The computational analysis of micronozzles has gained popularity due to the difficulty of experimentally assessing the internal flow at the micro-scale. The limitation for experimentation is caused by factors such as the micro/nano-scales, low-pressure conditions existing in thruster exit, and the various uncertainties associated with each technique. It is now very well established that the Direct Simulation Monte Carlo (DSMC) approach is accurate enough for various micronozzle simulations. However, it suffers high computational costs, especially at low M and Kn number conditions. The massive computational cost is due to the stiffness of the collision operator in the near hydrodynamic regimes. Previous studies demonstrated that slip boundary conditions could extend the N-S approach's applicability for higher Kn. Linear slip models seem to be a good approximation over the range of $10^{-3} < \text{Kn} < 10^{-1}$. For micronozzle simulations, the high-density variations downstream of the throat will produce a rarefaction effect, mainly in the divergent portion of the nozzle. DSMC simulation is preferred in the portion of the domain where Kn is high. Therefore hybrid methods with coupled N-S and DSMC are recommended for the simulations of micronozzles to save computational costs. Fig. 2.5 summarises the various approaches used in the micronozzle simulation.

The following inference has been made from a thorough assessment of the literature on the experimental and computational investigation of the flow characteristics of the micronozzle and its applications.

- Accurate measurement techniques are needed to study micro propulsion systems with thrusts between 100 nN and 100 mN. Torsional balances are commonly used for steady-state measurements, but the inverted type offers greater accuracy, sensitivity, and a lower thrust-to-power ratio.

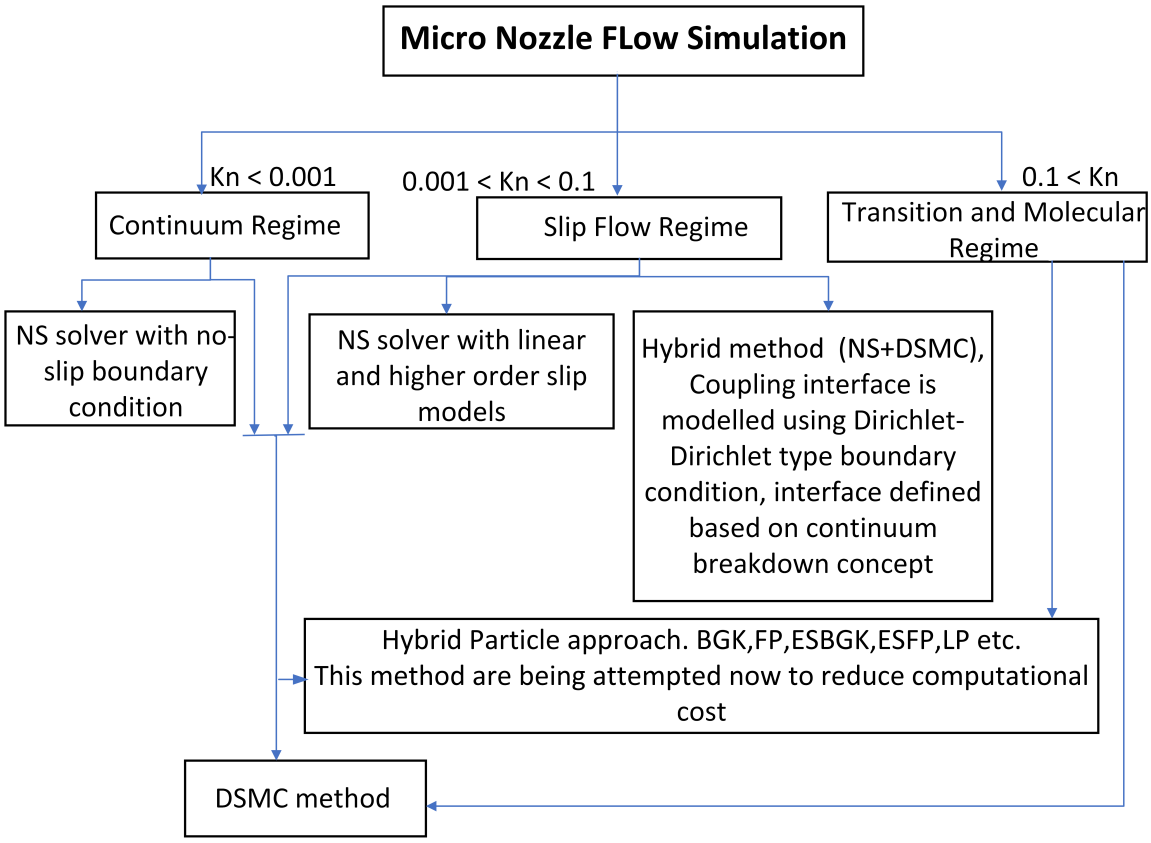

Figure 2.5: Various approaches used for micronozzle simulation

- Different pressure measurement techniques like pressure sensitive paints (PSP), Pressure sensitive molecular film, Pressure taping, sting probe and capacitive pressure sensors, and pitot tubes will provide the pressure details of the flow.
- Since visual observations will provide a more comprehensive view of the flow fields, the current trend is to use advanced techniques for flow visualization.
- The accuracy of continuum-based modelling methods is highly reduced due to the multi-scale flow and makes them of limited use, especially in the simulation of nozzles expanding to vacuum.
- For micronozzles, the simulation region includes continuum and rarefied gas regions, and therefore Navier Stokes solvers coupled with DSMC has become a straightforward approach
- The flow mainly depends on the Kn, and experiences continuum regime from the gas

chamber to nozzle throat, slip (10^{-3} < Kn < 0.1) and/or transition regimes (0.1 < Kn < 10) in the divergent part, and free molecular regime (Kn > 10) when expanding to vacuum.

- The classical method of thrust calculation of nozzle from simulation results may not be valid for micronozzles and needs to be modified to incorporate the effects of surface configuration, geometry, and Re
- It is noted that surface roughness, nozzle length, expansion ratio, and flow Re effects are highly noticeable and affect the performance of the nozzle
- Of various shapes proposed, conical being the simplest and is used in the majority of the studies.
- Micro nozzle plume interaction study at different wall temperatures is limited.
- Different types of structures like orifices, vortex tubes, and micro nozzles were used for aerodynamic species separation.
- DSMC method can be effectively used for species separation studies.
- An optimum micro nozzle design for species separation is not explored yet.

2.7 Objectives of the current work

Micronozzle has a thick boundary layer dominated flow, fundamentally different from conventional nozzles. The primary design constraint for propulsion systems is the build-up of the boundary layer, calling for a design optimization involving nozzle throat dimension, divergence angle, length of the divergence section, and expansion ratio. The current literature shows heterogeneous findings related to optimized divergence angles and the effect of back pressure. It is noted that the overall size and operating conditions prevailing influence the performance. Previous research on mixture separation using micronozzles concentrated on studying the effect of geometrical expansion ratio, wall conditions, Knudsen number, etc. The effect of divergent section contours and exit conditions on associated flow features and separation performance has yet to be studied. It is also noted that very few studies are available which discuss the separation effects of curved micronozzles operating under vacuum exit conditions.

This Ph.D. thesis analyses and explores how factors such as geometry, operating conditions, size, wall conditions, and cluster operation impact the thrust production performance of micronozzles. The study also focuses on micronozzle performance during the aerodynamic separation process. Specifically, the research will examine the effects of divergent section contours, exit conditions, and curved geometry. The research will employ computational methods such as N-S with first-order slip boundary conditions, DSMC, and a hybrid approach in a large number of micronozzle configurations operating under various exit conditions. Efforts are also made to generate experimental data that can be used for validating future computational models.

In summary, the specific objectives of the study are the following.

- Conduct a thorough literature review on micronozzles used for satellite attitude control, deep space probes, and mixture separation
- Experimental investigation of planar micronozzles
    1. Design an experiment set up to measure the plume velocity of micronozzle.
    2. Design and fabricate the converging-diverging (CD) planar micronozzle.
    3. Conduct an experiment to measure the flow velocity at the exit of the micro nozzle.
- Develop computational models for planar micronozzles using N-S with first-order slip boundary conditions, DSMC, and hybrid approach
    1. Investigate the geometrical effect on the flow behaviour by varying throat depths (2-200 μm), divergent angles (5-30°), and divergent lengths.
    2. Demonstrate the difference in flow features in the divergent section under various back pressure conditions and to address the conflicting results in the literature.
    3. Study the effect of nozzle wall heating on thrust
- Develop an empirical relation for predicting the thrust in the studied flow regime.
- Carry out the computational study on the micronozzle in the cluster arrangement
    1. Identify the geometrical effect on the plume by varying the pitch of the nozzles.
    2. Analyse the effect of nozzle wall heating.

- Develop computational models for planar and curved micronozzles with binary mixture flow using DSMC for studying separation performance

    1. Identify the geometrical effect by varying throat depths (2-8μm), divergent angles (15-45°) and divergent shapes such as linear, bell, and trumpet.
    2. Identify the effect on the species separation by varying back pressures (0-30kPa).
    3. Study the effect of a carrier gases.
    4. Identify the geometrical effect, back pressure, etc. on the species separation in a curved micronozzle by varying the radius of curvatures of the divergent section.

- Identify the predominant mechanisms of aerodynamic mixture separation.

In short, this study's main goals focus on enhancing micronozzle design used in satellite propulsion and aerodynamic separation, utilizing the insights gained from the research. The study investigates the flow characteristics of micronozzles employed in satellite propulsion under different operating conditions. The objective is to propose tools and techniques to facilitate improved micronozzle designs. The study aims to assess the feasibility and suitability of micronozzles for continuous real-time applications, particularly in aerodynamic mixture separation. The overarching objective is to contribute to developing compact and responsive sensors capable of real-time detection, thereby advancing micronozzle technology.

Chapter 3

Experimental Approach & Computational Methodology

This chapter discusses the methodology used for conducting numerical and experimental studies. The interferometric Rayleigh scattering technique is employed to collect data on the jet exit velocity, which is then used to validate the numerical simulations. The numerical methods covered in this chapter include the implementation of the Navier-Stokes equations, applying slip wall boundary conditions, utilizing the particle-based DSMC approach, and describing a hybrid approach that combines NS with DSMC. The chapter concludes by explaining the validation process of the numerical methods using experimental results and the investigation of grid and time independence.

3.1 Introduction

Experimental and numerical studies have been conducted on various micronozzle geometries during this work. Continuum flow, rarefied flow, or a mixture of both can be observed within the micronozzle during the operation, depending upon the flow parameters. The Navier-Stokes method will provide accurate results with less computational effort in a continuum flow regime, but this accuracy will decrease as the flow becomes rarefied. DSMC will give accurate results in a rarefied flow regime but at the added expense of high computational cost.

3.1.1 Basic assumptions of micronozzle flow

The basic assumptions used for the current study of micronozzle flow are as follows:

1. Gas Mixture (Experiment): The experiment assumes that acetone particles are homogeneously mixed with air, forming the working gas mixture. This assumption simplifies the analysis by considering a well-mixed propellant.

2. Adiabatic Wall: The wall of the micronozzle is considered to be adiabatic, which is justifiable due to the relatively short operation of the micronozzle, which is less than 1 millisecond [Louisos, & Hitt (200)].

3. Constant Inlet Conditions: The propellant is supplied from a large reservoir, ensuring that the inlet pressure and temperature remain constant throughout the simulation. This assumption simplifies the simulation and maintains steady boundary conditions.

4. Ideal Gas: The propellant gas is assumed to behave as an ideal gas.

5. Constant Flow Rate: The gas flow is assumed to be constant, which means that the mass flow rate remains unchanged over time.

6. Compressible Flow: The assumption that the gas is flowing at a very high velocity indicates that the gas behavior is compressible. This is a crucial assumption for analyzing supersonic flows, where changes in density and pressure are significant.

7. Species Separation: For species separation studies, the inlet gas is considered to be a homogeneous mixture. This simplifies the initial conditions for studying the separation of different components in the gas mixture.

These assumptions help simplify the modeling of the micronozzle flow, making it more manageable for analysis while still capturing the essential characteristics of the flow behavior. However, it's important to acknowledge that these are simplifications, and real-world conditions may deviate from these assumptions to some extent. The methodology used for the experimental and numerical analyses is discussed in detail below.

3.2 Experimental study

The experiment is conducted using the interferometric Rayleigh scattering technique. It is an optical technique used to measure flow velocity. The details of the experimental setup are depicted in Fig.3.1. The setup consists of a laser, focusing lenses, cameras, a scattering plate, a micronozzle, a seeder, etc. A biconvex lens with a 250 mm focal length is used to focus the output laser beam onto the area being probed. The source is a continuous-wave

diode pumped solid state laser with a wavelength of 532 nm and 220 mW output power. Light's polarisation affects how well Rayleigh scattering occurs. A half-wave plate is thus placed in front of the focusing lens and utilized to maximize the laser beam's polarisation for the best scattering results. A 100 mm focal length lens is used to capture the light scattered from the intended area and collimate it. This light is then focused on a sheet using a cylindrical plano-convex lens. At the focal point of the focused light sheet, a virtually imaged phased array (VIPA) is mounted on a multi-axis translation stage and a three-axis tilt stage. The VIPA has a free spectral range of 0.5 $cm^{\breve{}1}$ and a 500 – 600 nm transmission wavelength range. To provide the most effective transmission, the angle of incidence on the VIPA entry is adjusted using the tilt and translation stages. After the VIPA, the transmitted signal is focussed to a CCD camera using a spherical lens with a 1 m focal length. The laser beam is focused on the flow at a distance from the nozzle exit. The scattered beam will pass through the lenses and produce fringes corresponding to the velocity of the plume. The velocity of the plume ejected from the nozzle exit is calculated by measuring the Doppler shift in the scattered signal.

A micronozzle having a 500μm throat height with a depth of 1mm is fabricated on a brass plate by using an EDM technique. The dimensions and photographs of the micronozzle are shown in Fig. 3.2. After setting up the nozzle, laser, focusing lenses, scattering plate, and cameras, the initial reading is taken. Then the compressed air at a pressure of 3.5 bar is allowed to pass through a seeder that contains acetone particles. The acetone-seeded air flow is established in the micronozzle and the reflected laser due to the micronozzle flow is captured by using a primary camera, 'camera-1'.In the meantime, the secondary camera, 'camera-2' will measure the wavelength of the laser to avoid any unnecessary error caused by the shift in the laser wavelength. The shift in the spatial location of the fringes can be calculated by comparing the current position of the fringes with the initial readings and this shifting will correspond to the measured velocity of the plume. The velocity of the expanded gas can be calculated from the following equation 3.1 [185]

$$\Delta V_D = \frac{(\vec{k_s} - \vec{k_l}).\vec{u}}{2\pi} \tag{3.1}$$

Where ΔV_D is the Doppler shift, $\vec{K_s}$ and $\vec{K_l}$ are the wave vector of the scattered signal and incident light respectively. $\vec{u}$ represents the flow velocity vector. The experiment is repeated by varying the distance between the nozzle exit and the laser (2.5mm-4.5mm) in such a way that the velocity of the gas at different plume locations can be measured. Fig.

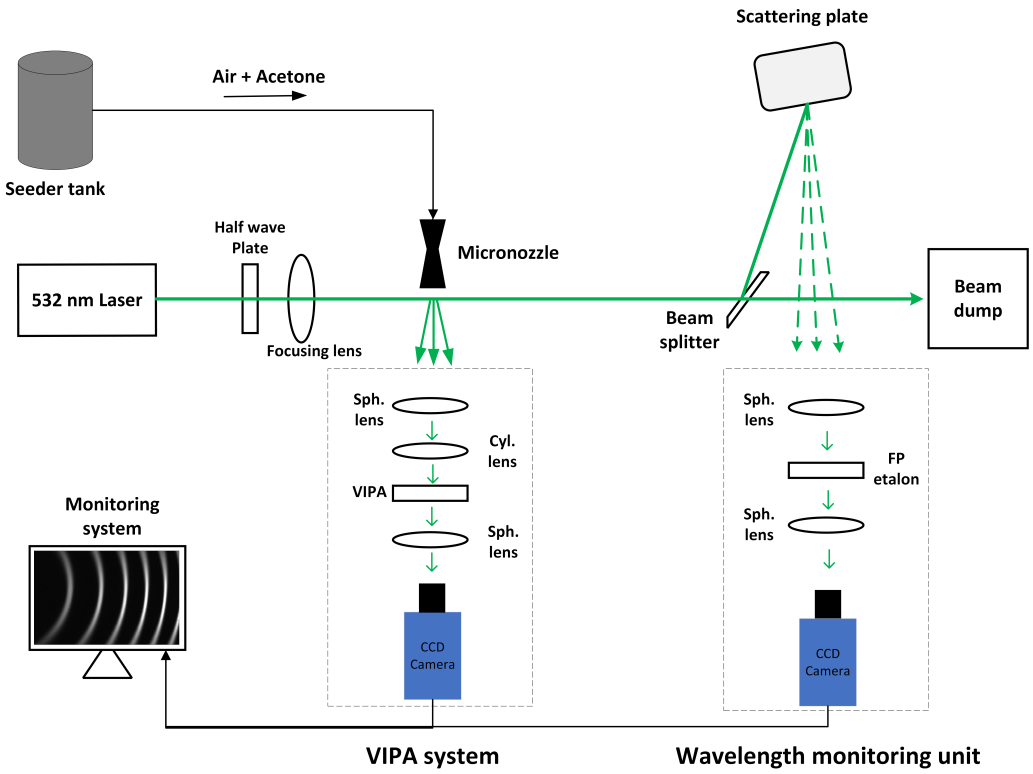

Figure 3.1: Experimental set up [1]

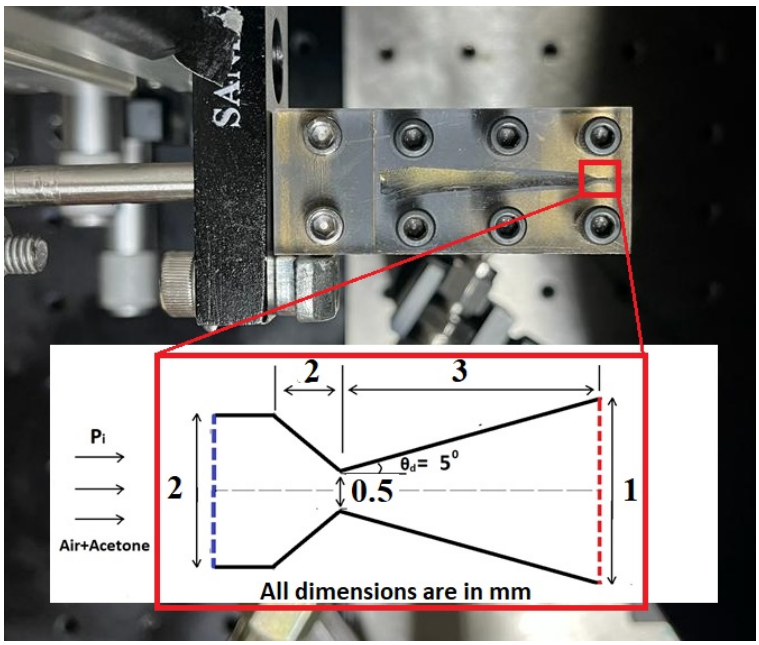

Figure 3.2: Schematic diagram and photograph of the fabricated nozzle

3.3 shows the images and connections of the experimental equipment.

3.2.1 Uncertainty calculation

Experimental uncertainty is calculated by comparing 50 images taken under the same experimental conditions. An inlet pressure of 4.5 bar is maintained, and 50 images are captured at three different locations (2.5 mm, 3.5 mm, and 4.5 mm downstream of the nozzle exit) using the same equipment, such as laser, mirror, camera, etc. These images are then compared with the reference image, and the flow velocities are calculated. The standard deviation of the average velocity is determined, providing the experimental uncertainty of 4.5% for a peak velocity range of 380-440 m/s. Figure 3.4 illustrates the procedure used to determine the uncertainty in the current experimental study

3.3 Computational Methods

Many researchers have undertaken the computational analysis of micronozzles as the experimental access of internal flow at the micro-scale is extremely difficult. The methods based on the kinetic theory of gases are expressed using Boltzmann's equation. Different equations used to simulate rarefied flows are (i) the linearized kinetic equations, (ii) the higher-order governing equations such as Burnett and moment equations (iii) Boltzmann's equation via the lattice Boltzmann method, and (iv) molecular-based direct simulation Monte Carlo (DSMC) method, etc. So in the current study, along with the N-S method and DSMC method, a hybrid approach is also used to reduce the computational cost in locations where the full DSMC study is not required. In cluster arrangement of micronozzle and species separation studies, a full DSMC study is conducted.

3.3.1 Computational resource

All N-S simulations and small DSMC simulations are conducted on an Intel i7@3.20GHz x 12-core workstation with 64GB RAM. For high-computational demanding DSMC simulations, a Virgo cluster consisting of 18 nodes, with each node equipped with 28 cores and 128GB RAM, is employed. The Virgo cluster enables the active tracking of more than 3 crore particles and facilitates efficient computation.

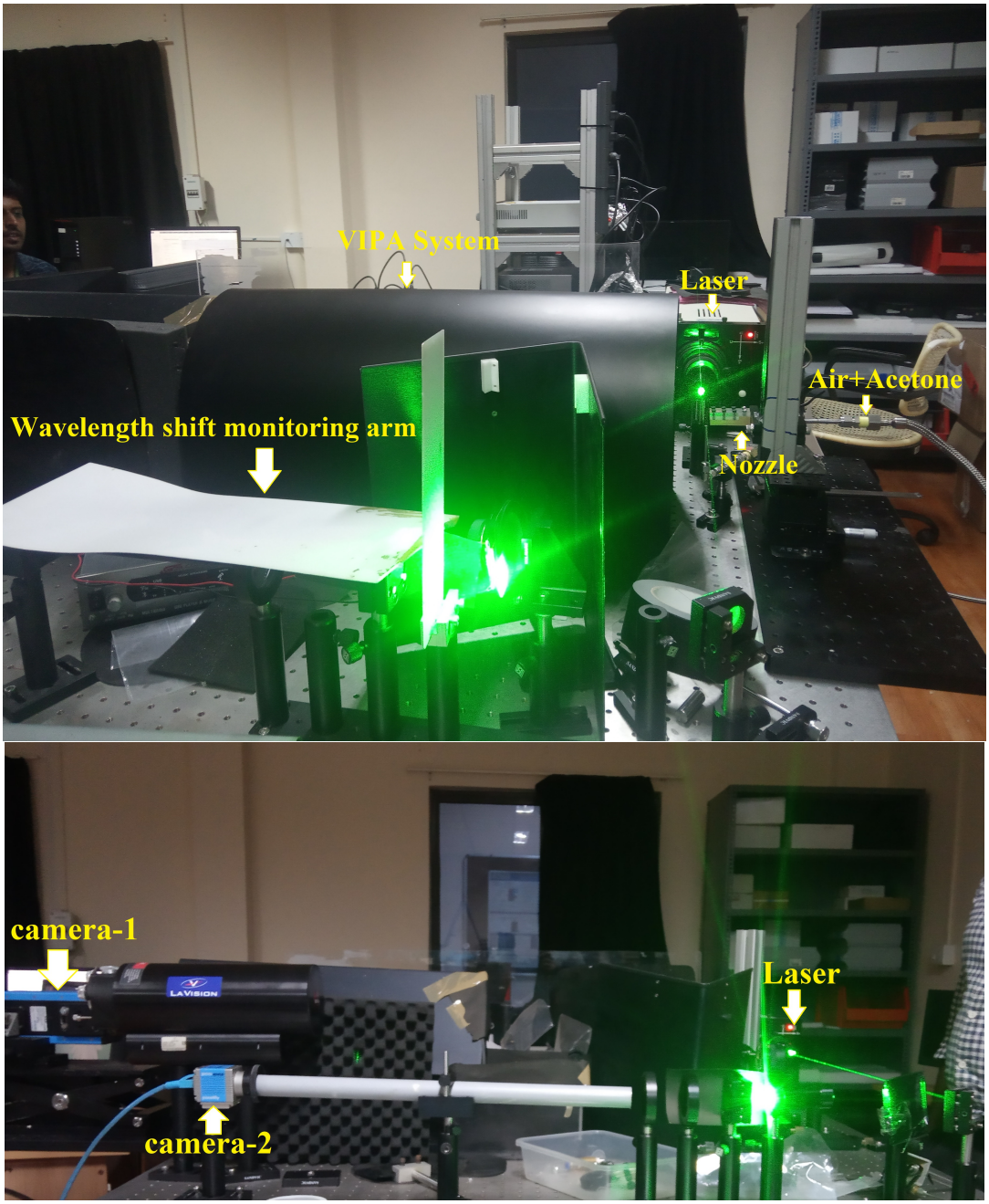

Figure 3.3: Photographs of the experimental setup

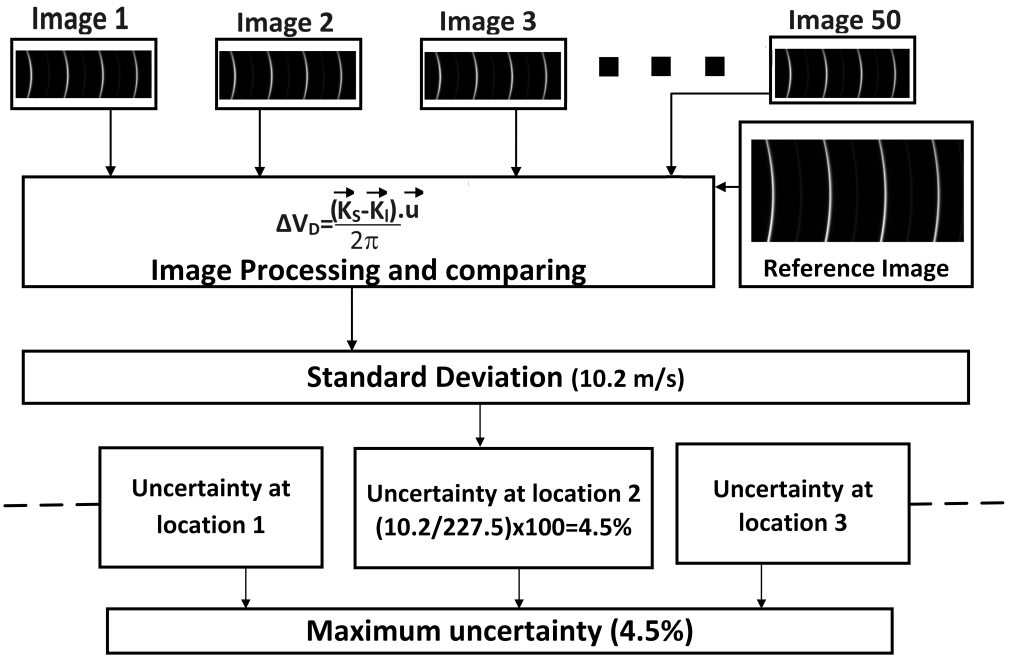

Figure 3.4: Uncertainty calculation procedure

3.3.2 Continuum method (Navier-Stokes)

The gas flow through the micronozzles in the continuum regime is modeled using the N–S equations. The continuity, momentum, and energy Equations used are presented as follows: Continuity equation

$$\frac{\partial \rho}{\partial t} + \nabla . \rho \vec{V} = 0 \tag{3.2}$$

Momentum equation (N–S equation)

$$\frac{\partial (\rho \vec{V})}{\partial t} + \nabla . (\rho \vec{V} \vec{V}) = -\nabla P + \nabla . \vec{\vec{\tau}} \tag{3.3}$$

Energy equation

$$\frac{\partial (\rho E)}{\partial t} + \nabla . (\rho \vec{V} (\rho E + P)) = \nabla . [K_c \nabla T + \vec{\vec{\tau}} . \vec{V}] \tag{3.4}$$

where

$$E = H + \frac{\vec{V}^2}{2} - \frac{P}{\rho} \tag{3.5}$$

$$\vec{\vec{\tau}} = \mu[(\nabla\vec{V} + \nabla\vec{V}^T) - \frac{2}{3}\nabla.\vec{V}I] \tag{3.6}$$

The gas flow in micronozzles in the continuum regime is modeled using the N-S equations. The system of equations is closed using the ideal gas law equation of state, $p = \rho RT$. The rarefaction effect is quantified by the Knudson number, $Kn = \lambda/L_c$. The numerical solution for the flow field is obtained by means of the Finite Volume Method. The basic algorithm used is based on the central difference scheme developed by Kurganov and Tadmor [186]. All the grids are created using blockMesh utility of OpenFoam. The Gauss Linear scheme is used for divergence, the gradient, and the Laplacian operators. Time derivatives are computed with the first order, bounded, and implicit Euler scheme. The Total Variation Diminishing (TVD) Van Leer limiter is used as the interpolation scheme. The convergence criteria for the simulation is taken as 1x10^{-6}. The specific heat capacity and viscosity are computed based on the model suggested by Ehlers et al.[187] and Sutherland law [188] respectively. All simulations are carried out using density-based, segregated, compressible flow solver rhoCentralFoam (rCF).

3.3.2.1 Navier Stokes boundary conditions

Pressure boundary conditions are employed at the domain's inlet and outlet. The nozzle walls are designated as adiabatic, and Maxwell's first-order slip boundary conditions are implemented on the walls for rarefied flow. The finite velocity-slip condition is implemented using Maxwell first order slip model and is given by

$$\vec{u_g} - \vec{u_w} = \frac{2 - \sigma_u}{\sigma_u} Kn (\frac{\partial \vec{u}}{\partial \vec{n}})_w \tag{3.7}$$

The temperature jump condition is given by

$$T_g - T_w = \frac{2 - \sigma_T}{\sigma_T} \frac{2\gamma}{\gamma + 1} \frac{Kn}{Pr} (\frac{\partial T}{\partial \vec{n}})_w \tag{3.8}$$

The values for accommodation coefficient σ_u and σ_T are taken as 1 to invoke perfect diffuse reflection with complete thermal accommodation. To account for symmetry, only half of the domain is simulated, and symmetry boundary conditions are enforced along the nozzle's centerline, as illustrated in Figure 4.1.

3.3.3 DSMC method

Direct simulation Monte Carlo (DSMC) is a particle method that uses uncoupling the particles and their collisions to model the physics of gas through the statistical approach of the Boltzmann equation. The Boltzmann equation for a simple dilute gas is

$$\frac{\partial(nf)}{\partial t} + \vec{c}.\frac{\partial(nf)}{\partial \vec{r}} + \vec{F}.\frac{\partial(nf)}{\partial \vec{c}} = \int_{-\infty}^{-\infty}\int_{0}^{4\pi} n^2[f^* f_1^* - f f_1]c_r \sigma d\Omega d\vec{c}_1 \tag{3.9}$$

where $d\Omega$ is the infinitesimal velocity space solid angle, and $d\vec{c}_1$ is the infinitesimal velocity of field molecules. f and f_1 are the velocity distribution function at c and c_1, with the superscript * denotes post-collision properties. The computational domain is subdivided into grid cells and collisions of the particle in each cell are independently simulated. The method involves the simulation of molecular motion and wall collisions deterministically and the intermolecular interactions stochastically for the case of dilute gas flows. A single particle that represents a large number of molecules moves in space freely depending upon its velocity and time step, and interacts with boundaries and other particles. A typical DSMC simulation cell has a dimension of λ/3, and each cell contains a minimum of 20 particles. The particles in the cell are allowed to interact with each other. The time step size has been selected smaller than the mean collision time of the molecules. If the time step is larger than the mean collision time, the molecule will move far without participating in the collision, leading to nonphysical results. The time step has been selected as

$$\Delta t = \frac{\lambda \xi}{c} \tag{3.10}$$

where ξ, is the fraction used to limit the time step. The explicit time-stepping scheme is used to move particles in time and space. The position of the particles is updated using a particle tracking algorithm[189]. For the wall boundaries, action will be applied based on the nature of the wall such as specular or diffuse. The gas wall interaction has been modeled as a diffusive wall where the reflected particles follow an equilibrium Maxwell distribution. Bird's no-time-counter (NTC) scheme [190] which selects pairs from a cell at a given time step is considered the collision algorithm. The number of pair selected from the given time step by the NTC algorithm is

$$\frac{1}{(2V_c)} F_N N(N-1)(\sigma_T C_r)_{max} \Delta t \tag{3.11}$$

F_N is the specific number of real molecules, N is the number of DSMC particles in the

cell at the instant and C_r and σ_T are magnitudes of the relative velocity of two molecules and the molecular collision cross-sectional area, respectively. V_C is the cell volume,Δt is the time step size, and $(\sigma_T C_r)_{max}$, is the maximum value of the product of collision cross-section and relative speed of possible particle pair in the cell. The collision is accepted if

$$\frac{(\sigma_T C_r)_{ij}}{(\sigma_T C_r)_{max}} > R_f \tag{3.12}$$

Where R_f is a random number uniformly chosen in [1,0], and $(\sigma_T C_r)_{ij}$ is the product for collision pair ij. After the collision, the velocities of the molecules will reset. The post-collision velocity of molecules i and j become

$$C_i^* = C_m^* + (\frac{m_j}{m_i + m_j})C_r^* \tag{3.13}$$

$$C_j{}^* = C_m{}^* - (\frac{m_i}{m_i + m_j})C_r^* \tag{3.14}$$

Where superscript denotes post-collision properties, C_m is the center mass velocity, and C_r is the relative velocity

$$C_r = |C_i - C_j| = |C_i{}^* - C_j{}^*| = C_r{}^* \tag{3.15}$$

The binary collision model has been selected as a Variable Hard Sphere (VHS) model with a reference temperature of 300 K for the thrust calculation studies. The variable soft sphere (VSS) model is used to predict the transport properties for the species separation study. The deflection angle in the VSS model is given by

$$\chi = 2cos^{-1}(b/d)^{1/\alpha} \tag{3.16}$$

where b is the impact parameter and d is the diameter of the molecule. The value of α generally lies between 1 and 2. The deflection angle of the VHS model is obtained by putting α =1 in the above equation. The mean free path of the gas molecules is calculated from

$$\lambda = \frac{k_B T}{\sqrt{2}\pi\xi_h^2 p} \tag{3.17}$$

where ξ_h is the hard sphere molecular diameter of the species. The model by Larsen and Borgnakke [191] is used to model the energy redistribution subsequent to an inelastic collision. The tangent velocity components are assumed as those at the adjacent cell. The open-source DSMC solver 'dsmcFoam+'[192] which is developed within the OpenFOAM

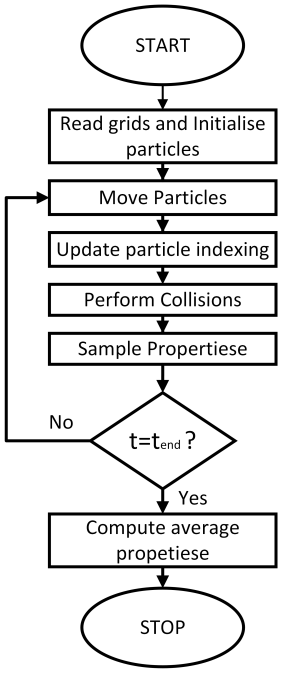

Figure 3.5: DSMC flow chart

software framework has been used for the current simulation. The molecular properties of different species used for the current DSMC simulations are shown in appendix A.The fig.3.5 depicts the flowchart of a normal DSMC procedure.

3.3.3.1 DSMC boundary conditions

The gas wall interaction has been modeled as a diffusive wall where the reflected particles follow an equilibrium Maxwell distribution in DSMC simulation. The pressure boundary conditions are applied at the inlet and exit of the domain. The particle flux at the inlet and outlet boundaries is given by

$$F = \frac{n}{(2\sqrt{\pi}\beta)}[\exp(-s^2\cos^2(\theta)) + \sqrt{\pi}\cos(\theta)(1 + erf(\cos(\theta)))] \tag{3.18}$$

where n is the particle number density and θ is the angle between the normal vector to the boundary and velocity vector. β can be estimated from the equation $\beta = 1/C_{mp} = 1/\sqrt{2RT}$, where C_{mp} is the most probable molecular speed. S can be calculated from the boundary mean velocity u by $S = u\beta$. The mean velocity at the boundary can be calculated

from the proposed method of Wang and Li [193]

$$u_{in,j} = u_j + \frac{(P_{in} - P_j)}{(\rho_j a_j)} \tag{3.19}$$

The subscript j denotes the quantity in the j^{th} cell.

$$n_{in,j} = \frac{P_{in,j}}{(K_B T_{in,j})} \tag{3.20}$$

And at the exit boundary, density, and velocity can be calculated as

$$\rho_{e,j} = \rho_j + \frac{(P_{e,j} - P_j)}{({a_j}^2)} \tag{3.21}$$

$$u_{e,j} = u_j + \frac{(P_{e,j} - P_j)}{(\rho_j a_j)} \tag{3.22}$$

The temperature is calculated using the ideal gas equation at the outlet element j.

$$T_{e,j} = \frac{P_{e,j}}{(\rho_j R)} \tag{3.23}$$

Again, for the sake of reducing computational cost, only half of the domain is simulated us-

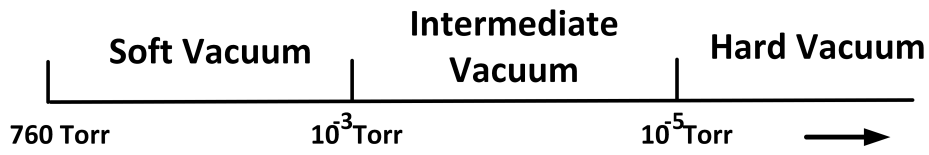

Figure 3.6: Classification of vacuum based on pressure

ing symmetry plane boundary conditions. The specific definition of the hard vacuum used in the current study is outlined in fig.3.6. To simulate the hard vacuum in the DSMC investigations, a DSMC deletion boundary was implemented along with the pressure boundary condition at the outlet of the simulation domain. Due to the usage of a hard vacuum boundary at the exit, particles exiting through this boundary were promptly removed. Also, the particles were not permitted to re-enter the simulation through the exit domain.

3.3.4 Hybrid approach

Previous studies, as referenced in [129] and [130], have demonstrated the effectiveness of the hybrid approach in reducing computational efforts while maintaining a high level of accuracy in predicting results for micronozzle flows.For hybrid micronozzle simulations, the high-density variations downstream of the throat will produce a rarefaction effect mainly in the divergent portion of the nozzle. Therefore DSMC simulation is only required in the portion of the domain where the Knudsen number is high. The hybrid NS-DSMC solution technique involves identifying a coupling interface and transfer of macroscopic properties of the NS simulation to the particles of the DSMC simulation by a Dirichlet-type boundary condition. The coupling interface is based on the continuum breakdown concept which is based on the Gradient Length Local Knudsen number (KnGLL) [130] given by

$$Br = max(kn_{GLL-\rho}, kn_{GLL-T}, kn_{GLL-|u|}) = 0.02 \tag{3.24}$$

The velocity, number density, and temperature have been used to insert particles into the DSMC domain based on Maxwellian distribution.The fig.3.7outlines the standard steps followed on a hybrid DSMC technique.

3.4 Grid, time step and no. of particle independence study for DSMC

The following criteria are used to perform a grid independence analysis for the DSMC solver. The DSMC requirements include (i) cell size smaller than the local mean free path, (ii) time step smaller than the local mean collision time (t), and (iii) sufficient molecules per cell to avoid statistical fluctuations in the sampling process.

3.4.1 Grid independence study

The simulations are done with various cell sizes such as λ, λ/3, and λ/6. Fig. 3.8 depicts the variation of normalized SF_6 concentration along line 2 inside the nozzle for the binary mixture simulations.Fig. 3.8 contains graphs depicting different numbers of particles in various grids. It serves as a combined graph for sections 3.4.1 and 3.4.2. Within these graphs, three lines illustrate the changes in SF_6 local/SF_6 bottom for various cell sizes. Additionally, another set of three lines represents the deviation in the results for different numbers of particles within the simulation and one line is common for both sections. It

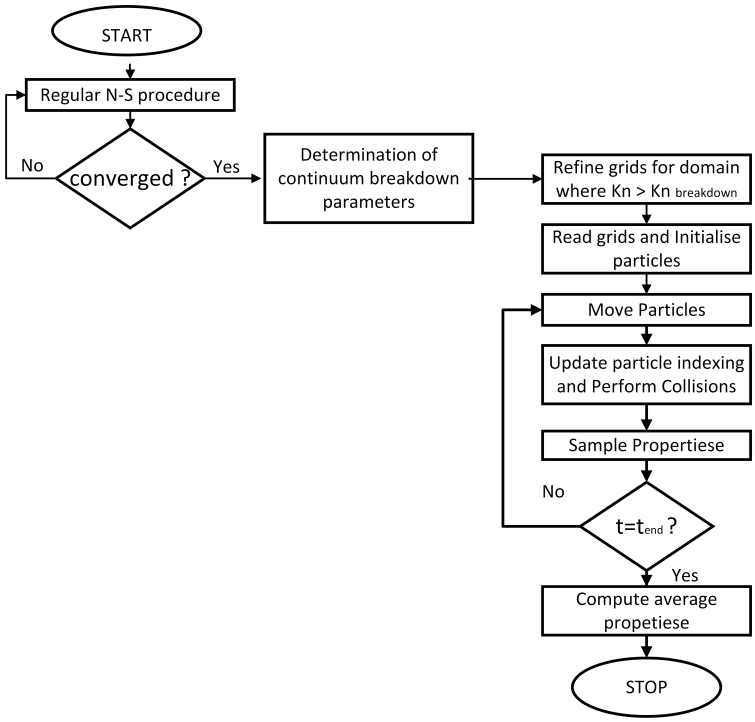

Figure 3.7: Hybrid DSMC flow chart

is observed that the SF_6 distribution of cell size $\lambda/3$ almost traced the same line as $\lambda/6$ with less computational effort. Therefore an optimum cell size of $\lambda/3$ has been selected for further studies.

3.4.2 Selection of no. of particles per cell

The particle independence study has been conducted on a $\lambda/3$ cell grid with particle numbers ranging from 10 to 30 per cell. The normalised SF_6 concentration on line 2 of 10 particles per cell simulation was found to be deviating from the simulation results having 20 and 30 particles per cell. This is clearly portrayed in Fig 3.8. Twenty particles are selected as the optimum number per cell with considerable accuracy and less computational effort.

3.4.3 Selection of time step

Three time steps such as t, t/10, and t/20 are selected for the time step independence study. Where 't' is the mean collision time which is calculated based on equation 3.10. From this study, t/10 is selected as the optimal time step for further studies. The same set of studies

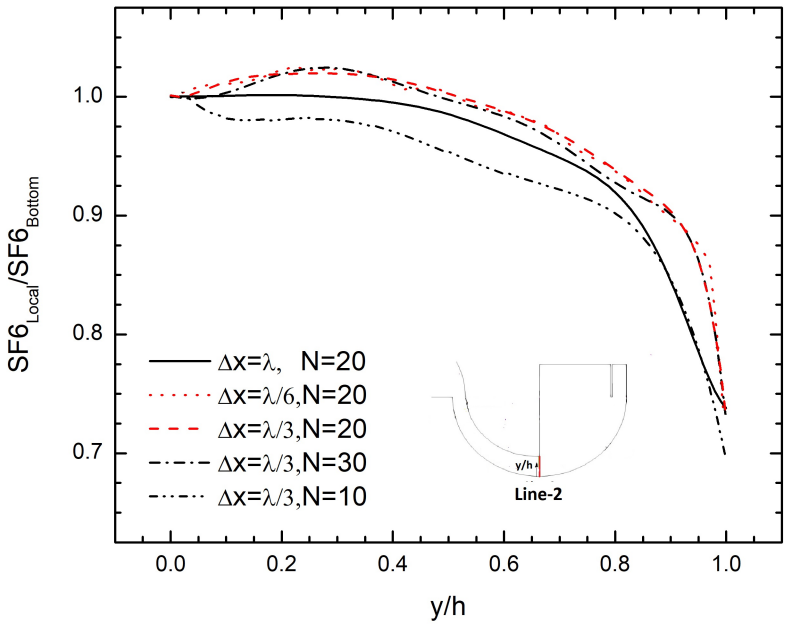

Figure 3.8: Grid and no. of particle independence analysis for the DSMC solver

is conducted for all the geometries employed in the present research, and the results are found to be consistent.

3.5 Grid independence study for N-S

For the Navier Stokes solver, a grid independence study has been conducted by varying the number of grids in geometrical progression for all geometries considered, and the results from a rectangular micro nozzle with h_t = 20μm and θ_d = 15° are shown in Figure 3.9. Studies are conducted for a pressure ratio of 1.43 and the centreline pressure and velocity are compared. Results from medium and fine grids are similar with less than a 0.1% difference between them and therefore medium grids are selected for subsequent simulations. For all the N-S simulations conducted, the Courant's number is kept below 0.5.

The following details will justify the selection of parameters for the numerical study

1. Grid Selection: The grids have been chosen based on a grid independence study. This ensures that the grid resolution is adequate to accurately capture the flow features and that the results are not overly sensitive to grid variations.

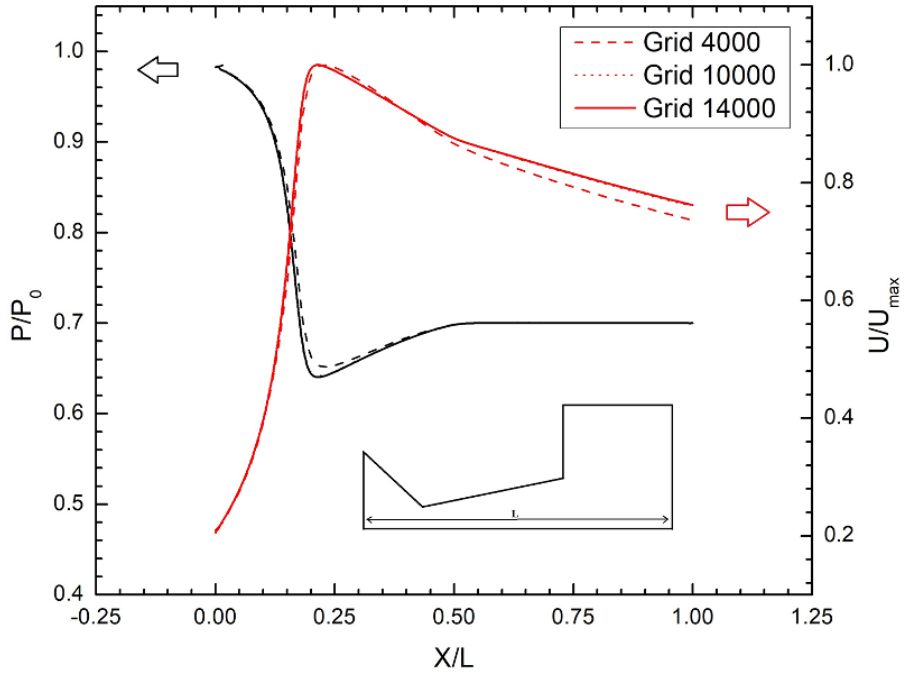

Figure 3.9: Grid independence study for a rectangular micronozzle with h_t = 20 μm and θ_d = 15°

2. Time Step Selection (Navier-Stokes Simulations): The time step is selected to maintain the maximum Courant number (CFL) of the flow below 0.5 for Navier-Stokes simulations. This is a common practice to ensure numerical stability and accuracy in solving the governing equations.

3. Time Step Selection (DSMC Simulations): The time steps for DSMC studies have been determined through a time step independence study. In DSMC, individual particle collisions are modeled, and the time step should be small enough to capture these interactions effectively. This ensures that the time step is suitable for the specific simulation and does not introduce significant errors.

4. Flow Parameters: The choice of flow parameters like pressure, temperature, etc., is consistent with previous experimental studies. This helps in maintaining continuity and comparability with existing research.[Hao et. al.[34], Li et.al.[182]].

5. Solver and Schemes: The selection of the rhoCentralFoam solver with different schemes is based on its proven accuracy and computational efficiency in previous micronozzle flow simulations [J.M Pearl [155].

6. Particle Count in DSMC Simulations: A particle independence study has been conducted and the results are shown in Figure 3.4. A minimum of 20 particles per cell has been selected for DSMC simulations to reduce errors and ensure a reliable representation of particle interactions within the simulation domain. The details are provided in the section 3.4.2.

These justifications reflect a systematic approach to parameter selection, ensuring that the simulation setup is both reliable and consistent with established practices in the field.

3.6 Validation of the computational models

The suitability of using the Navier stokes with slip boundary condition and DSMC method for the micronozzle simulation is verified using the experimental results of Hao et al.[34], Rothe [18], Li et al.[182], and also with the in-house experimental data and an analytical results of Piekos and Breuer [194].

3.6.1 Validation of Navier Stokes methodology

Due to the limited number of experimental studies available on the micro nozzle for validation, currently, a newly made experiment is conducted to measure the plume velocity at a distance of 2.5,3.5, and 4.5mm away from the nozzle exit. The fabricated micronozzle is used for the experimental study and measurement has been taken by using an Interferometric Rayleigh scattering method as described in Section 3.2. The numerical simulations are done by using a Navier Stoke's solver rhoCentralFoam with no-slip boundary conditions. The rhoCentralFoam solver is a density-based solver available in the open-source CFD software OpenFOAM-6. Pressure boundary conditions are applied at the inlet and exit of the domain. A pressure of 3.5 bar is applied at the nozzle inlet and the exit domain is kept at the atmospheric pressure. The nozzle dimension and validation results are shown in Fig. 3.2 and 3.10 respectively. The maximum variation of the velocity is observed to be below 4% for a 3.5 bar inlet pressure.

3.6.2 Validation of DSMC method

The DSMC methodology has been initially validated with analytical and numerical solutions of Piekos and Breuer [194] by simulating a microchannel flow. The experimental study of Li et al.[182] is also reproduced numerically and the details of the studies are given below.

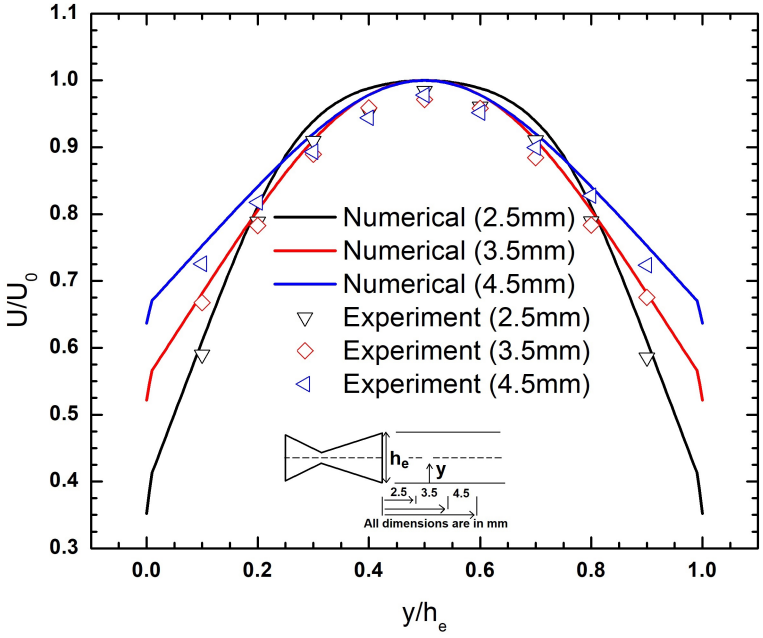

Figure 3.10: Comparison of nozzle exit velocity with Interferometric Rayleigh Scattering experimental data

Microchannel

Piekos and Breuer [194] investigated the flow through the microchannel with slip and transition flow numerically and analytically. They compared the numerical results to the analytical solution of the Navier Stokes equations with first-order slip boundary conditions. For the slip flow problem, the exit Knudsen number was around 0.05. The results of Piekos and Breuer [194] are reproduced by simulating a microchannel with a length and height of 2μm and 0.4μm respectively. Nitrogen is used as the working gas. The current DSMC method exactly retraces the analytical findings of Piekos and Breuer for a pressure ratio of 2.5. The variation of centreline pressure over the nozzle length is given in Fig. 3.11.

Li's Nozzle

Li et al. [182] fabricated a curved nozzle of throat size 3.6 μm using photolithography and measured the separation performance of a 1% mixture of SF_6 in N_2. Li et al. [182] used mass spectrometry to determine the contents in the separated mixture. The nozzle

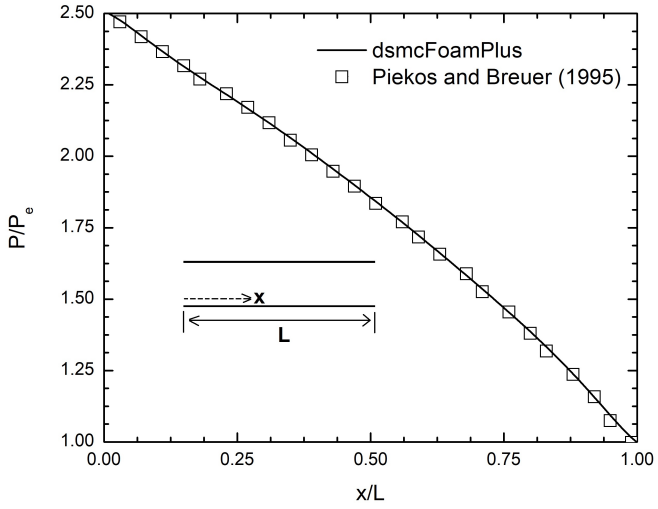

Figure 3.11: Comparison of centreline pressure in a microchannel with Piekos and Breuer

geometry is depicted in fig.3.12 The separation factor (A) can be calculated as follows

$$A = \frac{\theta_l(1-\theta_h)}{\theta_h(1-\theta_l)} \tag{3.25}$$

where θ_l and θ_h are light and heavy fraction partial cuts and they can be calculated from mass flow rates as follows.

$$\theta_l = \frac{\dot{m}_{l,light}}{\dot{m}_{l,light} + \dot{m}_{l,heavy}} \tag{3.26}$$

$$\theta_h = \frac{\dot{m}_{h,light}}{\dot{m}_{h,light} + \dot{m}_{h,heavy}} \tag{3.27}$$

Two different gas mixtures, $Ar + SF_6$ and $N_2 + SF_6$, were selected for the validation study. Pressure boundary conditions were applied at the inlet and exit of the domain based on the experimental conditions. Table 3.1 shows the numerically calculated separation factor (A) and the experimental results of the binary gas mixture. The maximum deviation was 21% which is lower than Li et al. [182]'s numerical model, which has a maximum error of 85%.

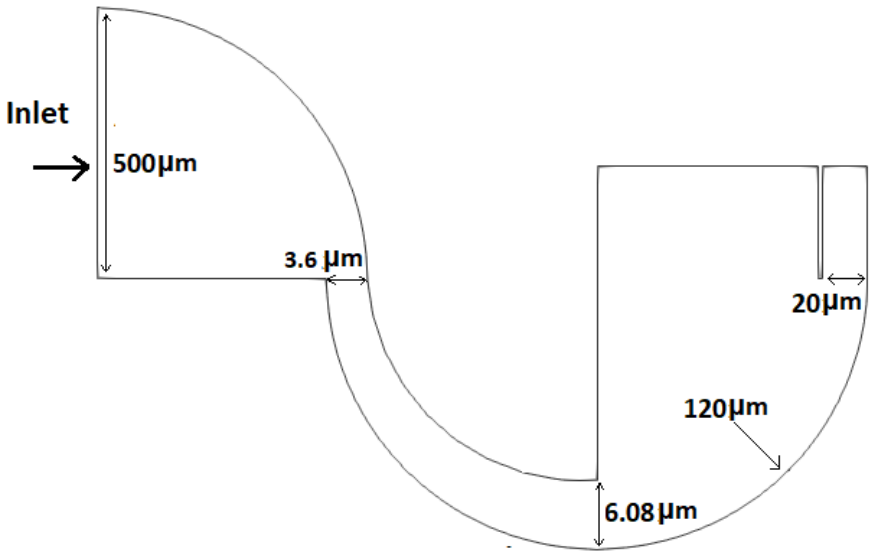

Figure 3.12: Nozzle geometry of Li et. al.[182]

Table 3.1: Separation factor for experimental, DSMC and Li Model-1

Δ P (atm)	$Mixture$	$A_{experiment}$	A_{DSMC}	A_{Li}	$Error_{DSMC}$	$Error_{Li}$
0.5	SF6+N2	1.1613	1.08	2.15	7%	85%
1.5	SF6+N2	1.6226	1.27	2.09	21.7%	28%
2	SF6+N2	1.3742	1.14	2	17%	45.5%
0.5	SF6+Ar	1.0732	1.07	-	0.29%	-
1.5	SF6+Ar	1.1794	1.09	-	7.5%	-
2	SF6+Ar	1.0637	1.1	-	3.4%	-

3.6.3 Validation of the hybrid approach

Hao's Nozzle

The current hybrid approach has been validated by comparing the experimental results of Hao et al [34]. The experiments were conducted with a rectangular cross-section CD micro nozzle, having a throat width of 20 μm for various outlet conditions. The nozzle details are shown in Fig.3.13a. Total pressure and temperature of 100kPa and 300 K are set at inlet and flow is established by varying outlet pressure from 0 to 90 kPa. The wall is maintained at 300 K. The Knudsen number value is calculated after completing a Navier Stoke simulation in the full micronozzle domain. The continuum is found to be broken down at the throat of the nozzle. So the DSMC simulation is carried out only in the divergent portion of the Hao's nozzle. The mass flow rate and pressure measurements upstream and downstream of the throat are compared with numerical predictions in Fig.3.13b. The measured values are

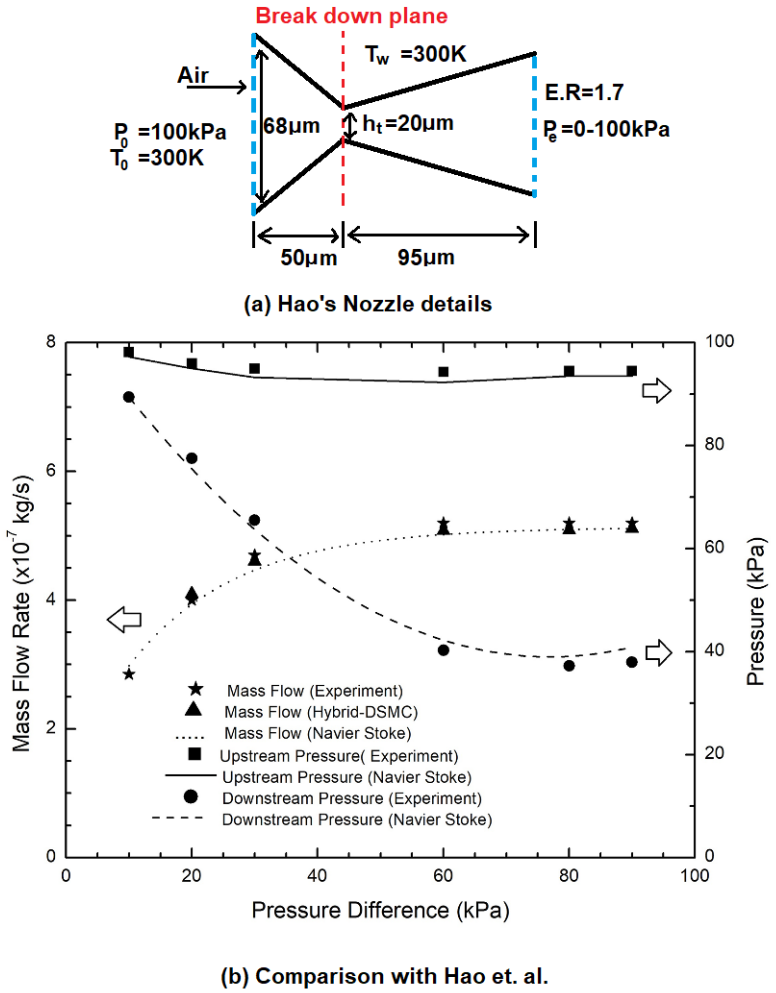

Figure 3.13: Validating computational methodology with the experimental studies of Hao et al.[33]

evaluation similar to Hao's nozzle, the continuum breakdown plane is located at the throat of Rothe's nozzle. The DSMC simulation is carried out downstream of the nozzle's throat. The centerline rotational temperature of the simulated nozzle is compared with the experimental results, and the maximum deviation is within 4%. The comparison is shown in Fig. 3.14b. The strong agreement between the predictions and the experimental results makes it possible to move forward with further investigation.

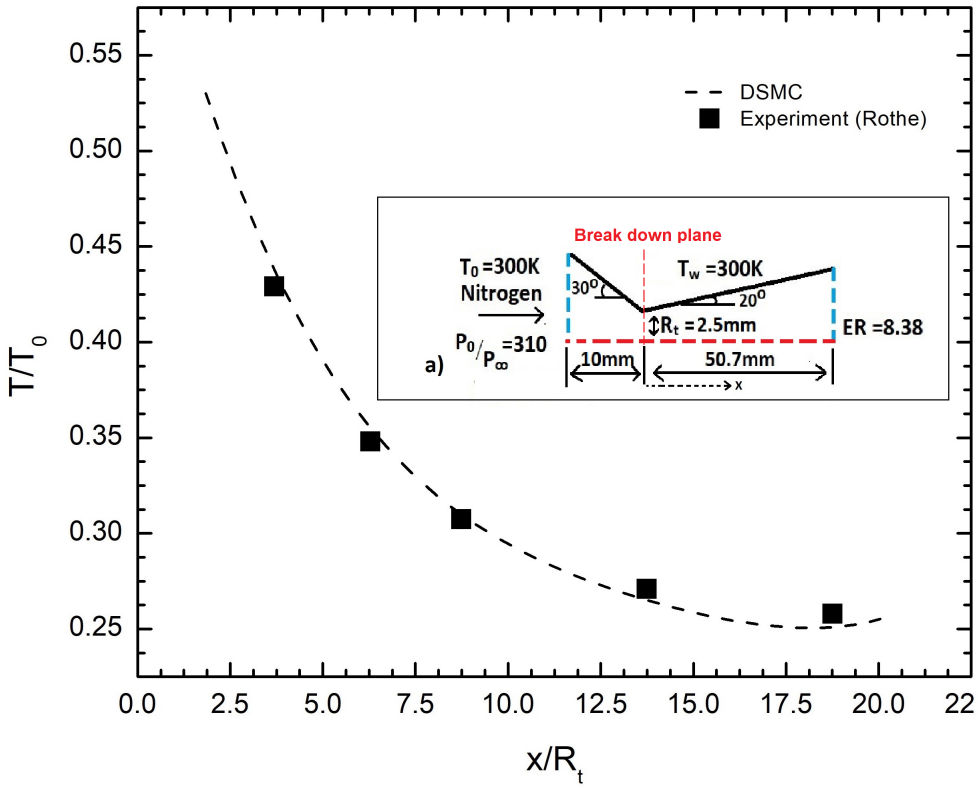

(b) Comparison with Rothe

Figure 3.14: Validating computational methodology with the experimental studies of Rothe [17]

3.7 Summary of micro nozzle geometries considered for the experimental and numerical studies

The numerical study on the planar micronozzle is conducted by varying throat height (h_t) from 2 to 200μm, divergent length (L_d) from 4.75h_t to 31.5h_t and divergent angle (θ_d) from 5 to 30° using suitable methods like Navier Stokes, DSMC, and hybrid approaches at different back pressure conditions. These studies are mainly conducted to identify an appropriate nozzle size for thruster applications. Only a limited number of experimental results are available on micronozzle flow, so an experimental study is conducted with h_t=500μm, L_d=6h_t, and θ_d=5° in an atmospheric back pressure condition with an inlet pressure of 350kPa. The effect of micronozzles operating in a cluster arrangement is also analyzed in vacuum exit conditions. A suitable size and shape of the micronozzle for species separation

are investigated with linear, bell, and trumpet divergent shapes. The throat height(2-8μm), divergent length (4.75h$_t$-15h$_t$), and divergent angle (θ_d=15-45°) changed along with different back pressures (0-30kPa). Later this study extended to a curved micronozzle with different radii of curvature (100-140μm) and back pressures ranging from 0-20kpa. Table 3.2 summarizes the different types of geometry studied, the parameters considered, the operating conditions, and the methodologies adopted.

The chosen parameters have been carefully configured to encompass both subsonic and supersonic flow regions within the divergent section of the nozzle. This deliberate selection allows for the examination of flow patterns for both types of flow. Furthermore, the dimensions of the nozzle have been systematically varied to investigate the impact of these dimensions on nozzle flow and the resultant thrust. Additionally, a study on wall temperature has been conducted to explore the influence of temperature on the viscous boundary layer and thrust. This investigation aims to propose optimal flow parameters and nozzle sizes for maximizing thrust and specific impulse within the studied flow regime. In a similar vein, the pursuit of an optimal nozzle size and shape is crucial for species separation within the studied flow regime. As a result, parameters affecting the separation process are identified, and proposals for an optimal divergent angle and shape are made to enhance the efficiency of species separation.

The appropriate size, shape, and dimensions of the micronozzle for the two distinct applications will be comprehensively discussed in upcoming chapters. Chapter 4 will primarily concentrate on the utilization of micronozzles in satellite applications, while Chapters 5 and 6 will delve into the use of micronozzles for species separation.

Table 3.2: Outline of the studies conducted in the thesis

Sl No.	Geometry considered	Method adopted	Geometry parameters	Working gas	Operating condition
1	Planar Nozzle	NS with Slip boundary	h_t=20-200μm, L_d=4.75h_t -31.5h_t, θ_d=5-30°	Air	P_i=100kPa, P_e=30 & 70 kPa
		Hybrid method	h_t=10-20μm, L_d=4.75h_t -31.5h_t, θ_d=5-30°	Air	P_i=100kPa, P_e=30 & 70 kPa
		DSMC	h_t=2μm, L_d=4.75h_t -31.5h_t, θ_d=5-30°	N_2+O_2	P_i=100kPa, P_e=30 & 70 kPa
		Experiment	h_t=500μm, L_d=6h_t, θ_d=5°	Air+ Acetone	P_i=350kPa, P_e=100kPa
2	Planar nozzle in cluster arrangement	DSMC	h_t=20μm, L_d=4.75h_t, θ_d=30°	N_2	P_i=1000 Pa, P_e=0 Pa
3	Planar Nozzle with linear, bell and trumpet divergent section for species separation	DSMC	h_t=2-8μm, L_d=4.75h_t-15h_t θ_d=15-45°	Ar + He, Carrier gas-N_2,Kr	P_i=120 kPa, P_e=0-30 kPa
4	Curved nozzle for species separation	DSMC	h_t=12μm, R=100-140μm	SF_6+N_2	P_i=100 kPa, P_e=0-20 kPa

Chapter 4

Flow characteristics of micro-scale planar nozzles

This chapter describes the studies on utilizing linear micronozzles for satellite thruster applications. An extensive examination of numerous micronozzle configurations operating under different exit conditions is conducted. Specifically, the chapter discusses the flow characteristics through 2-D micronozzles with varying throat depth, divergent angles, and length while considering different operating conditions. The effects of flow parameters such as back pressure and wall temperature are also analyzed. An empirical relationship is proposed to predict the thrust per unit width in the studied flow regime. Furthermore, the chapter explores the study of micronozzles arranged in clusters, investigating the impact of varying pitch and wall temperature on the nozzle performance.

This chapter is based on

1. M. K. Sukesan, S R Shine, Geometry effects on flow characteristics of micro-scale planar nozzles, *Journal of Micromechanics and Microengineering*, 31(12),2021, https://doi.org/10.1088/1361-6439/ac2bac

2. M. K. Sukesan, S. R. Shine, Plume interaction study on a cluster of heated Micronozzles , *proceedings of the 26th national and 4th International Heat and Mass Transfer Conference (2021)*, IIT Madras.

4.1 Introduction

Micronozzle has a thick boundary layer dominated flow which is fundamentally different from conventional nozzles. The major design constraint is the build-up of the boundary

layer, calling for a design optimization involving nozzle throat dimension, divergence angle, length of the divergence section, and expansion ratio. The current literature shows heterogeneous findings related to optimized divergence angles. It is noted that this is highly influenced by the overall size and operating conditions prevailing. The present study attempts to generate a unified analysis by simulating a large number of micronozzle configurations operating under various exit conditions. A numerical investigation of geometry effects on the flow characteristics associated with converging- diverging 2D planar micronozzles is analyzed. The classical N–S with linear slip model, DSMC method, and a hybrid N–S/DSMC based on the continuum breakdown concept are employed for the simulations. The study addresses the issue of heterogeneous findings on optimized half divergence angles recommended by previous studies.

4.1.1 Geometry and parameter selection

A study on small-sized micronozzles, similar to the one conducted by Hao et al. [34], was undertaken. In this experiment, the nozzle operated with an inlet pressure of 100kPa and various back pressures ranging from 0 to 90kPa. The same flow parameters were employed in the current investigation. To assess the nozzle's performance, two different back pressures of 70kPa and 30kPa were applied at the nozzle exit, resulting in the generation of subsonic and supersonic flows respectively in the divergent section. The nozzle dimensions employed in this study were in line with those used in Hao's original experiments. Furthermore, the research involved in-depth numerical analyses by scaling the nozzle size, reducing it to 1/2, 1/10, and increasing it to 10 times the initial size. The flow characteristics were meticulously examined, and thrust values were computed for the micronozzle at various dimensions.

The analysis is conducted for various throat dimensions (2–200μm throat height), divergence angles (5°–30°), and divergence length. The performance and flow characteristics are compared at two distinct operating conditions, i.e. when the flow is mostly subsonic and supersonic in the divergent section. The geometry considered along with the mesh details and boundary conditions for the N–S solver is shown in Figure 4.1. Pressure boundary conditions are applied at the inlet and exit of the domain and the wall is selected as completely diffusive. Due to the symmetry of the computational domain, only half of the domain is simulated with symmetry boundary conditions at the center of the nozzle. Necessary grids are generated using the blockMesh utility of OpenFOAM.A total of 120 simulations are conducted and analyzed for the current study. The table 4.1 containing details of the

simulation and the results are discussed in the subsequent sections.

Table 4.1: Details of the computational studies conducted in this chapter

Sl no.	Geometry Considered	Method Adopted	Geometry Parameters	No. of Simulations	Approximate Computational Hours
1	Planar nozzle	N-S with a slip boundary	h_t=20-200μm, L_d=4.75h_t - 31.5h_t, θ_d=5-30°	58	1392
		Hybrid method	h_t=10 - 20μm, L_d=4.75h_t - 31.5h_t, θ_d=5-30°	27	5184
		Full DSMC	h_t=2μm, L_d=4.75h_t - 31.5h_t, θ_d=5-30°	27	162
2	Planar nozzle in cluster arrangement	Full DSMC	h_t=20μm, L_d=4.75h_t , θ_d=30°	8	3840

4.2 Analysis with constant L_d /h_t ratio

Comparison of N–S solver with slip and no-slip boundary conditions, coupled Navier–Stokes, and DSMC (hybrid) and full DSMC simulations have been conducted for a micronozzle of throat height of 0.2 μm . Simulations are conducted for inlet/exit pressures of 250/100 kPa with pressure boundary conditions. Slip boundary conditions are employed with Maxwell's first order slip having an accommodation coefficient of 0.9. Figure 4.2 shows the centerline pressure and velocity of the divergent portion of the nozzle for all cases. The full DSMC, hybrid, and NS simulation with slip boundary conditions are showing a close agreement. In order to verify the continuum assumption, the local Kn is obtained from the DSMC simulation for the h_t = 2 μm nozzle operating at a pressure difference of 70 kPa. The result is analyzed for 30° nozzles having an area ratio of 6.5. Kn contours are shown in Figure

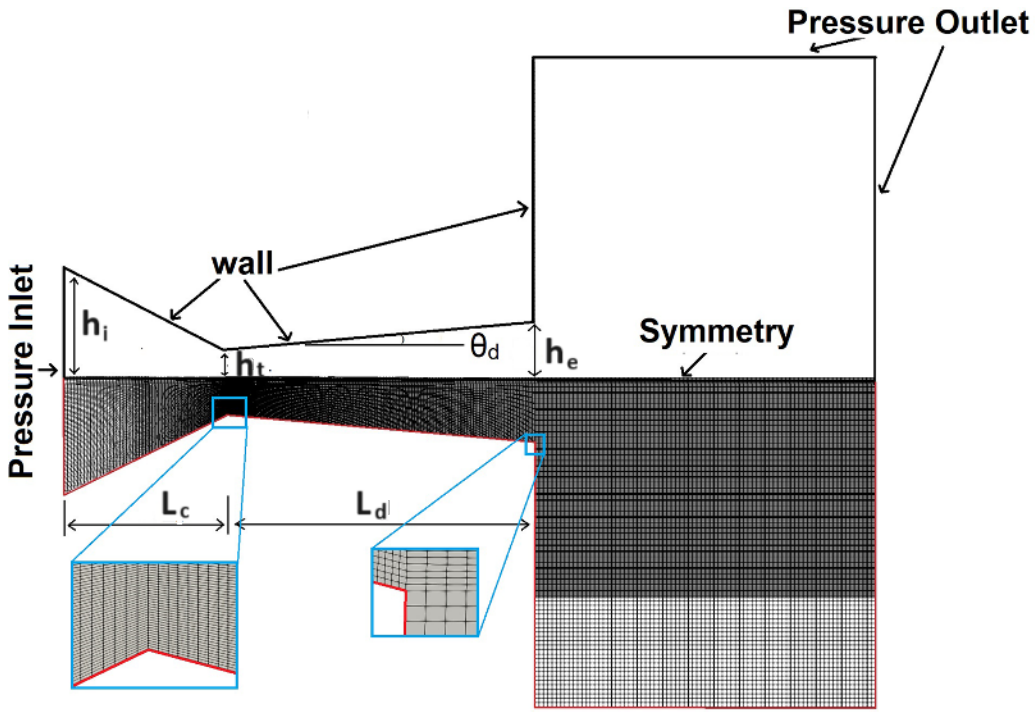

Figure 4.1: Geometry of micronozzle with boundary conditions of the N–S solver

4.3, and the highest Kn of 0.023 is observed downstream of the throat. Kn over the range of operation variation is 0.003 to 0.023, which justifies the first order slip assumption. Micronozzle is operating well within the limit of the continuum regime. However, wall slip velocity may become significant downstream of the throat.

The literature on micronozzle flow shows that the viscous effects significantly affect the micronozzle performance. Therefore flow features are analyzed with constant L_d /h_t for nozzles having h_t = 2, 10, 20, and 200 μm. The L_d /h_t ratio is kept at 4.75 for various divergent angles of 5°–30°.

4.2.1 Internal flow features

The major flow features of the internal flow are investigated in detail here. Simulations are conducted at two different pressure differences P_o – P_b = 30 kPa and 70 kPa, in order to distinguish the flow features when the flow in the divergent section is mostly subsonic or supersonic. The inlet pressure is maintained at 100 Kpa. Figure 4.4 shows streamlines and Mach number contours for various micronozzles for the two operating conditions. Clear

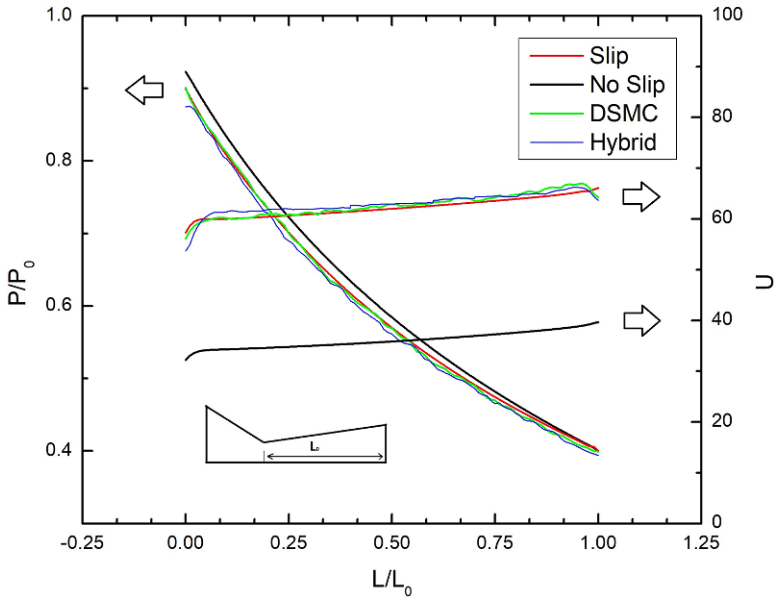

Figure 4.2: Comparison of various computational models

flow separation can be noticed for the bigger nozzles at higher pressure differences. It also shows a shock wave structure, shift of the sonic line downward of the throat, and recirculation zones. These effects become more substantial with the increase in throat size. It is seen that the number of Mach cores increases as the throat dimension increases. The presence of Mach cores is seen at higher pressure differences only. Other notable features are (a) decay of Mach core strength towards the exit, (b) existence of separated flow at most of the divergent section, (c) almost equal area coverage of the separated and unseparated region at the nozzle exit, and (d) negligible effect of the divergent shape on flow features. The substantial impact of rarefaction and viscosity effects keep the shock waves away from the wall and make the flow similar to a conduit flow. In other cases, i.e. for the smaller throat and low-pressure differences, the thicker boundary layer prevents the separation of boundary layers. For the smaller nozzle, at a 30 kPa pressure difference, the reduction in the effective area due to the presence of the viscous boundary layer causes the effective minimum cross-section downstream of the throat. Therefore the flow reaches a maximum Mach number of 0.45 downstream of the throat and decelerates in the divergent section. The thick boundary layer and higher rarefaction effects contribute to the flow behavior significantly. The boundary layer thickness is higher relative to the nozzle dimensions and produces a shock-less decrease of Mach number and velocity. For the 200 μm nozzle at a 30 kPa pressure difference (as seen in Figure 4.5), flow is accelerating in the divergent

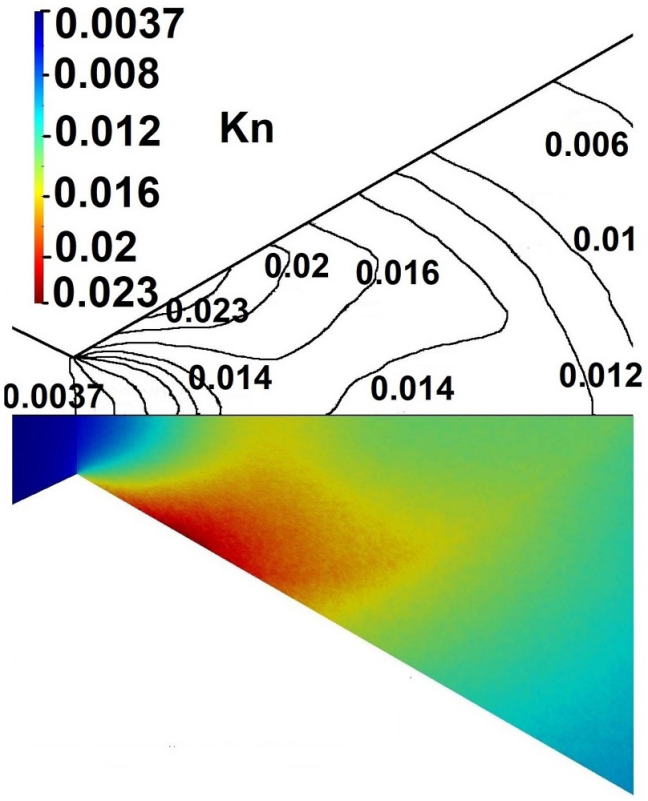

Figure 4.3: Knudsen number contours for the $h_t = 2\mu$m, $\theta_d = 30^\circ$ micronozzle operating at 70 kPa pressure difference

section, though it is entirely in the subsonic regime, which is unexpected.

The thick growing boundary layer reduces the effective area available for the core flow and creates a convergent shape effect for the subsonic flow in the divergent section. When the exit boundary layers are subsonic, the backpressure and the ambient flow field might communicate to the upstream. This can result in flow turning, deflection of exit momentum in the transverse direction, and degradation of performance. Various vortices are seen inside the viscous boundary layer and near the corner of the exit plane. The boundary layer mainly occupies the flow field with backflow. Figure 4.6 shows the Re variation for the different micronozzles at the two operating conditions.

When the flow is mostly subsonic, the effect of viscous forces is predominant. At higher divergence angles, the growing boundary layer decreases the effective flow area, resulting in decreased flow rate and Re. Re shows an asymptotic behavior based on the throat di-

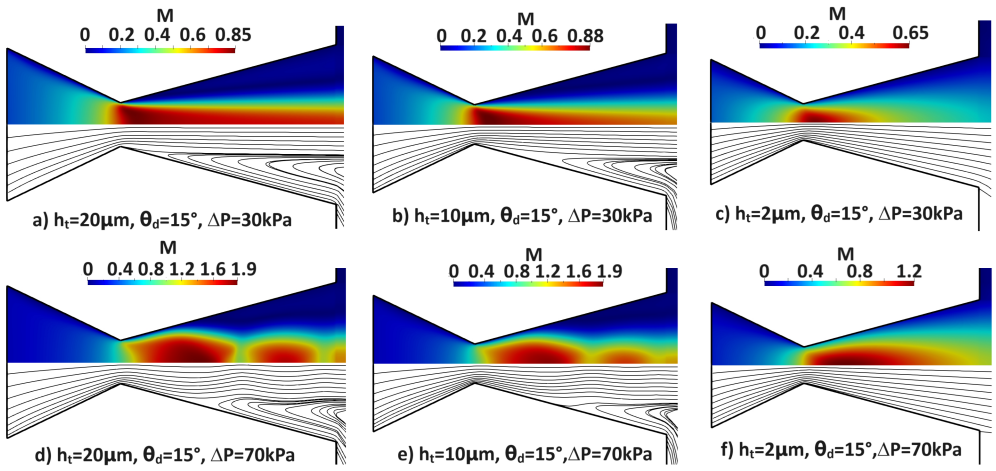

Figure 4.4: Streamlines and Mach number contours for micronozzles with h_t = 2, 10, and 20 μm, and θ_d = 15° for two operating conditions.

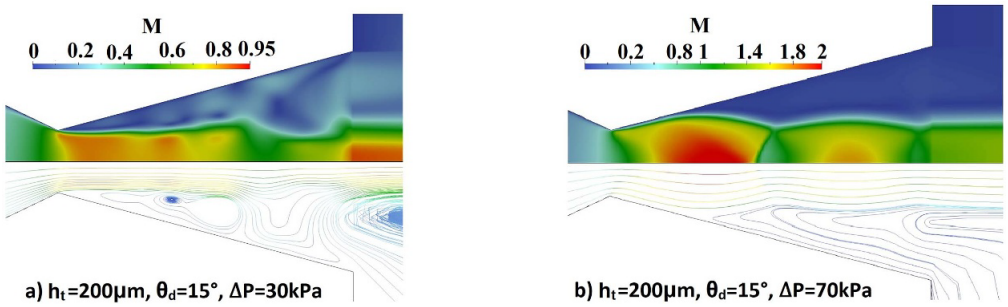

Figure 4.5: Streamlines and Mach number contours for micronozzles with h_t = 200 μm and θ_d = 15° for two operating conditions

mension. This effect is not severe at supersonic flow conditions and shows a slight increase in Re with an increase in divergence angle. Figure 4.7 shows the Mach No. and pressure variation at the throat for three two nozzles having θ_d = 15° at the two operating conditions. Mach number and pressure at the throat are significantly different while operating at a 30 kPa pressure difference. Similar behavior can also be seen in the throat temperature as depicted in figure 4.8. Therefore it can be concluded that the micronozzle size effect is predominant at lower pressure differences. Sonic conditions have not been attained at the throat in all cases.

The internal flow features of the micronozzles can be summarised as follows. There is

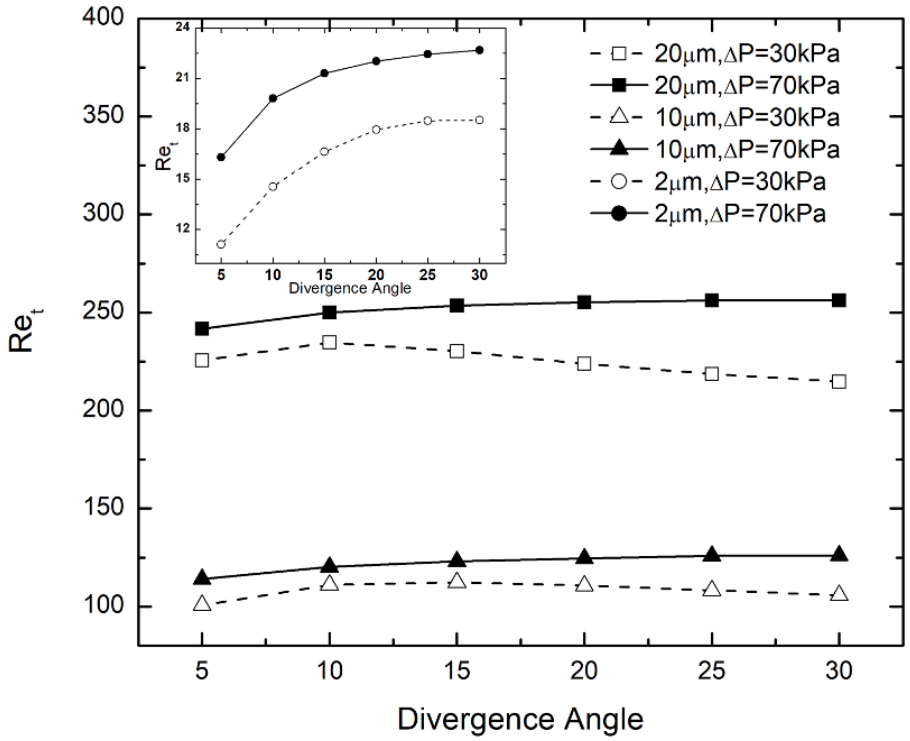

Figure 4.6: Re variation for the different micronozzles at P_0 –P_b =30 kPa and 70 kPa.

a substantial difference in flow characteristics when the micronozzle is operating at high and low-pressure differences. At low-pressure differences, the flow is primarily subsonic throughout the nozzle; however, it accelerates in the divergent section due to the effective area reduction caused by the growing boundary layer. During these operating conditions, the flow turning and deflection of exit momentum cause further degradation of performance. The losses will increase with the increase in divergent angles. In the divergent section, the flow is supersonic at high-pressure differences, with clear boundary layer separation at higher throat dimensions. However, the separation phenomenon and the Mach core formation are less pronounced at the microscale than the conventional nozzle due to rarefaction and viscosity effects. The resulting shockwaves are weak.

4.2.2 Effect of divergence angle

This section discusses the effect of divergence angle for various nozzles at the two operating conditions mentioned in the previous section, i.e. when the flow in the divergent section is mostly subsonic (ΔP = 30 kPa) or supersonic (ΔP = 70 kPa). Figure 4.9 shows the predicted thrust per unit depth from micronozzles with ht = 2, 10, and 20 μm for various

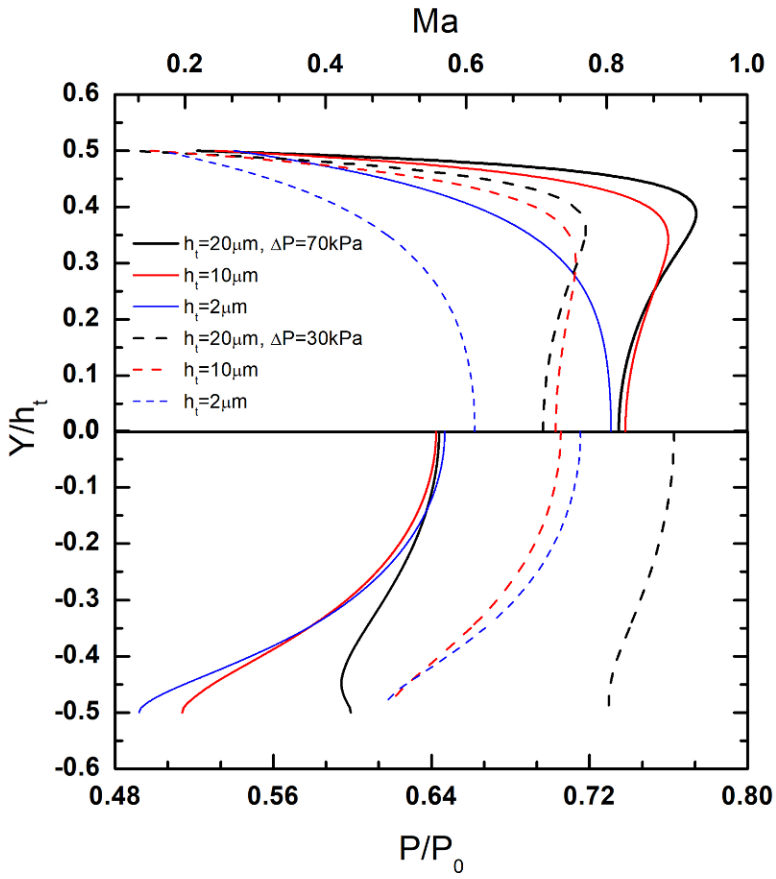

Figure 4.7: Comparison of Mach No. and pressure at the throat for the three micronozzles at the two operating conditions

half-divergent angles (5° to 30°) at the two operating conditions. As the L_d/h_t is kept constant for various cases, the exit is mostly covered by the subsonic layers caused by viscous forces. Therefore increasing the divergence angle causes higher viscous losses and a decrease in performance. The only exception is at 2 μm, where the half divergence angle of 10° shows the peak thrust production. The decrease in performance is more severe for bigger nozzles at higher divergence angles, and pressure differences. This suggests that divergence length needs to be carefully selected for optimizing performance. The mitigation of viscous losses is not aided by the increase in divergence angle due to the higher divergence length. The gains at small divergence angles due to axial flow alignment are negated by the viscous flow effects which demonstrate a performance trade-off between geometric and viscous effects. The substantial non-axial components of flow velocity at the nozzle exit also contribute to the thrust decrease at higher divergence angles.

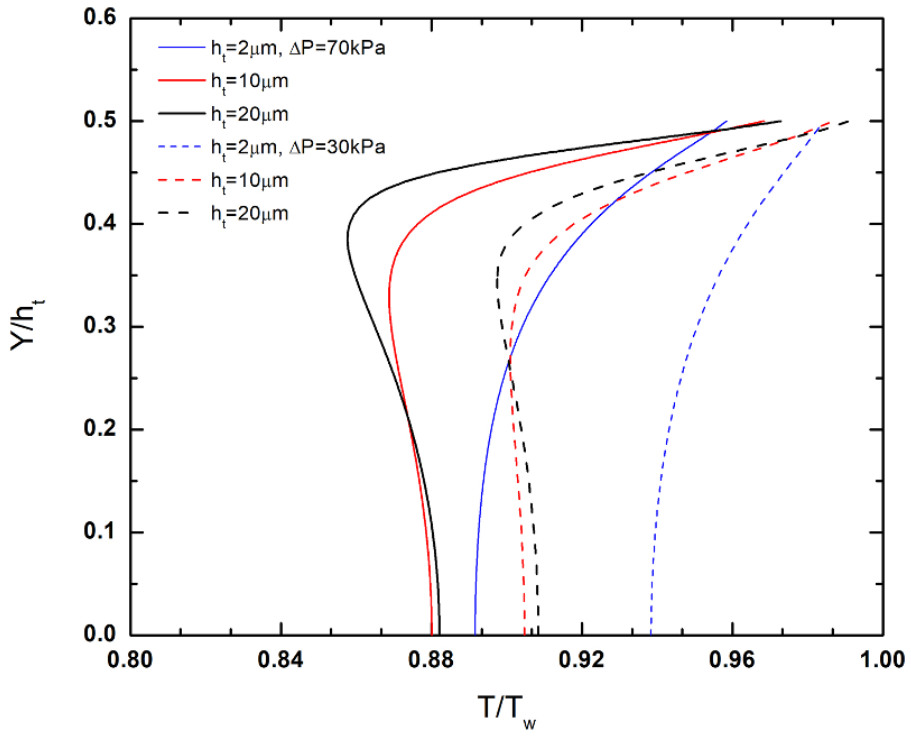

Figure 4.8: Comparison of exit plane temperature for the three micronozzles at the two operating conditions.

Figure 4.10 shows the normalized (normalized with average axial velocity in every case) v variation at the nozzle exit for the various cases. As the divergence angle increases, v increases significantly in the core flow region. The presence of a larger recirculation region can also be noticed at a higher divergence angle. The nozzle efficiency, which is defined as the ratio of the actual specific impulse to quasi-1-D specific impulse for a given pressure ratio is an effective parameter to compare varying geometries and operating conditions [85]. It is defined as

$$\eta = \frac{I_s}{I_s^{opt}} = \frac{T_h/mg}{\sqrt{2\gamma RT_0/[g^2(\gamma-1)][1-\frac{P_{exit}}{P_0}^{\frac{\gamma-1}{\gamma}}]}} \tag{4.1}$$

Specific impulse efficiency, η of various cases is plotted in Figure 4.11. η is very low at higher divergence angles due to the dominance of viscous losses as mentioned in earlier sections. Improvement in efficiency is noted at higher micronozzle depth but drops significantly as the divergence angle increases. In summary, viscous losses are predominant at lower divergence angles, whereas at higher angles, both viscous losses and non-axial velocity components contribute to thrust decrease. These losses are increasing with an increase

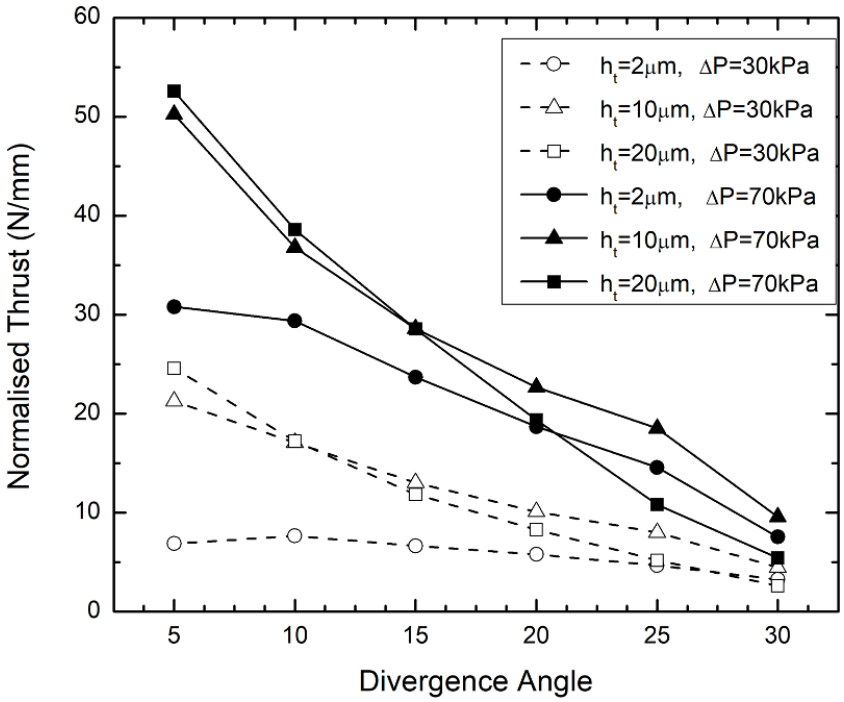

Figure 4.9: Comparison of thrust production per unit depth at constant divergence length

in nozzle length. When the divergent length is more, the increase in divergence angle does not contribute to performance improvement. This is mainly due to the higher viscous losses caused by the substantial backflow present at the divergent section. The performance loss is severe for higher throat size and low back pressure. This suggests that the truncation of nozzles is very important for optimizing the performance, especially at higher divergence angles.

4.2.3 Effect of pressure difference

The effect of pressure differences across the micronozzle with $h_t = 20\mu$m having a divergence angle of 5° and 15° is discussed. The Mach contours and streamlines for the pressure differences of 90, 50, and 10 kPa are compared in Figure 4.12 Comparing this result with Figure 4.4 (where results for 30 and 70 kPa are available), it is seen that the presence of high Mach cores in the divergent part is the main flow feature at higher pressure differences and higher divergence angles. However, the strength of the Mach cores decreases towards the exit. As the pressure difference increases, the boundary layer separation point and the first core move away from the throat. A wave interface is seen separating the inviscid core and the boundary layer with the backflow. The presence of strong viscosity effects does not al-

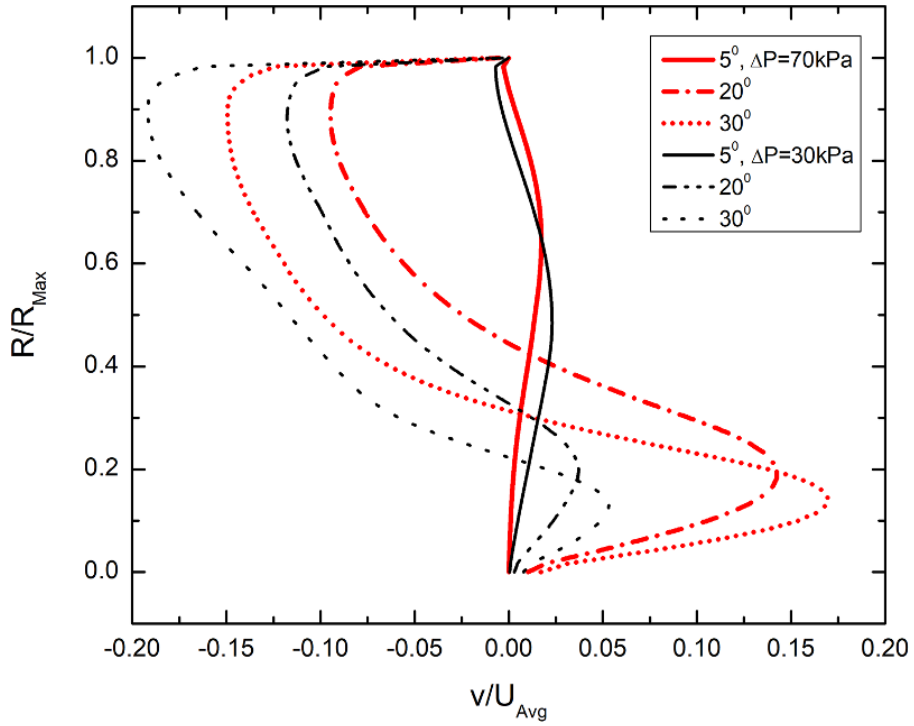

Figure 4.10: Variation at the nozzle exit for the various cases

low the shock waves to reach the wall and results in a series of high Mach cores. At a higher divergence angle, the separated flow occupies a considerable portion of the divergence section, and the flow is like a conduit flow. The thrust reduction at a higher divergence angle is severe at high-pressure drops due to the overall reduction in Mach number at the exit. The above findings are inconsistent with that of Xu et al[195], and Darbandi and Roohi [119].

Figure 4.13 shows the distribution of the centreline pressure under various pressure differences for the micronozzle having different divergence angles (5° and 15°), and throat height (h_t = 20 and 2 μm). For the bigger nozzle, under subsonic flow regimes, the effect of the divergence angle is insignificant. There is a substantial effect of divergence angle on the flow behavior under supersonic flow conditions. The formation of the Mach core, higher strength, and shifting of the first core away from the throat are visible at higher pressure differences. For the 2 μm nozzle, the flow behavior is different for the two divergent angles at all flow conditions. There is no Mach core formation observed in this case. The subsonic boundary layer region spreads up to the flow axis at higher pressure differences and degenerates the core isentropic flow. It may be due to the very low Re associated with smaller nozzles. The above observations demonstrate that enhanced viscous effects may lead to

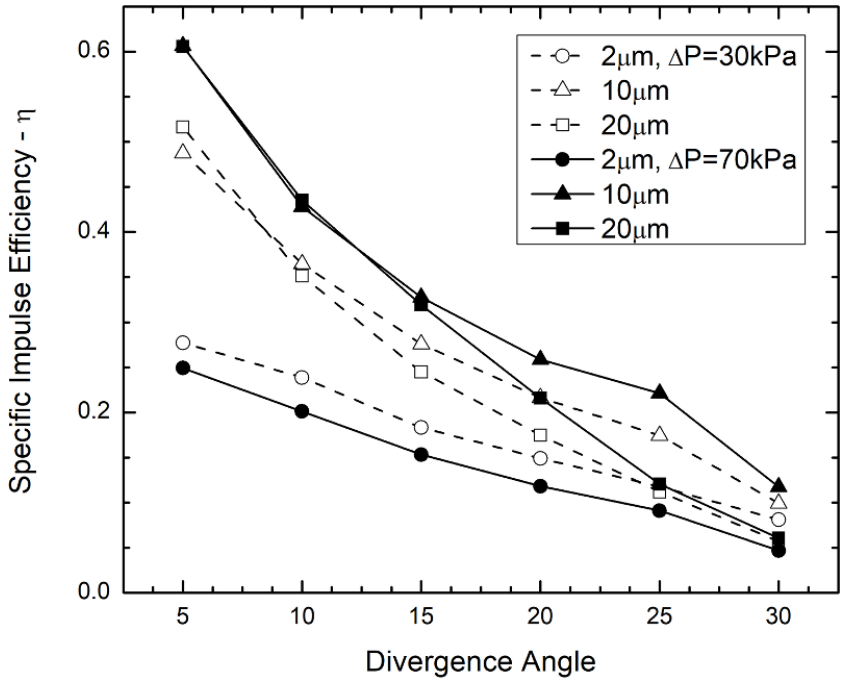

Figure 4.11: Comparison of micronozzle-specific impulse efficiency at constant divergence length

different flow behavior for micro-and nano-nozzles. It can be concluded that backpressure has a significant effect on micro and nanoscales. The impact of viscous forces, rarefaction, and compressibility effects contribute to the overall flow behavior. It is difficult to set up supersonic flow as the throat size decreases.

4.2.4 Error in thrust calculations

Pearl et al[196] proposed an extended method to include the viscous stress tensor's contribution along with momentum flux and pressure imbalance for the thrust calculation of micronozzles. This is necessitated by the presence of significant effects of various forces along with the supersonic flow in micronozzles. The proposed thrust equation is given by

$$T_h = \iint (\tau.n)dAe - \iint u(\rho u.n)dAe - \iint (P - P_\infty)ndAe \tag{4.2}$$

The contribution for the viscous term (first term of 4.2) is calculated assuming an arbitrary region outside the nozzle exit plane, but containing it. The thrust contribution from all the terms in equation 4.2) will be then calculated along all surfaces and thrust from the nozzle is determined using Newton's third-law-type pair. In the current 2D micronozzle,

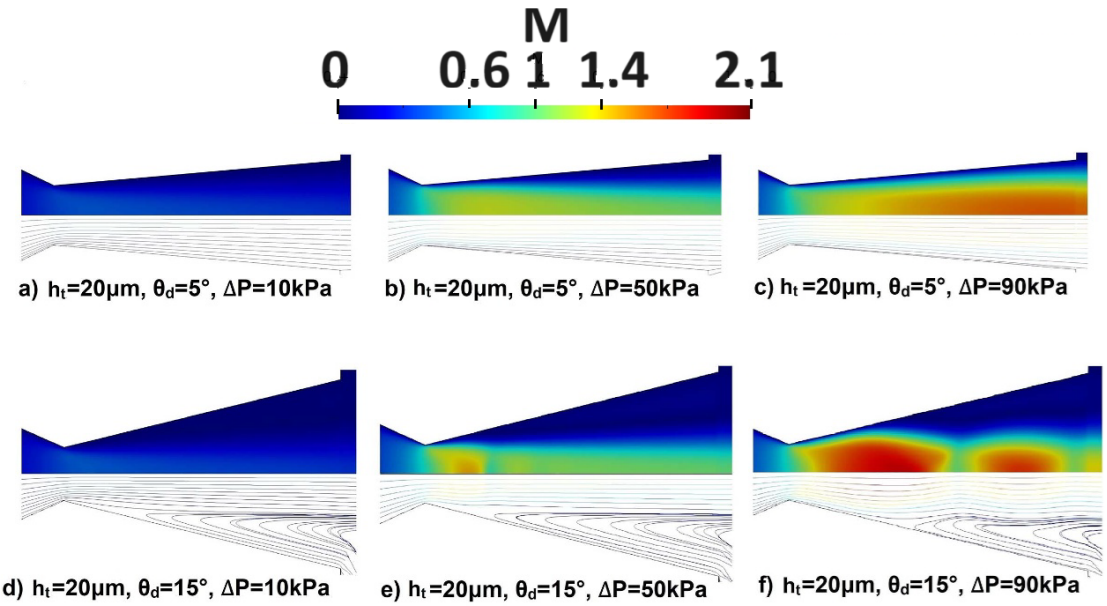

Figure 4.12: Streamlines and Mach number contours in $h_t = 20\mu$m micronozzle at different pressure differences at divergence angles of 5° and 15°

the exit plane perpendicular to the axis is taken for sampling field data.

Figure 4.14 shows the error associated with the classical method and the extended method for the 2 and 20 μm h_t nozzle for various operating conditions. The comparison is made for the divergent angle of 5° and 15°. As discussed in the previous sections, the geometry of the nozzle significantly affects the flow features and viscous stress field. The error is a function of the viscous stress field and is seen as predominant when operating at high back pressures (low-pressure difference) for the smaller nozzle, i.e. when the Re is very low. The error is due to the viscous stress component τ_{xx}, as the sample plane is perpendicular to the thrust axis. In real applications, when the effects are 3-dimensional, the error may be higher.

4.3 Analysis with a constant area ratio

This section analyses the performance of the micro nozzle at a constant area ratio. The analysis is done for various divergent angles of 5–30° with nozzle depths ranging from 2 to 20μm. The throat and exit of the micronozzle yield an area expansion ratio of 6.5 in all cases. The axial length of the divergent section is varied to maintain this constant area

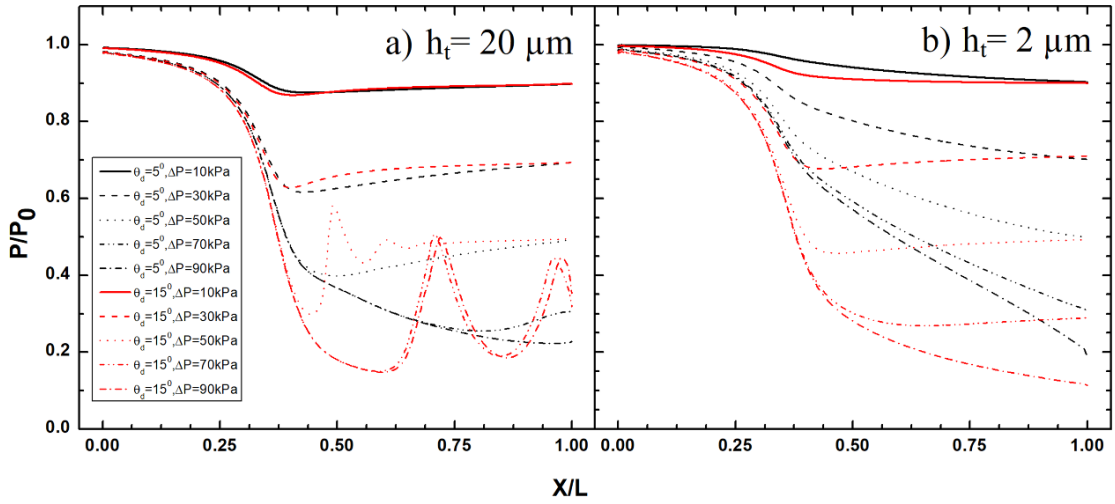

Figure 4.13: Centreline pressure distribution under various pressure differences for the micronozzles with different divergence angles (5° and 15°) and throat height (h_t = 20 and 2 μm)

ratio. The convergent length of the nozzle is kept at 2.5h_t.

4.3.1 Effect of divergence angle

Figure 4.15 shows the thrust produced per unit depth as a function of the divergence angle for all nozzles at the two operating conditions. It is evident that the optimum divergence angle for the highest performance depends upon the nozzle size and operating conditions. However, it falls in the range of 15°–25° for the current simulations. This suggests that the heterogeneous findings available in the literature regarding the optimized divergence angle are due to the variation in nozzle size, area ratio, length of the divergence section, and operating conditions associated with each study. A significant drop in the thrust is observed beyond 25°, which is a direct result of higher viscous losses and transverse velocity components. A higher divergence angle may be preferable at lower expansion ratios. For smaller divergence angles, the increased length due to the fixed area expansion ratio causes higher viscous losses. The optimum divergence angle is found to be decreasing as the nozzle size decreases. The flow is mainly subsonic under these conditions, and higher premature flow turning at the exit is observed. This creates vectoring of the exit momentum in the transverse direction. This effect increases with the divergence angle and results in a further reduction in performance.

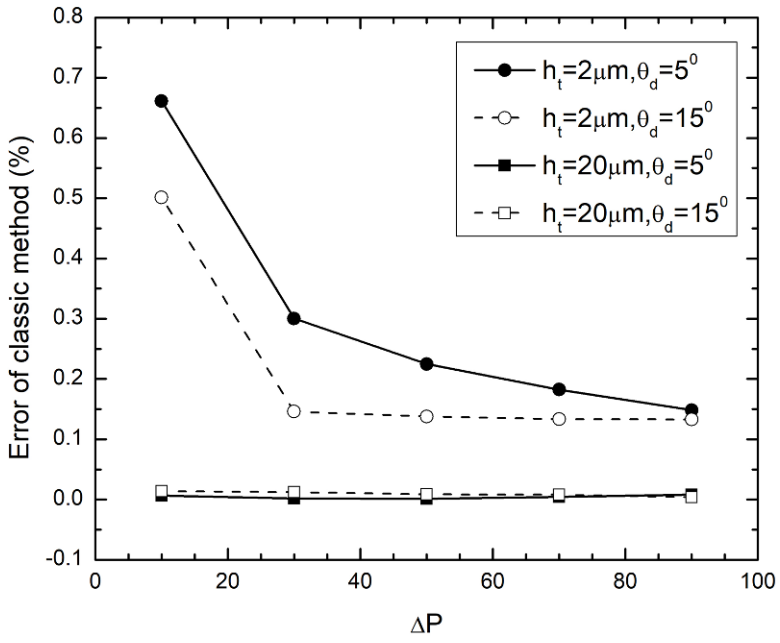

Figure 4.14: Percent error of the classical method of thrust calculation for the micronozzles with different divergence angles (5° and 15°) and throat height (h_t =20 and 2μm) at various operating conditions.

4.4 Comparison of constant L_d/h_t, and area ratio cases

A comparison of flow features for the two cases, (a) constant L_d/h_t, and (b) constant area ratio is given in Figure 4.16. The fraction of the subsonic layer at the nozzle exit plane is shown when the nozzle operates at a 70 KPa pressure difference. Subsonic layer thickness decreases with an increase in divergence angle for constant area ratio, whereas the layer thickness increases with an increase in divergence angle for constant divergent length. When the divergence angle is altered from 5 to 30° degrees, a 60.7% expansion in the subsonic layer is observed in the study of a constant divergent length for a 20μm nozzle. However, a decrease of 18% in the subsonic layer is observed in the study with a constant area ratio. Similarly, in the case of a 10μm nozzle, a 54.5% growth in the subsonic layer is observed with a constant divergent length, while a decrease of 15% is noted in the study with a constant area ratio. It can be observed that a higher pressure difference is required to create supersonic flow in the divergent section as the nozzle size decreases. This is evident from the fact that the 2 μm nozzle operates in the subsonic regime at all conditions simulated. For the 2 μm nozzle, the Re number is very low (20), and the differences in flow features are negligible. At these Re, the low rates are not sufficient to create super-

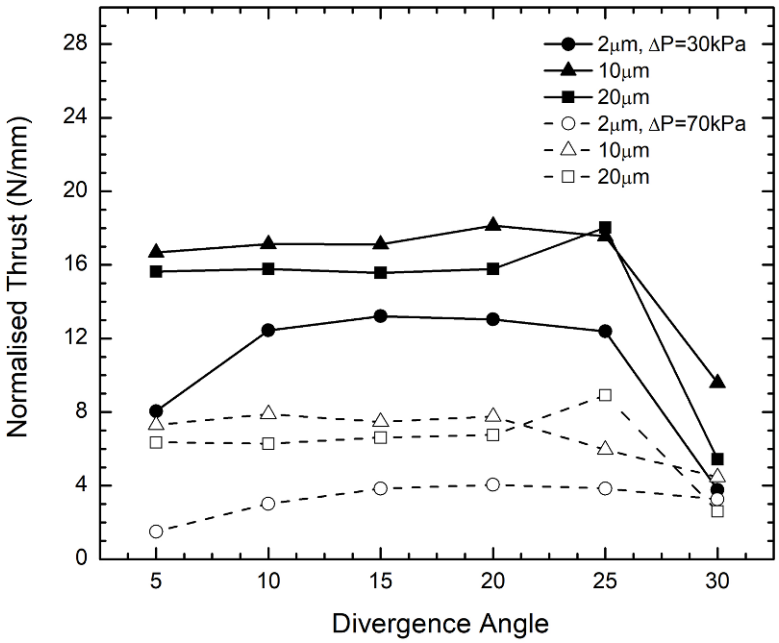

Figure 4.15: Comparison of thrust production for various micronozzles having constant area expansion ratio

sonic flow at the exit. It is also observed that even at higher Re = 100, there is a chance of merging the subsonic layers from the nozzle walls if the divergence length is higher. This is the reason for 100% subsonic exit for h_t = 10 and 20μm at lower divergence angles. The flow Re increases at higher divergence angles and nozzle size, and a reduction in the area occupied by the subsonic layer can be noticed. The shape of the constant L_d/h_t graph suggests that there exists a critical divergence length above which the merging of subsonic layers from the opposing walls occurs for a certain micronozzle depth. Therefore it can be concluded that the performance of micronozzles is dominated by viscous effects, and a careful selection of geometry is required to optimize the performance at a given operating condition.

4.4.1 Wall temperature effect

Simulations are conducted with wall temperature varying from 200 K to 600 K to deduce the effect of wall temperature on the size of the subsonic layer and the performance. Comparisons are done for a micronozzle having h_t = 20 μm, θ_d = 15°, and operating at a 70 kPa pressure difference. The subsonic layer size as a percentage of exit and the thrust produced is compared in Figure 4.17.

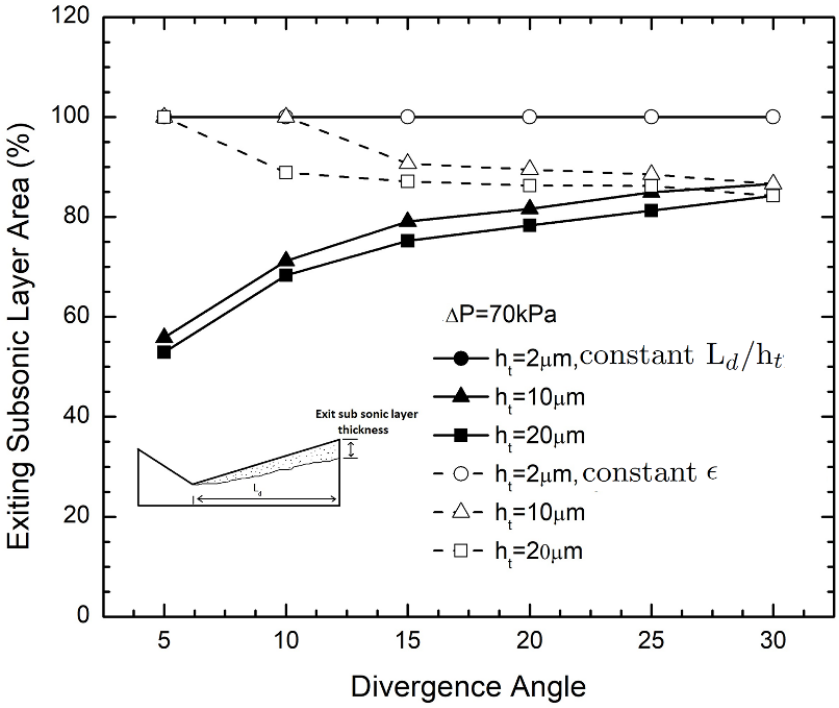

Figure 4.16: Percentage of micronozzle exit plane with Mach number M < 1 operating at 70 KPa pressure difference

The decrease in subsonic layer size with a reduction in temperature creates a performance improvement. At lower wall temperatures, heat loss will be more. The local sonic velocity decreases due to temperature decrease. This increases the local Mach number, which drives the reduction in the size of the subsonic layer. Therefore the optimum divergence angle will depend on the wall's thermal conditions. At lower wall temperatures, the density increases. This accelerates the flow and increases thrust production.

A significant change in the subsonic layer and flow features are noticed on the divergent section with the changes in wall thermal condition. A thrust decrease of around 5% was noticed for a wall temperature increase of 100 K. This brings the importance of considering the thermal coupling of solid-gas surface, conjugate wall, and external environmental conditions, especially in the simulation of microsatellite propulsion systems.

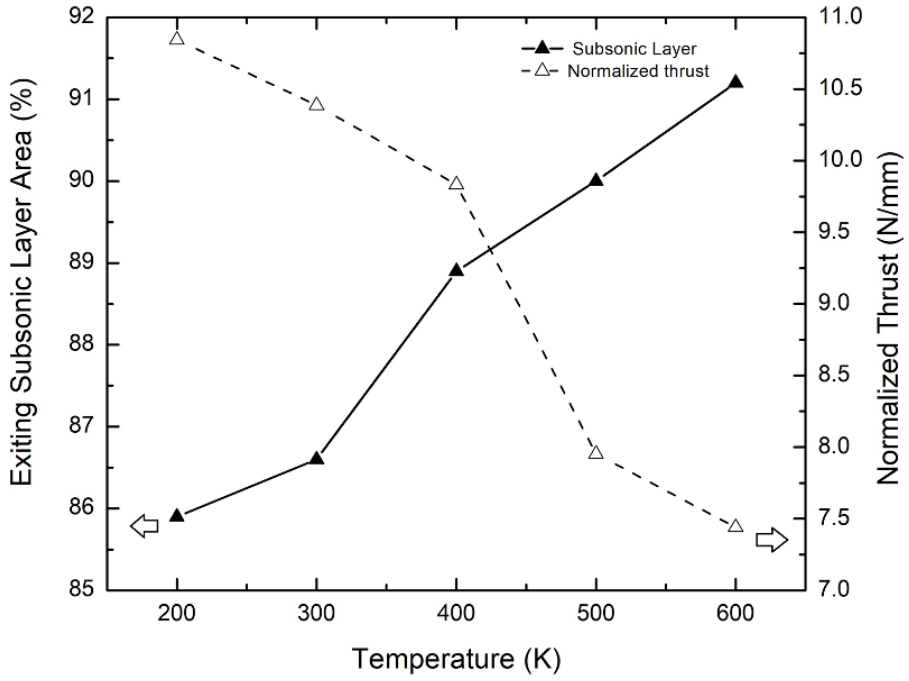

Figure 4.17: Percentage of micronozzle exit plane with Mach number M <1 and the thrust for the ht = 20 μm, θ_d = 15° at various wall boundary conditions

4.5 Correlation for thrust prediction

The total of 96 numerical simulations conducted has resulted in many data sets for micronozzle geometries having various throat dimensions, divergence angles, and operating conditions. It is observed that the performance is highly influenced by the area ratio, length of the divergent wall, and pressure difference across the nozzle. Therefore, the following performance parameter, X, is identified to relate to the thrust per unit depth produced. The parameter X is defined as

$$X = \frac{sin^2\theta}{AR^2}\frac{P_0}{\Delta P}\frac{\epsilon}{\epsilon - 1} \tag{4.3}$$

The proposed correlation for thrust per unit width can be expressed as follows

$$Thrust/width = AX^b \tag{4.4}$$

where A and b are 71 587.8 and –0.6 respectively. The correlation coefficient is 0.97. A comparison of the predictions of the proposed correlation with the data points obtained from the numerical analysis is shown in Figure 4.18.

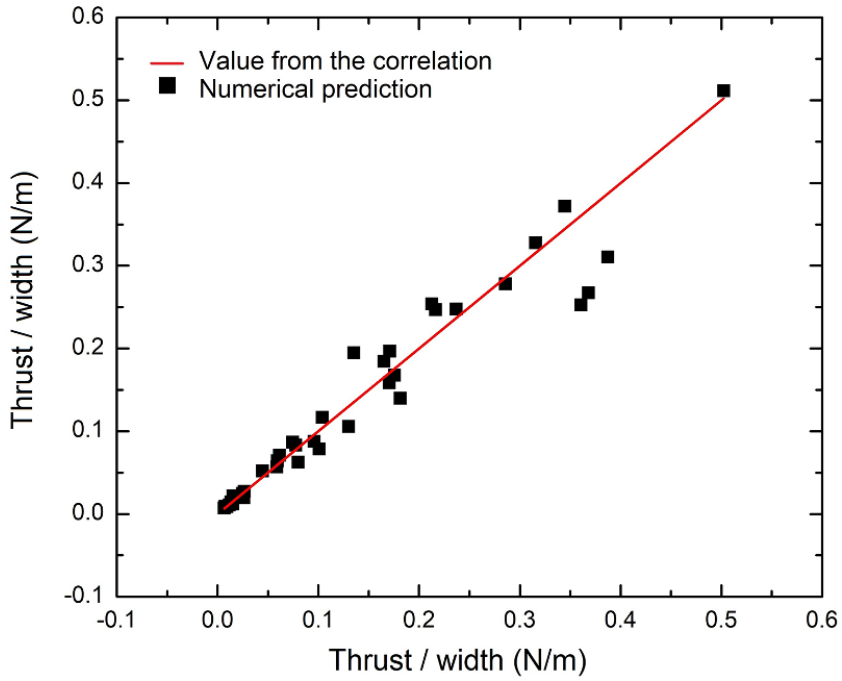

Figure 4.18: Comparison of the predictions of the proposed correlation with the data points obtained from the numerical analysis

4.6 Micronozzle in a cluster arrangement

From the above sections how a single micronozzle is behaving in different operating conditions has been identified. The thrust produced by the micronozzles is in micro Newtons, so to get the desired thrust level, micronozzles need to be arranged in the cluster. While in the cluster arrangement, the plume interaction of the nozzles will take place and it may affect the performance of individual micronozzles. So a number of numerical simulations have been conducted with varying nozzle pitches ranging from 100μm; 300 μm; 500 μm and 1000 μm. To study the thermal effect on the plume flow, two wall temperature has been selected as 300K and 1000K. The variation of the Mach number, thrust, and I_{sp} was plotted and analyzed in the following sections. The computational domain used for the current numerical study is depicted in Figure 4.19 and the whole domain is simulated using a DSMC method. A total pressure of 1000 Pa is imposed at the nozzle inlet, while a back pressure of 1 Pa is maintained at the nozzle exit for all simulations.

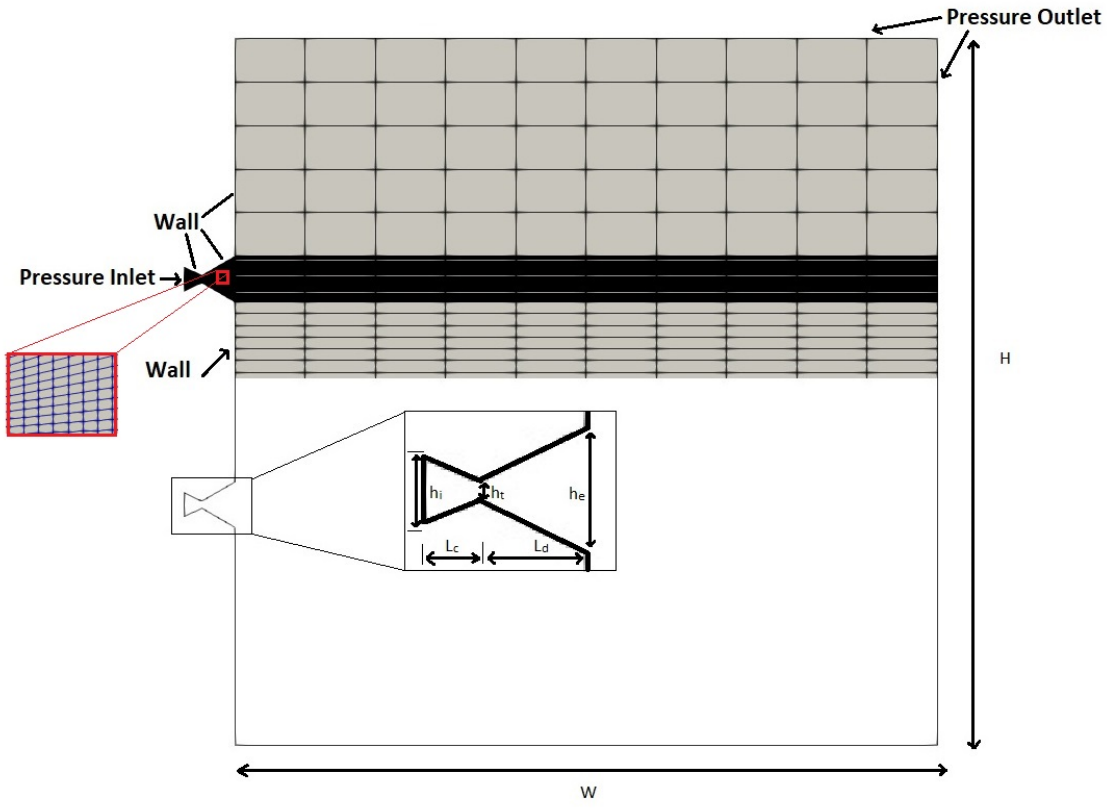

Figure 4.19: The geometry of the micronozzle in cluster arrangement for the DSMC study

4.6.1 Variation of maximum flow Mach number

The variation of maximum Mach number with nozzle pitch of the cluster for two different wall temperatures is depicted in fig.4.20. The maximum flow Mach number of the cluster configuration is found to increase with an increase in nozzle pitch for both wall temperatures studied. This is due to the merging of the viscous subsonic layer from the adjacent micronozzle in the cluster arrangement, which will stop the under-expanded plumes from the nozzles from growing. The micronozzle axis is parallel to these viscous layers, which prevents gas growth beyond the cluster.

Figure 4.20 additionally illustrates the variation in maximum Mach number with nozzle pitch for two distinct wall temperatures 300k and 1000K. The maximum Mach number of a nozzle with a higher wall temperature (1000K) also rises with pitch, albeit the values are observed to be lower than those of a nozzle with a lower wall temperature (300K). The decrease in Mach number with an increase in wall temperature is attributed to the heightened sonic velocity, aligning with expectations.

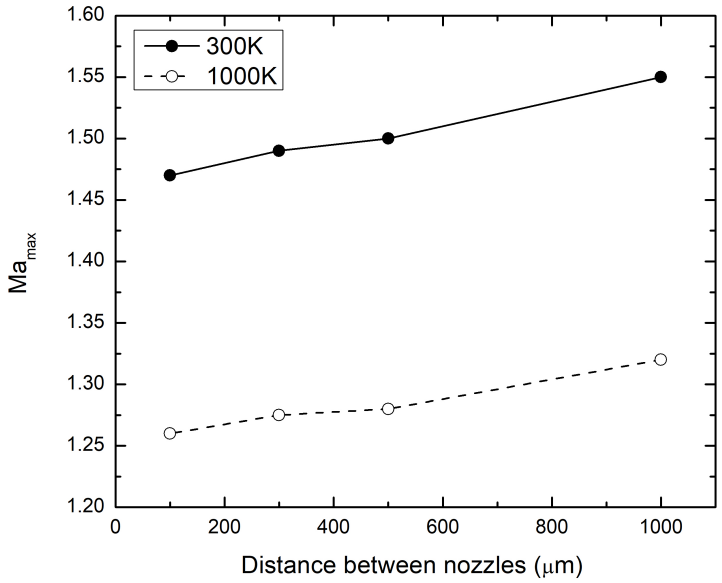

Figure 4.20: Variation of Maximum flow Mach number with the pitch at T_w =300 and 1000 K

4.6.2 Variation of Thrust and I_{sp}

The thrust and I_{sp} of the nozzles are calculated and plotted against the pitch of the cluster for the wall temperatures 300 and 1000K (fig. 4.21). The thrust produced by the 300K wall temperature nozzle is found to be higher than the 1000K Nozzle. The thrust was also found to be decreasing with an increase in nozzle separation initially up to 300μm and started to increase from there onwards with an increase in nozzle separation for both wall temperatures studied. This is a result of the trade-off between different factors that affect the thrust when the axis-to-axis distance is changed. The combined action of the momentum thrust component and the pressure thrust component produces thrust. Momentum thrust contributions will be greater at the smallest nozzle separations, but pressure thrust contributions to overall thrust are significantly reduced. It was discovered that as nozzle separation increased, the particular impulse of the nozzles grew a little bit. At 1000K wall temperature compared to 300K wall temperature, the specific impulse was found to be greater. The main cause of this is a considerable reduction in mass flow rate coupled with an increase in wall temperature.

The research findings indicated that there are distinct flow characteristics between subsonic and supersonic nozzles. The flow through the micronozzle is influenced by factors

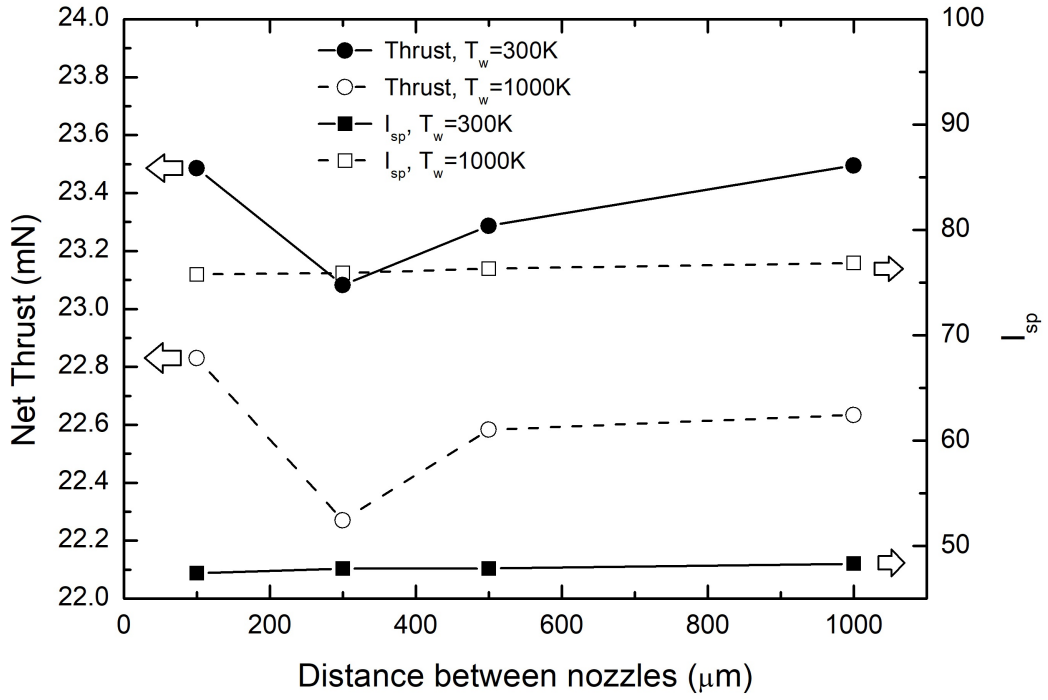

Figure 4.21: Variation of thrust and I_{sp} with the pitch at T_w=300K and 1000K

such as viscous loss and rarefaction effects. It's worth noting that the nozzle with the greatest divergence angle exhibited the highest loss and the lowest thrust, but this outcome might not apply to other micronozzle applications. Subsequent chapters will delve into a different application of the micronozzle, specifically, its use in aerodynamic mixture separation.

Chapter 5

Aerodynamic mixture separation using CD micro nozzles

This chapter discusses the use of converging-diverging micronozzles for species separation applications. It examines the effect of the size, divergent angle, and back pressure on species separation. The divergent shapes like linear, bell, and trumpet were compared to get optimum separation. The aid of carrier gas on species separation is also analysed.

This chapter is based on

1. M. K. Sukesan, S R Shine, Effect of back pressure and divergent section contours on aerodynamic mixture separation using convergent–divergent micronozzles, *AIP Advances*, 12(8), 085207, https://doi.org/10.1063/5.0097772

2. M. K. Sukesan,A. Kumar, S. R. Shine, Effect of Divergence Angle, Carrier Gas and Back Pressure on Species Separation using Convergent Divergent Micronozzle , *Proceedings of the 49th national and 9th international conference of Fluid Mechanics and Fluid Power (2022)*, IIT Roorkee.

5.1 Introduction

Research on flow characteristics of micronozzle is currently dominated by micro thruster applications, followed by its use for gas mixture separation. Uniformity in the flow structure to obtain the optimum thruster performance is the prime objective of the former, while the latter demands highly nonuniform species distribution of the flowing mixture. Further investigation is required to explore the suitability of aerodynamic mixture separation for continuous real-time applications.

One of the objectives of the present study has been to understand the binary separation characteristics of converging-diverging 2-D planar micronozzles under various conditions. Simulations are carried out with various divergent section shapes (linear, bell, and trumpet), throat heights (2-8μm),divergent angles (15-45°) and various back pressure (0-30kPa) conditions.The scaled version of Hao's nozzle was employed in species separation experiments for linear nozzles. A total of 54 simulations are conducted for the species separation study. The table 5.1 contains details of the computational studies conducted for the current chapter.

Table 5.1: Details of the computational studies conducted in the current chapter

Sl no.	Geometry Considered	Method Adopted	Geometry Parameters	No. of Simulations	Approximate Computational Hours
1	Planar Nozzle with linear, bell and trumpet divergent section for species separation	Full DSMC	h_t=2-8μm, L_d=4.75h_t - 15h_t, θ_d=15-45°	54	3888

The schematic of the linear nozzle configuration with dimensions non-dimensionalized with h_t is shown in Fig.5.1. The binary mixture consists of Argon (*Ar*) and Helium (*He*) (molecular masses of 39.95 and 4.00 u). Constant pressure (120kPa), temperature, and an equimolar mixture of *He* and *Ar* are considered at the inlet boundary. The outlet is assumed as the hard vacuum that prevents molecules' entry into the simulation domain. Various pressure exit conditions (0, 0.3, 3, and 30 kPa) are used to study the effect of back pressure. All Knudsen number mentioned in the study is based on throat height.

5.2 Flow field and streamlines

The mixture flow is driven by the pressure/temperature /concentration gradients, and therefore, variations in *He* and *Ar* velocities may be expected. Sabouri and Darbandi [9] have observed a considerable increase in the velocity of the lighter species along the centerline of the nozzle. The behavior of binary gas mixture flowing through a convergent-divergent

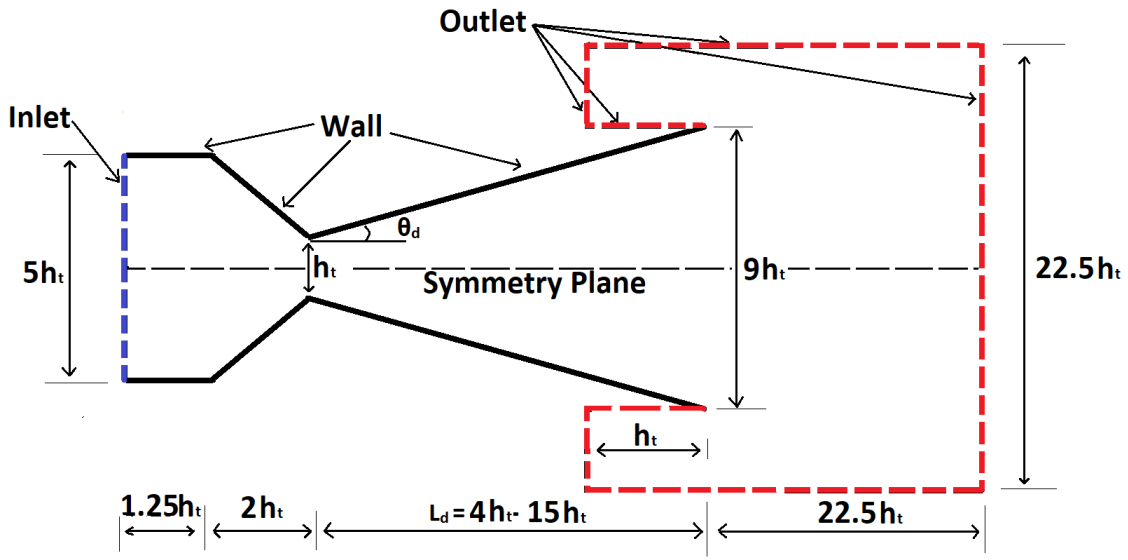

Figure 5.1: Micronozzle geometry details used for simulations

micronozzle of 2 and 8 μm is discussed in this section. The inlet pressure of the micronozzle has been 120 kPa. Flow is allowed to expand freely, and a fixed temperature of 300K is maintained at the wall. The molar fraction of *He* and *Ar* is maintained at 0.5 at the inlet of the nozzle. The Kn at the exit of the nozzle is observed as 0.209 and 0.0585 for the 2 and 8 μm h_t nozzles respectively Fig. 5.2b shows the mean velocities of *Ar* and *He* along the centre line. Towards the exit of the nozzle, the velocity difference between the lighter and heavier molecular species at the core region is increasing, and the difference is higher when Kn is high. It is observed that perpendicular to the flow, the difference is almost constant for the two nozzles. The shape of the convergent-divergent nozzle will produce curved streamlines and centrifugal pressure gradients in the outward direction. The curved streamlines generate for the 2 and 8 μm h_t nozzles are shown in Fig. 5.2a.

The species streamlines show a greater curvature for *He* than *Ar*. The disparity in molecular mass causes the difference in centrifugal forces and divergence of the streamlines. The effect is more severe in the 8 μm h_t nozzle. The pressure gradient is from the wall to the centreline at the exit, and the streamlines rotate outward. This effect is more for the bigger nozzle creating depletion of the heavier species near the wall.

One can expect higher heavier species concentration near the axis for the smaller nozzle whereas higher lighter species concentration on the peripheral regions of the bigger nozzle

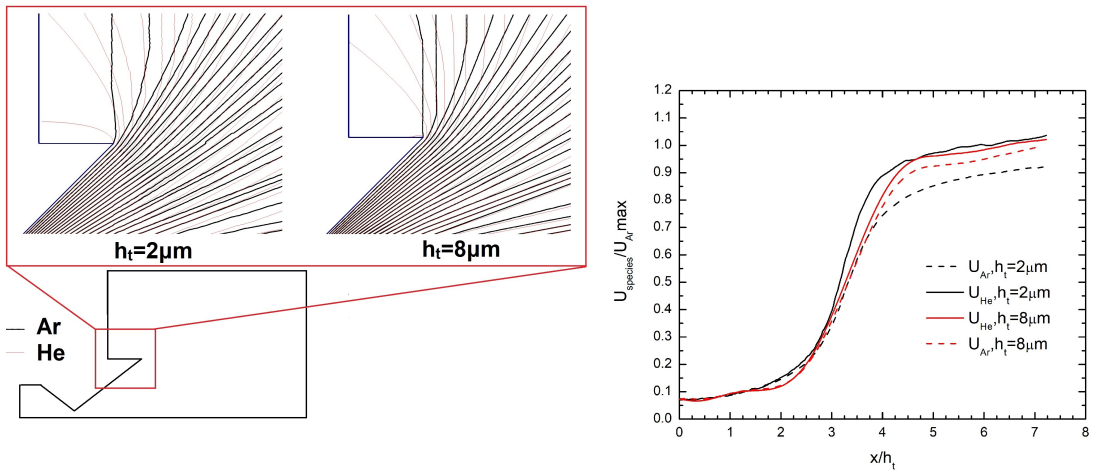

(a) streamlines **(b) Species mean velocities**

Figure 5.2: Streamlines and mean velocities of Helium and Argon and for the 2 and 8 μm h_t micronozzles

due to the difference in Kn. Consequently, the hypothetical surfaces shown in Fig.5.3 are selected to compare the species accumulation. The peripheral area ABCDEFG is used to compare the *He* accumulation and is shown in Fig.5.4. Higher *He* concentration is observed for the bigger nozzle along the line CDE. The smaller nozzle produced a higher *Ar* concentration along FG.

5.3 The species distribution

Fig. 5.5 shows the static mole fraction of *Ar* (heavier species) along the nozzle centerline. The static mole fraction (X) is defined based on the number density and is given by

$$X_{Ar} = \frac{n_{Ar}}{n_{He} + n_{Ar}} \tag{5.1}$$

The mole fraction increases from the inlet and reaches a peak downstream of the throat. Further increase of mole fraction is seen outside the nozzle exit. It is also noted that the concentration of heavier species along the centreline increases with the increase of Kn. It can be concluded that at higher exit Kn, a higher concentration of *Ar* is expected near the axis, whereas the *He* concentration near the wall is higher when Kn is lower. This is more evident from Fig. 5.6 and 5.7, which shows the stagnation mole fraction contour of *He*, Mach contour, and streamlines for the nozzles. The stagnation mole fraction (X_{st}) is

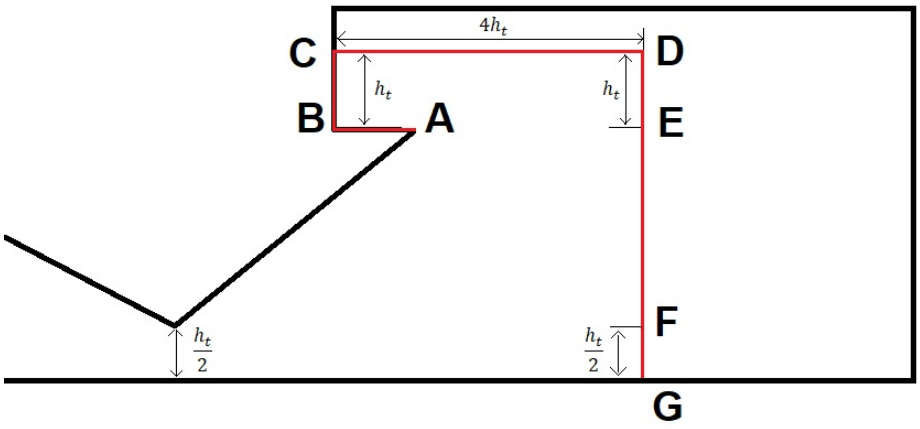

Figure 5.3: Sampling area for comparing species separation efficiency

defined based on the number density and velocity magnitude and is given by

$$X_{st-Ar} = \frac{n_{Ar}u_{Ar}}{n_{He}u_{He} + n_{Ar}u_{Ar}} \tag{5.2}$$

A thicker region of higher *He* concentration can be noticed for the 8μm nozzle divergent section. The static mole fractions of *He* in the vertical plane at the three axial locations downstream of the throat are shown in Fig. 5.8 for the 2 and 8 μm nozzles. The L1, L2, and L3 locations are selected downstream of the throat at a distance of h_t, $2h_t$, and $3h_t$, respectively. The non-dimensional parameter ($\psi = h_{max}/h_t$) is used to specify the axial location. A steep increase in the *He* mole fraction is observed for the nozzles adjacent to the throat near the wall. The helium concentration is higher throughout the wall, with the 8μm nozzle showing a significantly large value (around 16% increase). At the exit of the nozzle, the variation is almost linear for the 8μm nozzles, with a higher drop near the wall. The data in these sections are mainly provided for information purposes. The direct result is that the separation effect primarily depends on exit Kn created by the different nozzle sizes.

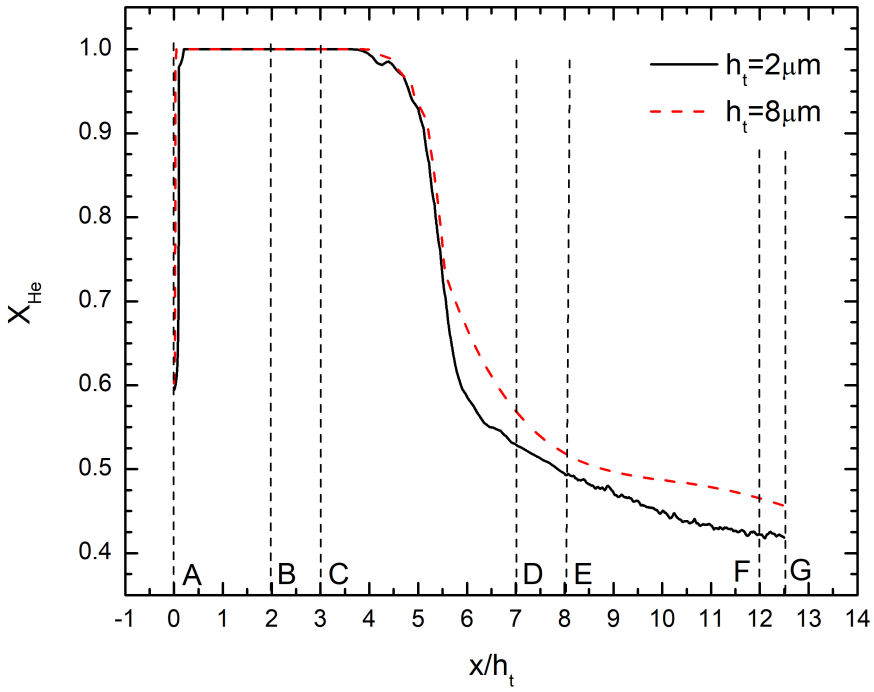

Figure 5.4: *He* molar fraction along the line ABCDEFG

5.4 Effect of divergence angle

The effect of divergence angle for a constant expansion ratio is studied with different divergence angles 15, 30, and 45° for micronozzle having h_t= 2μm. The expansion ratio is defined as the ratio of outlet to throat width. The length of the divergent section has been varied to maintain a constant expansion ratio. Inlet pressure of 120 kPa and hard vacuum at exit is maintained for all simulations.

Fig.5.9 shows the centerline mole fraction of *Ar* for the three cases. The highest mole fraction is observed for the higher divergence angle. The peak value shifted more downstream of the throat as the divergence angle increased. No significant differences are observed in the convergent part of the micronozzle. Considerable enhancement in *Ar* mole fraction is noticed for the 45° towards the exit. Since the expansion ratio is kept constant, the length of the divergent section varies for the three cases. The higher length of the 15° nozzle promotes more velocity slip and separation towards the exit. For the 45° divergent

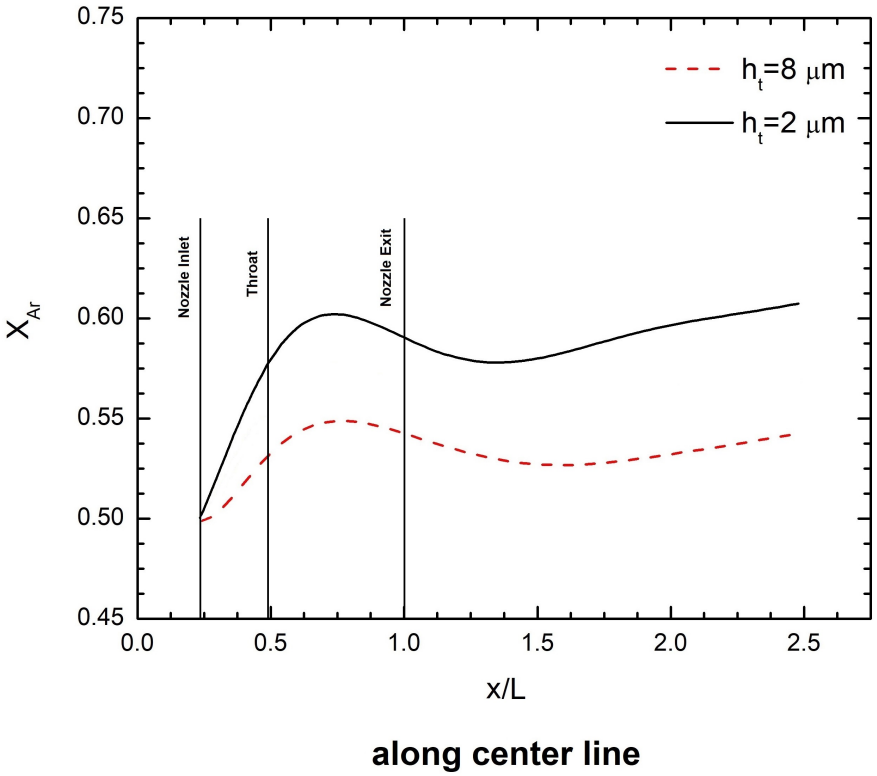

Figure 5.5: Variations of static Argon mole fraction along the centerline for various micronozzles

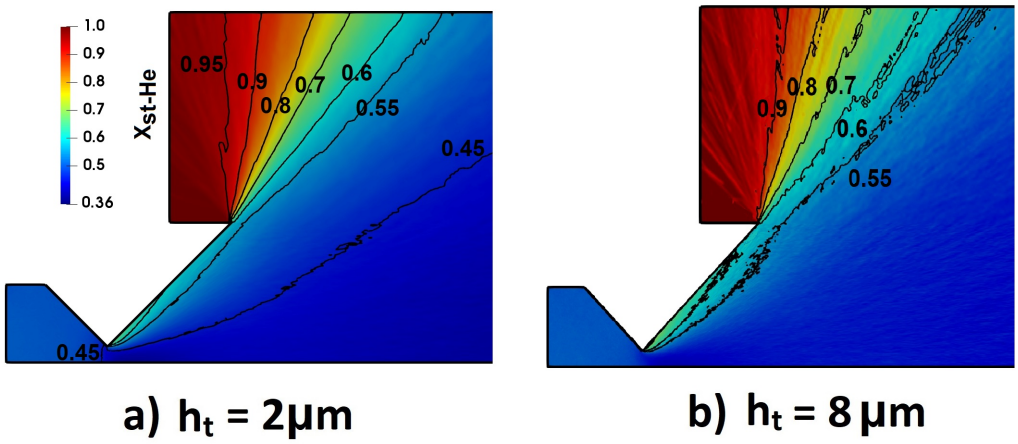

Figure 5.6: *He* stagnation mole fraction for the a) 2 and b) 8 μm h_t micronozzles

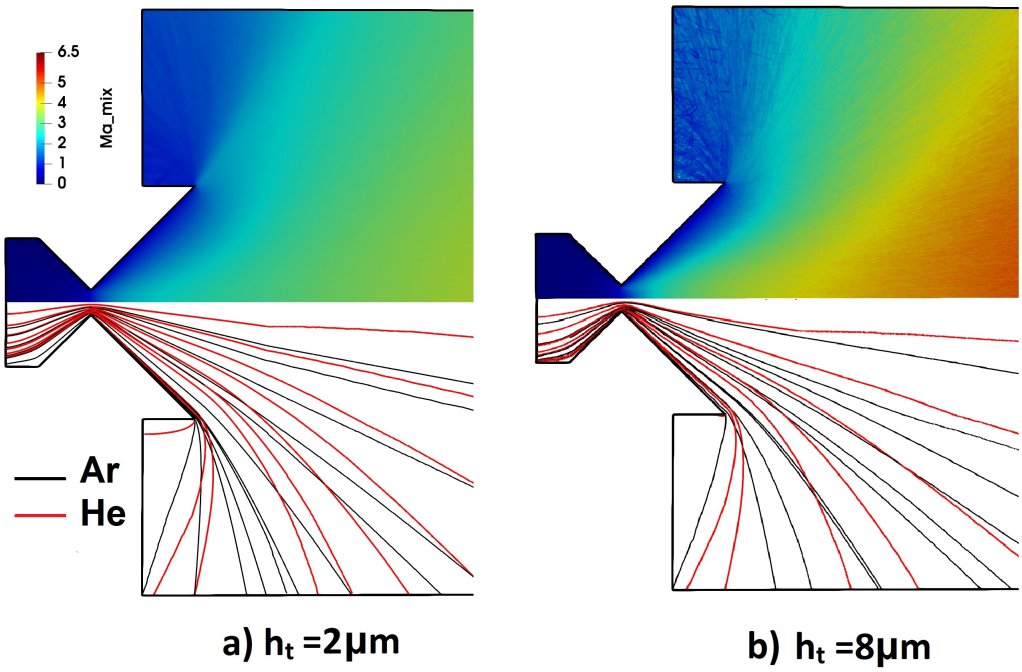

Figure 5.7: Mach number contour and streamlines for the a) 2 and b) 8μm h_t micronozzles

angle, wall deflection is more, resulting in higher lateral separation effects. The curvature of the streamlines is higher; the heavier molecules cannot bend so easily and therefore remains in the axis region. The bending of the He streamlines was found to be higher compared to Ar and the deviation is more visible at the outlet of the micronozzle. The highest bending of the streamlines in the 45° nozzle creates a higher pressure gradient towards the center of the nozzle and as a result, 45° nozzle shows the highest Ar concentration.

5.4.1 Effect of divergent section contours

Most of the past research involving the aerodynamic separation process using micronozzles has considered conical nozzles due to their simplicity and ease of manufacturing. The species separation performance of various micronozzles with a divergent section having linear, bell, and trumpet shaped contours are analyzed. The throat height for all micronozzles is kept as h_t= 2 μm. The convergent section dimensions, divergent section length, throat height, and expansion ratio are kept the same for all the nozzles studied. Bell nozzle contour has been created according to the method of characteristics (MOC) based on Rao's approximation [197]. By altering the lip angle θ_e, two bell nozzles with distinct diverging parabolic curves are created, as shown in Fig. 5.10a. The parabolic profile starts imme-

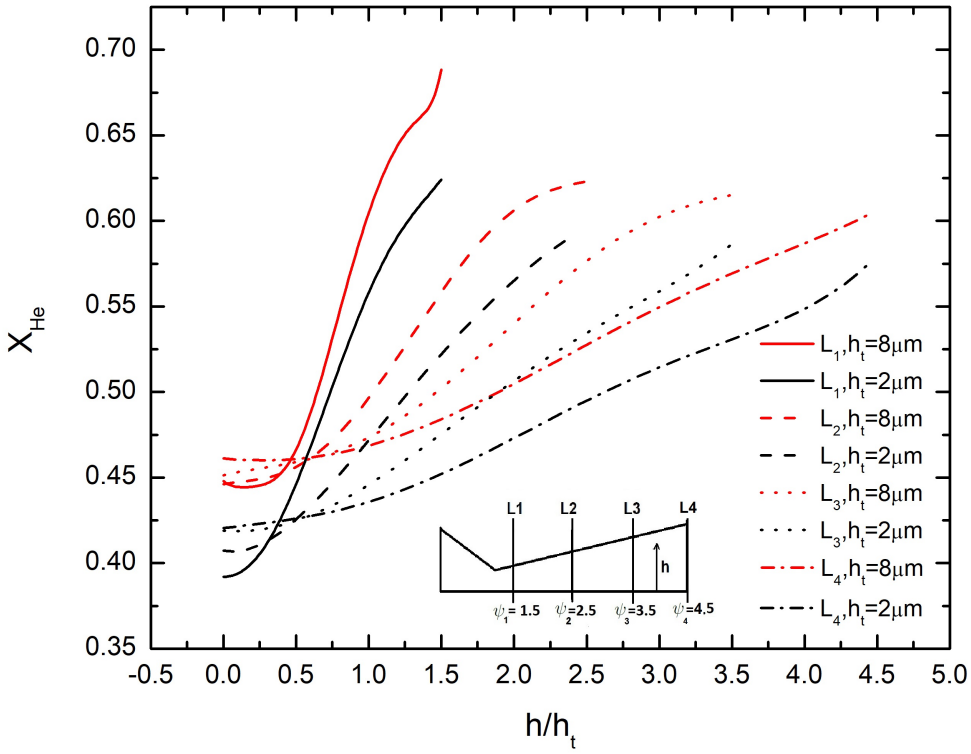

Figure 5.8: *He* mole fraction in the vertical plane at the three axial locations and at the nozzle exit of various micronozzles

diately after the initial expansion angle θ_n, and it is extended up to the exit of the nozzle, where it will meet the lip angle θ_e. The bell nozzles are designed with Autodesk Fusion 360 software [198] and meshed with OpenFOAM's block mesh tool [199]. The arc (c-d) near the convergent section has a radius of 0.75 h_t. The arc (d-e), which connects the throat to the parabolic extender, has a radius of 0.191 h_t. The parabolic curve-1 and curve-2 (e-f) are created with a lip angle of zero and 8 degrees, respectively. For both the bell nozzles investigated, the divergent angle θ_n was set to 30 degrees. The convergent portions (b-c) of both the bell nozzles are made smooth, and the divergent length L_d has the same length of 15° linear nozzle. For the trumpet nozzle, the shape is created with an arc of radius 60 and 120 μm immediately after the throat. The radius of the curve is chosen to be 30 or 60 times the throat height. OpenFOAM's block mesh tool[199] is used to generate and mesh the geometry. Fig.5.10b depicts the trumpet curves. These curves which connect the throat to the exit are selected to study the effect of divergent trumpet curvature on separation.

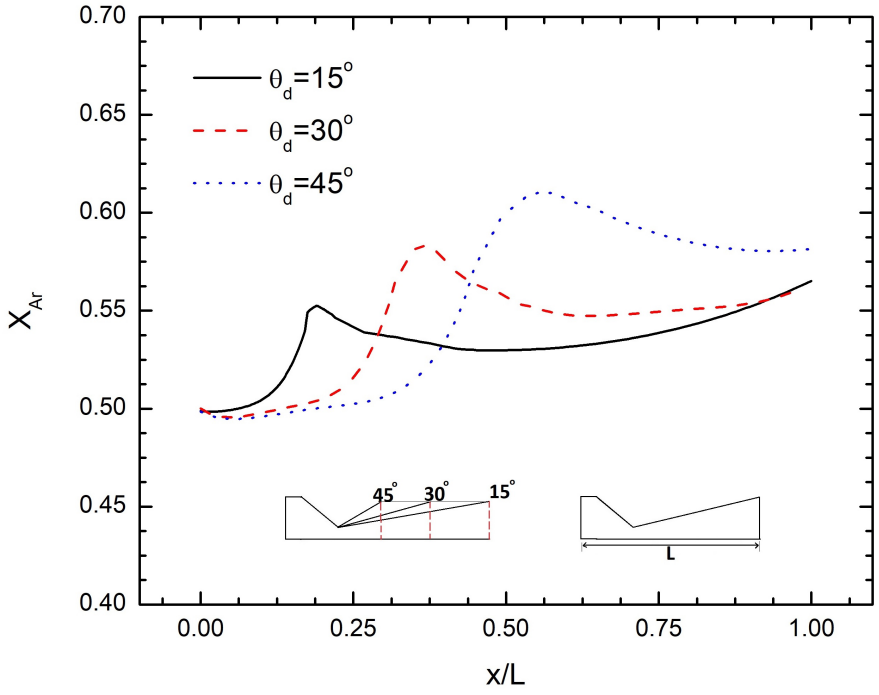

Figure 5.9: Ar mole fraction along the centreline for micronozzles having different divergence angles 15, 30, and 45°

Simulations are conducted with a sharp and curved throat region of bell nozzles to check whether the shape influences the central Argon mole fraction. Fig.5.11 shows the *Ar* mole fraction along the centreline for both cases. *Ar* concentration is the same everywhere except the immediate downstream of the throat, where the smoothed convergent portion has the highest mole fraction. The shape effect is negligible in all other locations. Fig. 5.12 shows the static mole fraction of *Ar* along the nozzle centerline and across the exit for the three cases, linear, bell nozzle-1, and trumpet-1. The trumpet nozzle shows a higher *Ar* centerline concentration. *Ar* mole fraction variation in the vertical plane at the exit is also different for various shapes. The flow alignment capability of the bell nozzle is demonstrated in Fig.5.13, which shows the transverse Y velocity component for the different shapes under exit vacuum conditions. The trumpet and linear nozzle show significant Y-velocity at the exit plane.

The center line velocities of *Ar* and *He* for the bell and trumpet nozzles are compared in

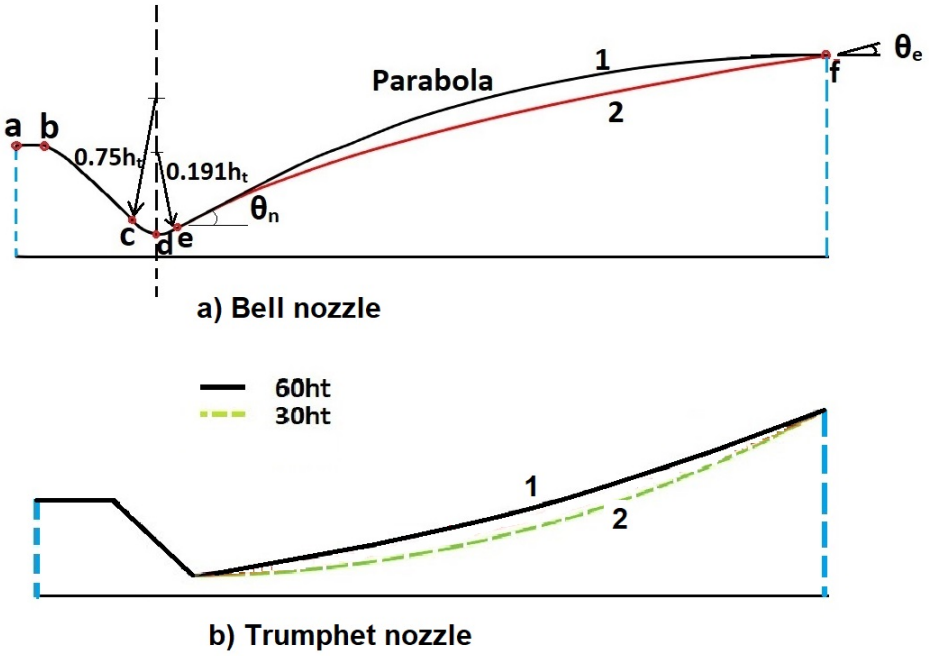

Figure 5.10: Micronozzle a) Bell and b) Trumpet shapes considered for separation studies

Fig. 5.14. The velocity slip is maximum downstream of the throat but decreases towards the exit. A higher lip angle of the bell creates a higher velocity slip, though the exit velocities are decreased compared to the trumpet. For the trumpet nozzle, slip velocity gradually increases along the axis. The stagnation mole fraction of *He* along the axis for the various cases are analyzed in Fig. 5.15. The divergent section of the trumpet shapes shows the highest separation compared to the bell and linear nozzles, though the advantage decreases at the exit downstream. The separation effect increases almost linearly along the axis.

Fig.5.16 shows the stagnation mole fraction of *He* and the streamlines of the species for the trumpet and bell nozzles. More outward bending of the streamlines is observed for the trumpet nozzle, facilitating higher lateral separation. Fig.5.17 shows the Mach number and pressure distribution for various cases. This is presented to understand better the gas behavior in these systems and for information purposes.

The Mach number contours of the three cases illustrate a significant subsonic layer present in the divergent section of the bell nozzle, causing a reduction in the average exit

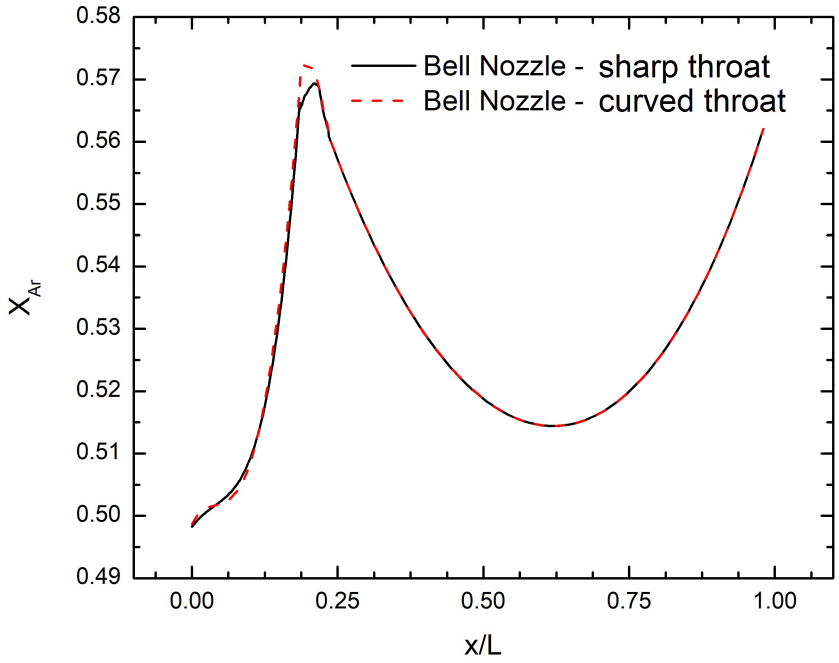

Figure 5.11: Ar mole fraction along the centreline for the bell nozzle with sharp and curved throat section

Mach number. As the velocities are lower, the slip velocities are also lower, driving lower separation performance. The growth of the subsonic layer is less when the lip angle is high, which causes an increase in average exit velocity. This caused an increase in velocity slip and increased separation performance.

5.5 Effect of back pressure

The effect of back pressure is studied for the 2 μm h_t micronozzle by varying the exit back pressure from 30 kPa to 0 kPa. Fig.5.18 shows Mach number contours and mean streamlines for various back pressures. It is observed that the exit pressure and the thick subsonic layer contribute to the flow behavior significantly at higher back pressures. At the high back pressure of 30 kPa, the divergent section is dominated by the subsonic flow. The flow reaches the highest Mach number downstream of the throat and decelerates in the divergent area. As the subsonic layer mostly dominates the divergent part, there might be a negligible effect of the divergent shape on flow features. Since the subsonic region spreads up to the

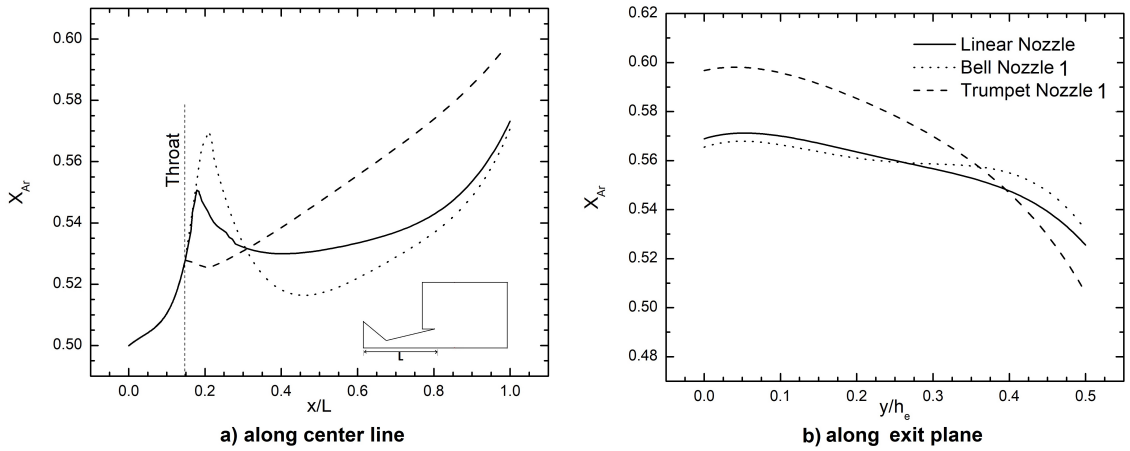

Figure 5.12: *Ar* mole fraction for bell, trumpet, and linear nozzles (h_t= 2 μm for all cases) for the same operating conditions (a) along the centreline, (b) at the exit vertical plane

axis, the core isentropic flow has degenerated. The back pressure and the ambient flow field might communicate to the upstream in this case and causes the turning of the flow and deflection of exit momentum in the transverse direction. When the exit pressure decreases, the flow continuously accelerates, and the divergent section shape could substantially affect flow behavior. Fig.5.19 shows the stagnation mole fraction variation along the line C-D-G at the exit of the nozzle for all four cases investigated. For vacuum exit conditions, the bending of the streamline at the nozzle tip will create a pressure gradient towards the center of the nozzle, which produces a higher concentration of heavier species (*Ar*) at the center. From Fig. 5.18, it is visible that the bending is more at the lip of the nozzle for higher back pressure conditions, which will create a pressure gradient away from the wall towards the exit. This is more evident in Fig. 5.19, where the *He* concentration decreases away from the centreline, but the rate of decrease is higher under vacuum conditions. This creates a higher *Ar* mole fraction at the nozzle's exit near the wall for higher back pressure cases. *He* concentration increases with height for all cases though the rate of increase is different.

Fig. 5.20 shows the pressure contours and stagnation mole fraction of *He* under different back pressure conditions. High stagnation mole fraction can be noticed at very low back pressures. This is created by increased flow turning and higher flow acceleration. Variation of Kn, and mean free path of the mixture, is shown in Fig. 5.21. Kn is found to be increasing with decreasing exit pressure, and flow enters the free molecular regime. The high Kn zone is located behind the plume and above the nozzle exit plane.

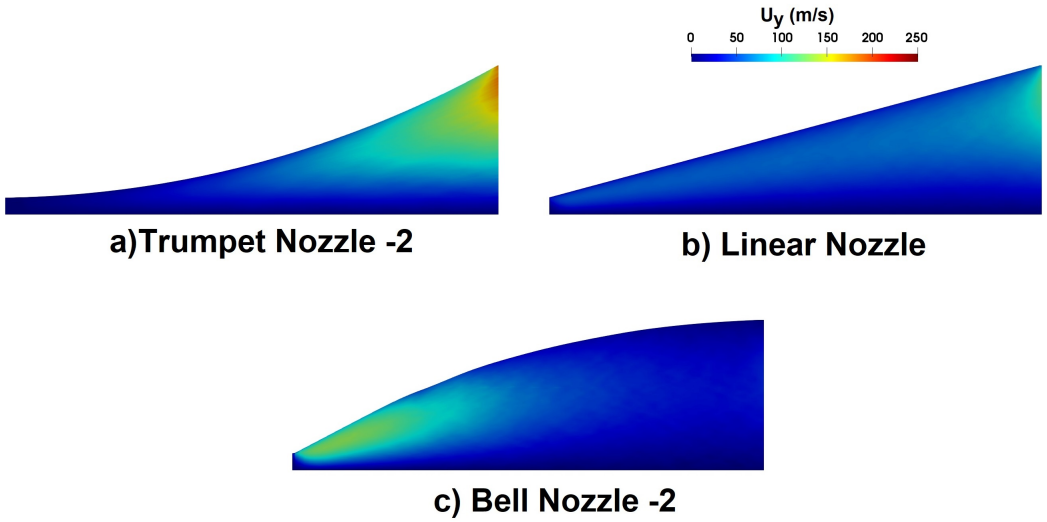

Figure 5.13: Transverse velocity components u_y in the linear, trumpet, and bell nozzle at vacuum exit conditions

5.6 Effect of carrier gas

To study the effect of carrier gas on species separation, a third gas is introduced along with Helium and Argon. Nitrogen is selected as the carrier gas as it has a molar mass between *He* and *Ar*. Different simulations are conducted with varying percentages of carrier gas, such as 0%, 33%, 70%, and 90%. Inlet pressure of 120 kPa and hard vacuum at exit is maintained for all simulations. The normalized Argon mole fraction on a vertical plane at a distance of $2h_t$ from the nozzle exit is plotted and is shown in Fig.5.22.The introduction of carrier gas has decreased the species separation effect at the nozzle exit. As the percentage of N_2 increases, the species separation is reduced at the exit of the domain.

Simulations are conducted with a heavier carrier gas such as Krypton (*Kr*), and the results are shown in Fig.5.23.The selection of N_2 and *Kr* as carrier gases are based on specific characteristics, particularly their molecular weights in comparison to *Ar* and *He*. Firstly, with regard to N_2, its molecular weight falls between that of *Ar* and *He*. This choice is likely made for specific applications where a moderate molecular weight is advantageous. On the other hand, *Kr* is selected because it has a molecular weight higher than both *Ar* and *He*. This can be advantageous in scenarios where a carrier gas with a higher molecular weight is required. The molecular weight of a gas can impact its ability to carry substances through a

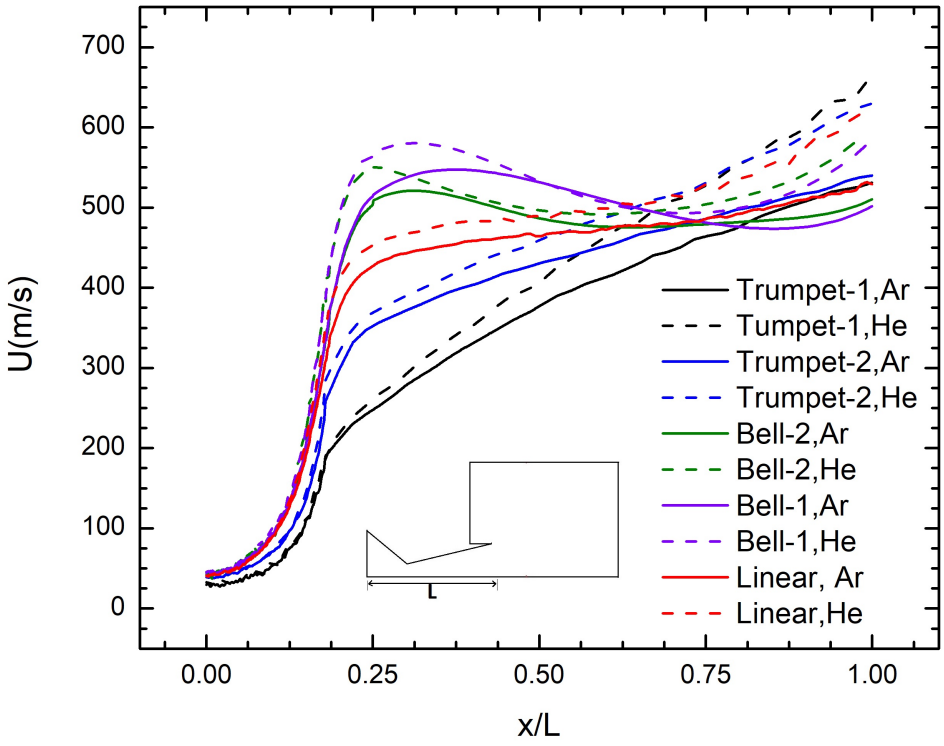

Figure 5.14: Center line velocities of Ar and He for the bell and trumpet nozzles studied

system, affecting parameters such as diffusion and separation efficiency. As the carrier gas becomes heavier, the species separation is suppressed. Krypton is almost heavier by two times Ar and 20 times He. Adding a heavier component reduces the lateral separation effect due to the low turning of streamlines. Lower species streamline divergence is noticed with heavier carrier gas. The slip velocity is highest when the difference in molecular weight is highest. There is higher bending for the lighter gas (He) and the least for the heavier gas (Kr). N_2 and Ar almost traced the same path because of the slight mass difference.

The investigation highlights that the bending of streamlines is a primary factor responsible for species separation. Consequently, a study has been carried out on a curved micronozzle, and the results of this study will be examined in the following chapter.

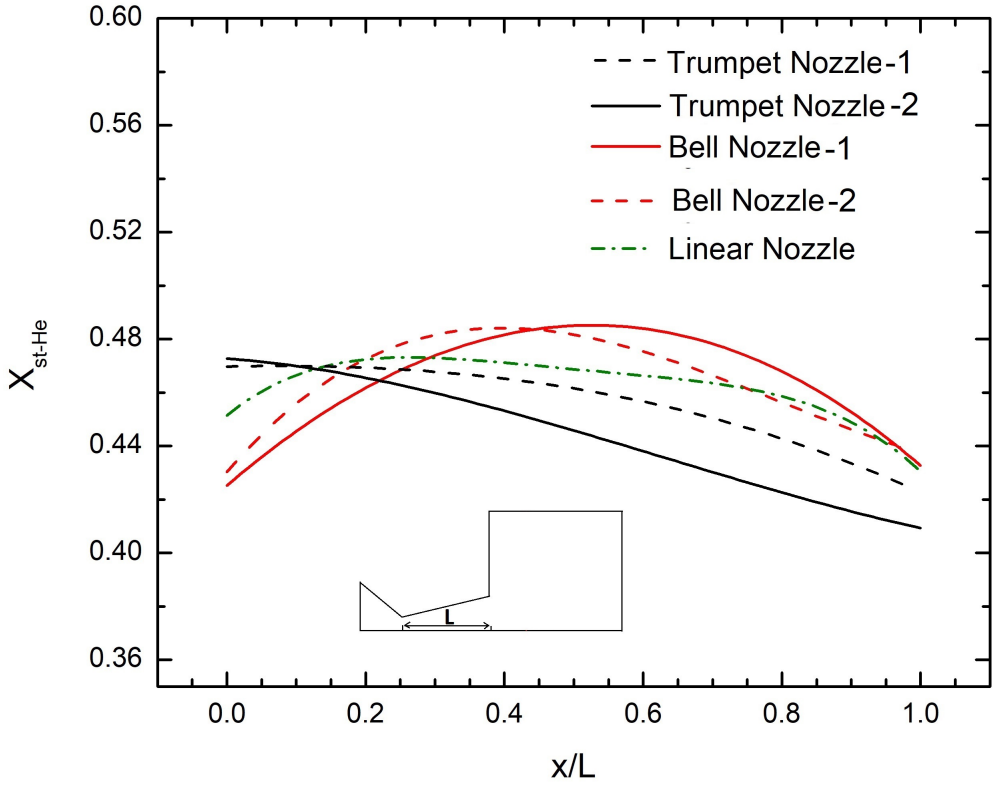

Figure 5.15: Stagnation mole fraction of *He* along the axis for the bell, trumpet, and linear nozzles studied

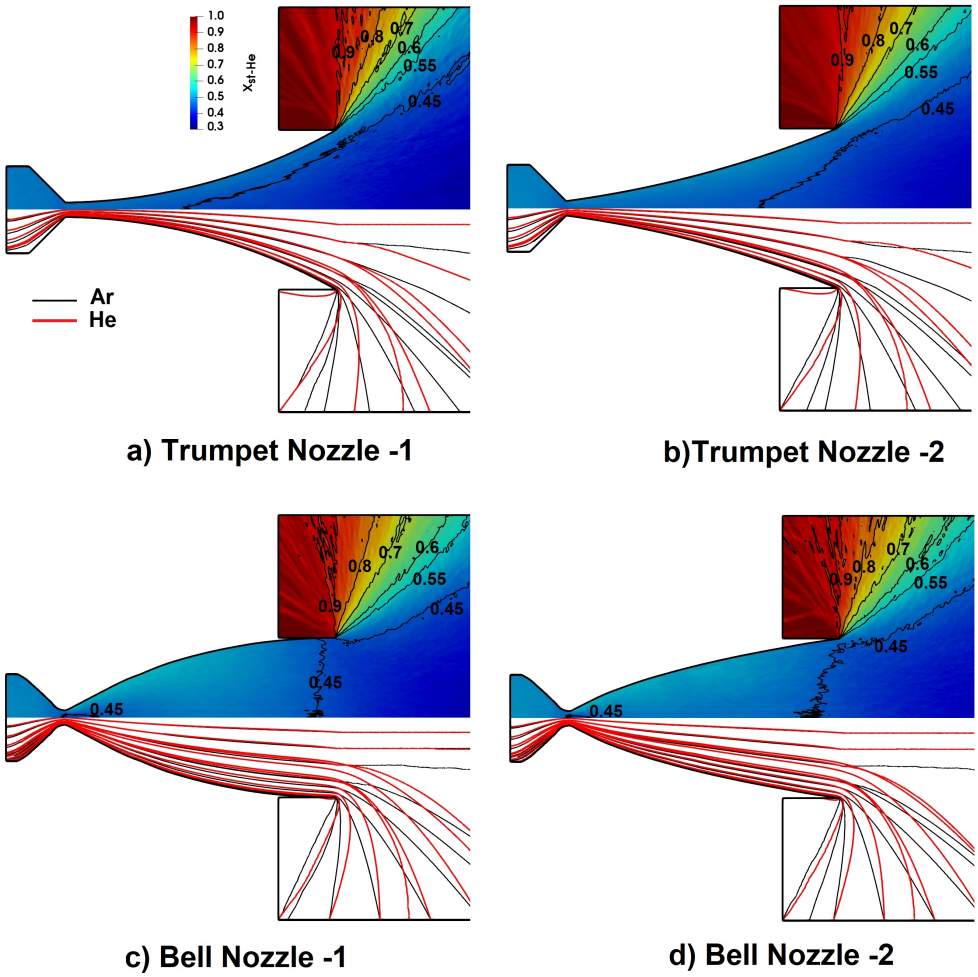

Figure 5.16: Stagnation mole fraction of *He* and the streamlines of the species for the trumpet and bell nozzles having 2 μm h_t

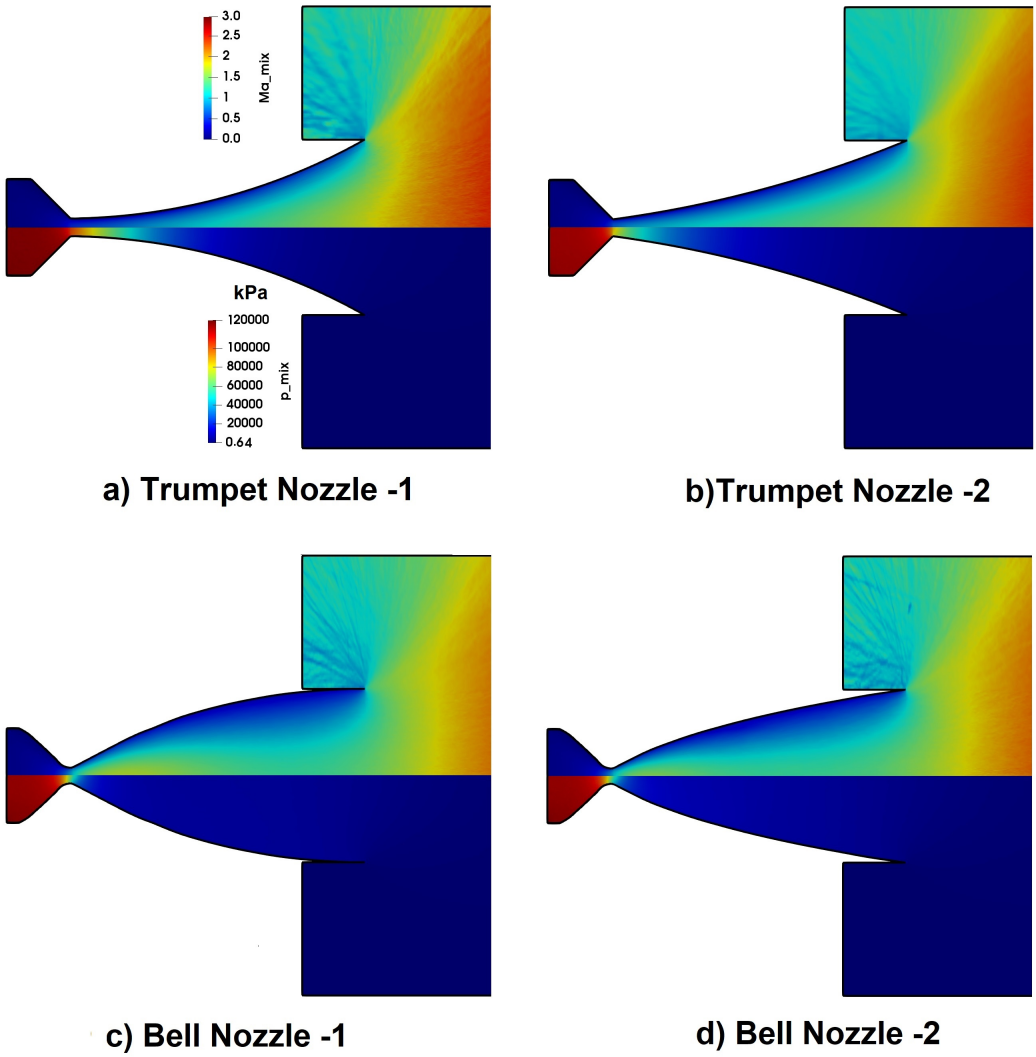

Figure 5.17: Mach number and pressure distribution for the trumpet and bell nozzles having 2 μm h_t

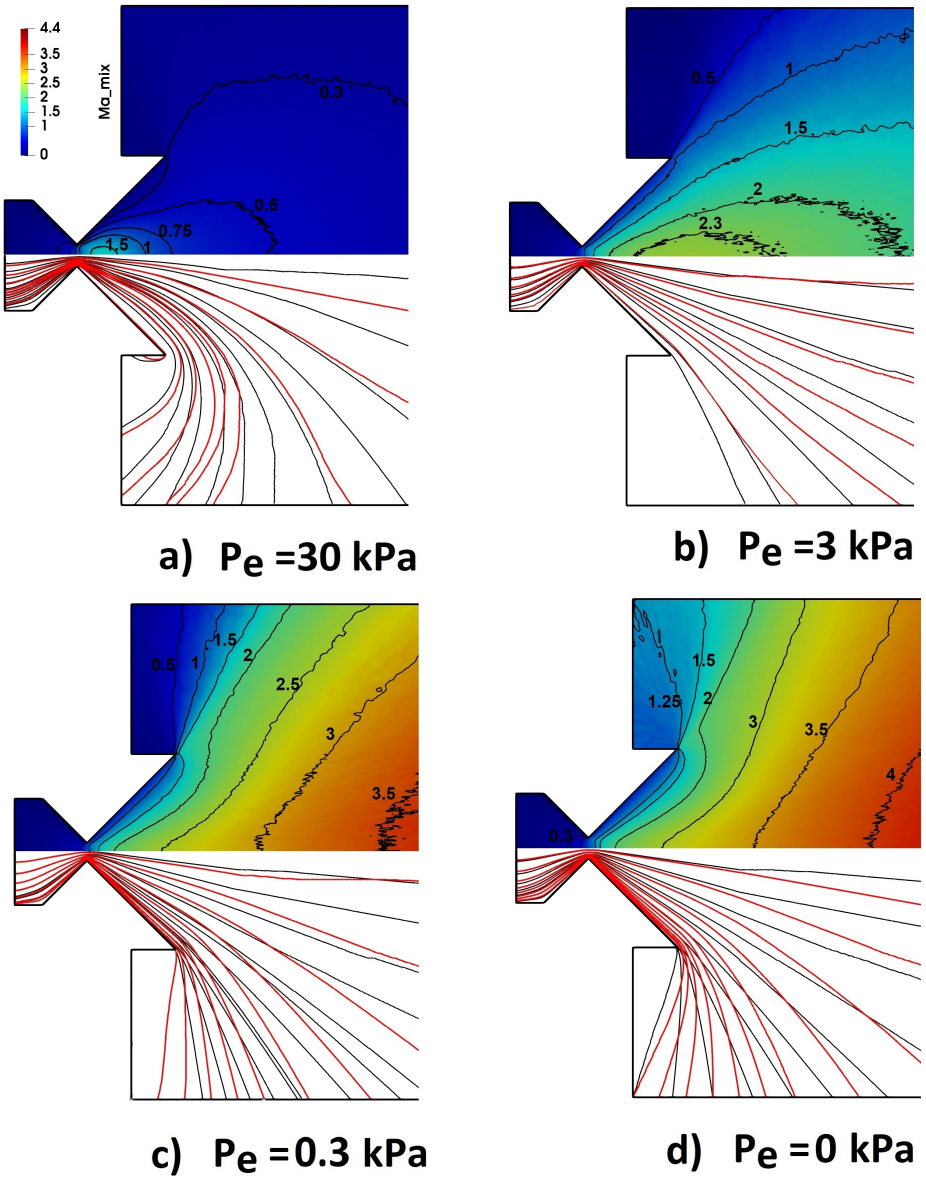

Figure 5.18: Mach number contours and streamlines for the 2μm h_t micronozzle under various back pressures a) 30, b) 3, c) 0.3 and d) 0 kPa

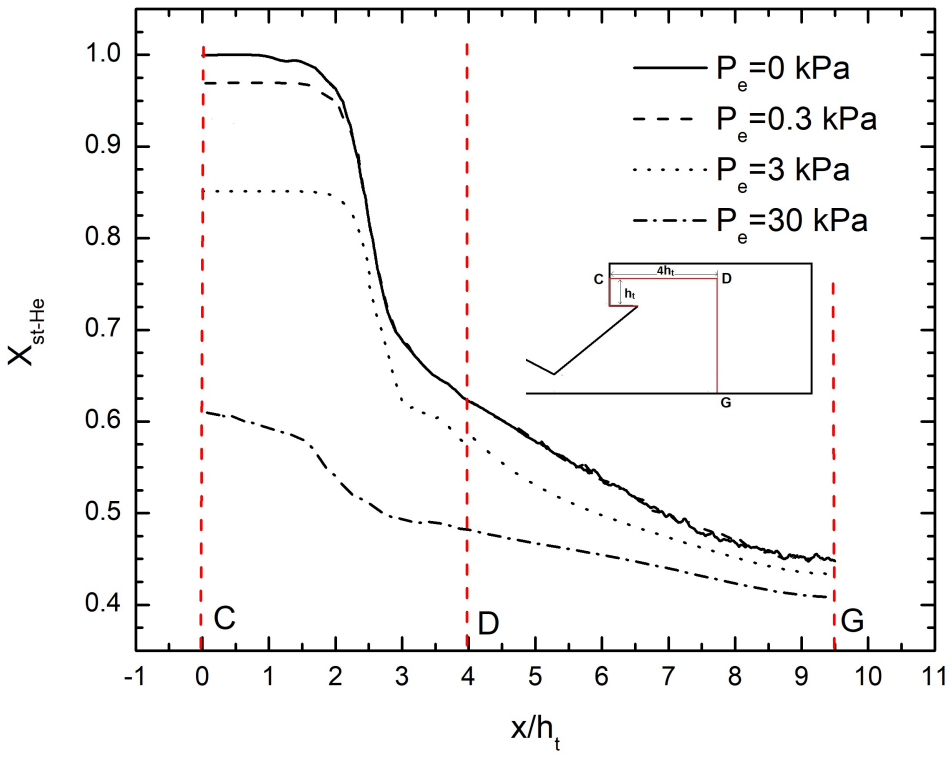

Figure 5.19: Stagnation mole fraction variation at the exit plane (CDG) at various back pressure conditions for 2 μm h_t micronozzle

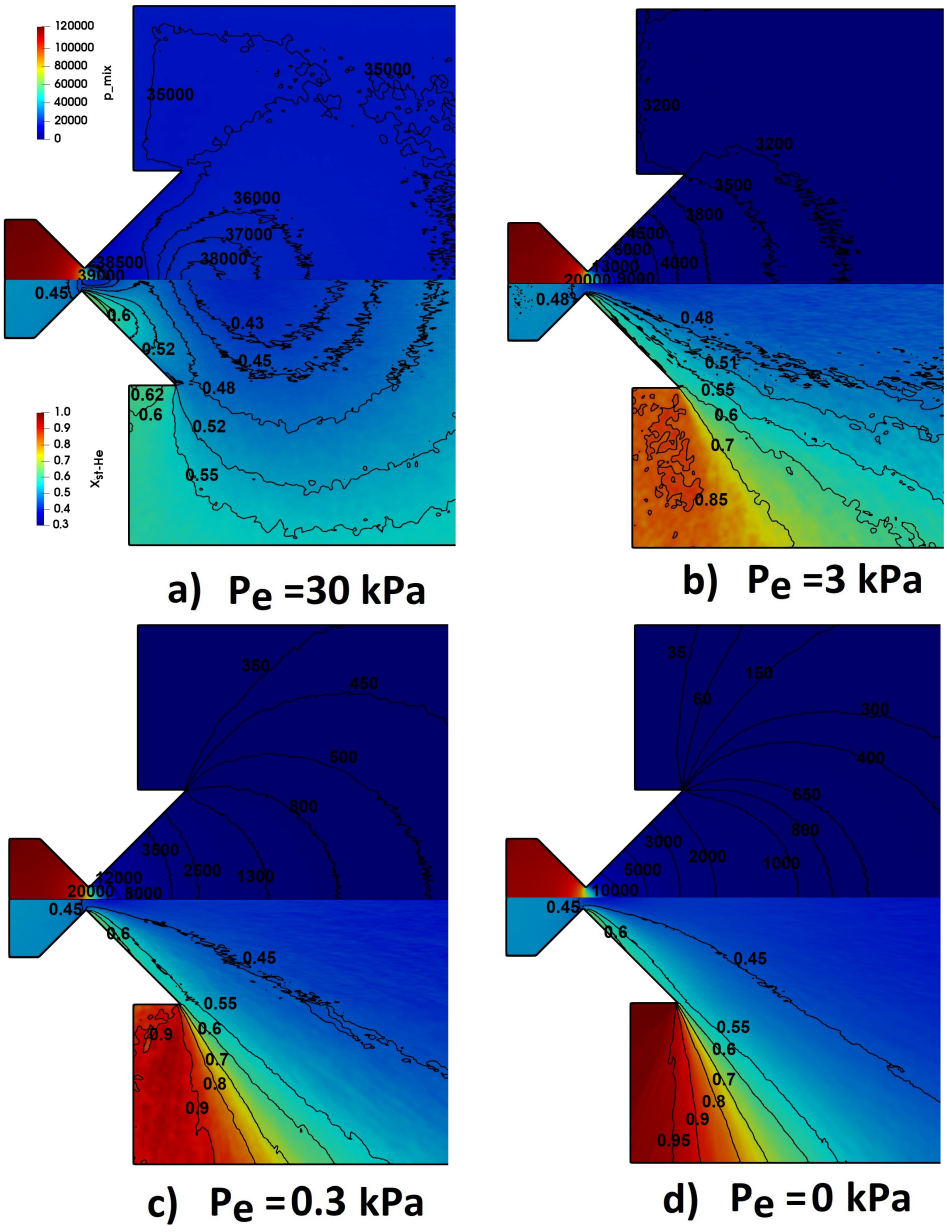

Figure 5.20: Pressure contours and stagnation mole fraction of He under different back pressure conditions for 2 μm h_t micronozzle

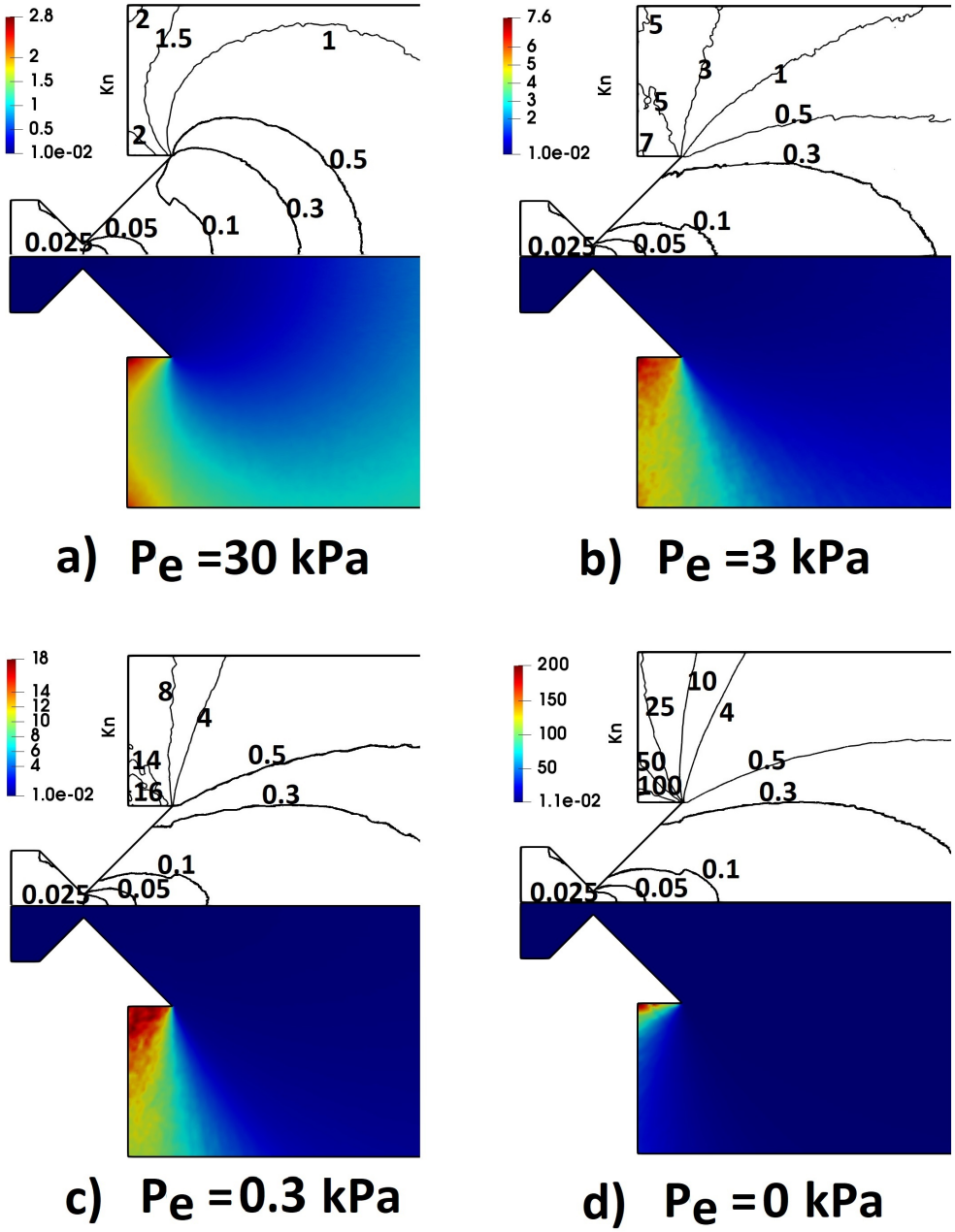

Figure 5.21: Kn contours at various back pressures for 2 μm h_t micronozzle

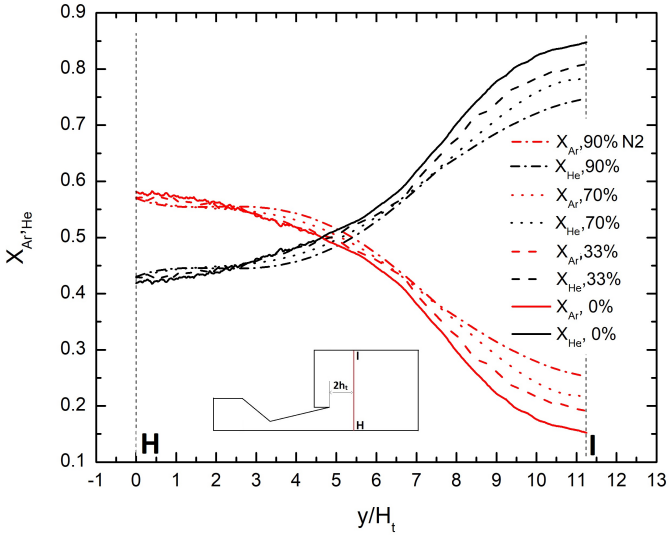

Figure 5.22: Micronozzle axis Argon and Helium mole fraction for the linear nozzle with N_2 as carrier gas

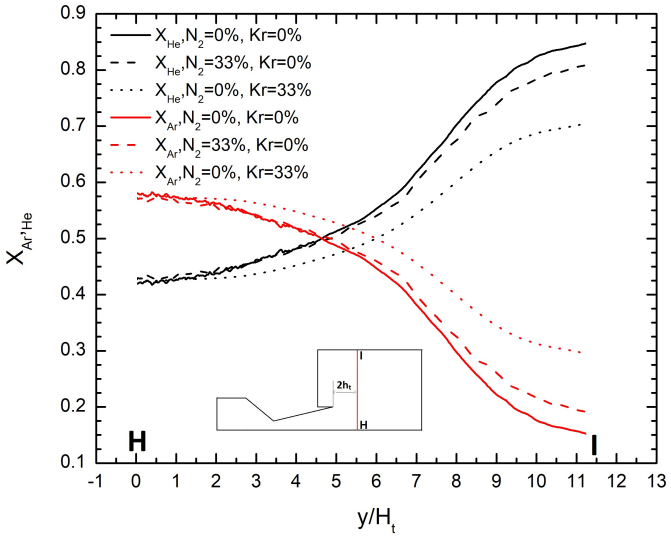

Figure 5.23: Micronozzle axis Argon and Helium mole fraction for the linear nozzle with *Kr* and N_2 as carrier gas

Chapter 6

Performance of curved micronozzle used for gas separation

This chapter presents the study focused on separating species using a curved nozzle with different radii of curvature, nozzle wall temperature, and various back pressures. The primary objective is to ascertain the most suitable nozzle design for efficient species separation achieved by comparing the results obtained from curved and linear-wall nozzles.

6.1 Introduction

A previous study conducted using linear nozzles has demonstrated that when the flow streamlines are curved, the discrepancy in molecular mass leads to the development of varying centrifugal forces, ultimately causing the streamlines to diverge. This phenomenon gives rise to the lateral separation effect, which becomes more pronounced as the curvature of the streamlines increases. Consequently, there is an enhanced concentration of higher-molecular-mass species in the peripheral regions. Therefore the study has been extended to the curved nozzle in order to analyze the effect of various operational and geometrical parameters on species separation. Flow through a curved geometry creates pressure gradients across the flow due to centrifugal forces and offers the possibility of separation. The current work numerically investigates the aerodynamic separation process associated with curved micronozzles operating under vacuum exit conditions.Curved nozzle dimensions and flow parameters were selected similar to Li's [182] earlier experimental research. Direct Simulation Monte Carlo method is used to simulate gas mixtures with various compositions of species. A total of 33 simulations were conducted and the effect of the curvature of the

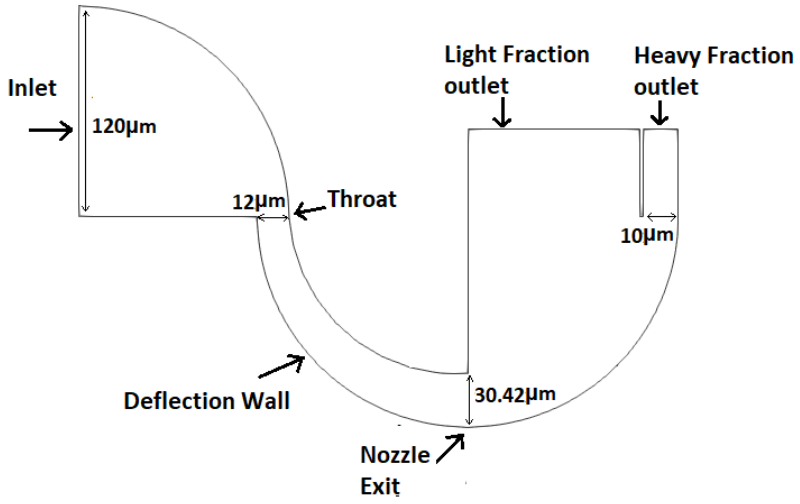

Figure 6.1: Geometry of the curved nozzle

geometry, differential wall heating, and back pressure effects are analyzed. The table 6.1 contains details of the computational resource used for the numerical studies conducted.

Table 6.1: Details of the computational studies conducted in the current chapter

Sl no.	Geometry Considered	Method Adopted	Geometry Parameters	No. of Simulations	Approximate Computational Hours
1	Curved nozzle for species separation	Full DSMC	h_t=12μm, R=100-140μm	33	2376

The studied geometry of the curved nozzle is depicted in Fig 6.1. A skimmer is provided at the exit of the domain to separate out the heavier species. A curved converging section has been used for better performance [182]. All the studies have been conducted with an inlet mixture temperature of 300K and exit vacuum conditions. At the inlet of the nozzle, an equal molar mixture of species with 100kPa pressure is introduced in all the studies except unless stated in the subsequent section.

6.2 Different Mixture combinations

Three different mixture combinations, $N_2 + SF_6$, $Ar + SF_6$, and $He + Ar$, have been used to study the effect of molecular mass ratio on species separation. The inlet conditions, species mass ratio, and diffusion coefficients for various cases are shown in table 6.2.

Table 6.2: Details of the species mixture studied

Mixture	Temperature (K)	Pressure (atm)	Mass Ratio	D_{ab}(x10^{-6}) (m^2/s)
$Ar + SF_6$	300	0.5	3.65	17.2
$N_2 + SF_6$	300	0.5	5.214	19.6
$He + Ar$	300	0.5	9.987	146

where binary mass diffusion coefficient (D_{ab}) can be calculated from the following equation [200]

$$D_{ab} = 0.00188T^{\frac{3}{2}}\sqrt{\frac{M_1 + M_2}{M_1 M_2}}\frac{1}{P\sigma_{ab}^2\Omega_D} \tag{6.1}$$

σ_{ab} is the characteristic length defined as

$$\sigma_{ab} = \frac{\sigma_a + \sigma_b}{2} \tag{6.2}$$

Ω_D is the collision integral for diffusion and can be calculated from

$$\Omega_D = \frac{1.06036}{(T^*)^{0.15610}} + \frac{0.19300}{exp(0.47635T^*)} + \frac{1.03587}{exp(1.52996T^*)} + \frac{1.76474}{exp(3.89411T^*)} \tag{6.3}$$

where T^* is

$$T^* = \frac{K_B T}{\epsilon_{ab}} \tag{6.4}$$

In all cases, an inlet heavier species concentration of 1% is maintained. Fig. 6.2 shows the mole fraction of heavier species along the bottom wall. The mole fraction is normalized with the inlet mole fraction and the length with the maximum length. The heavier species mole fraction is initially decreasing downstream of the throat. This is due to the effect of the initial converging section upstream of the throat and the circular converging area. The bending of the streamline creates the movement of the heavier species toward the upper wall. This effect persists a small distance downstream of the throat, and afterward, the trend is reversed. Fig. 6.3 shows the variation of heavier species mole fraction perpendic-

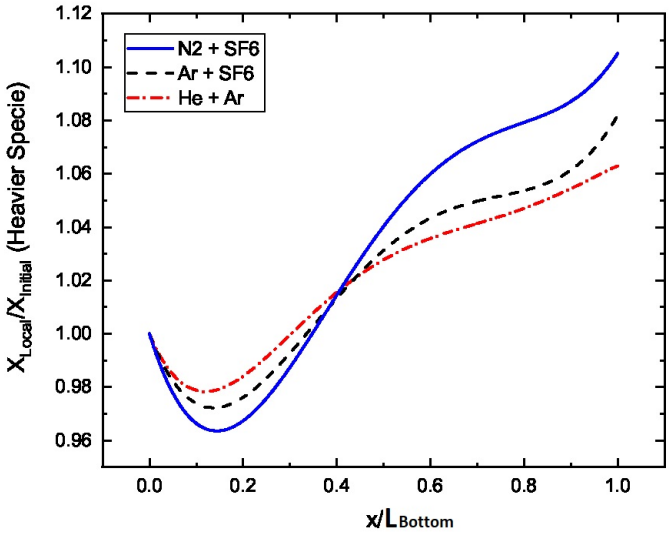

Figure 6.2: Normalized mole fraction of heavier species on the bottom wall for the $N_2 + SF_6$ mixture

ular to the axis at various locations of the curved nozzle for the $N_2 + SF_6$ mixture. A high concentration of species near the upper wall is noticed only adjacent to the throat. Previous studies also noticed the effect of curved streamlines and centrifugal forces on species separation[[9], [201]], and it is known as lateral separation. Towards the downstream of the throat, the curvature changes, and heavier species moves toward the bottom wall. $N_2 + SF_6$ mixture showed the highest separation at the exit. This can be explained with the help of two phenomena, one is due to the effect of mass ratio (lateral separation), and another is due to mass diffusion. The lateral separation effect will increase with the mass ratio. $He + Ar$ mixture has the highest mass ratio among all the mixtures studied, but due to the impact of diffusion, it has the least separation. The diffusion coefficient of the $He + Ar$ mixture is considerably higher than the others studied. The mass diffusion will work against the separation and will try to make the mixture composition uniform. $Ar + SF_6$ has the least mass ratio and diffusion coefficient. The trade-off between the lateral separation caused by mass ratio and the mass diffusion creates a higher separation at the exit for the $N_2 + SF_6$ mixture.

Previous research on micronozzles [[9], [201]] noted two distinct separation phenomena, lateral and streamwise separation. The slip velocity between the species created by the molecular weight differences facilitates the streamwise separation. As the mixture moves

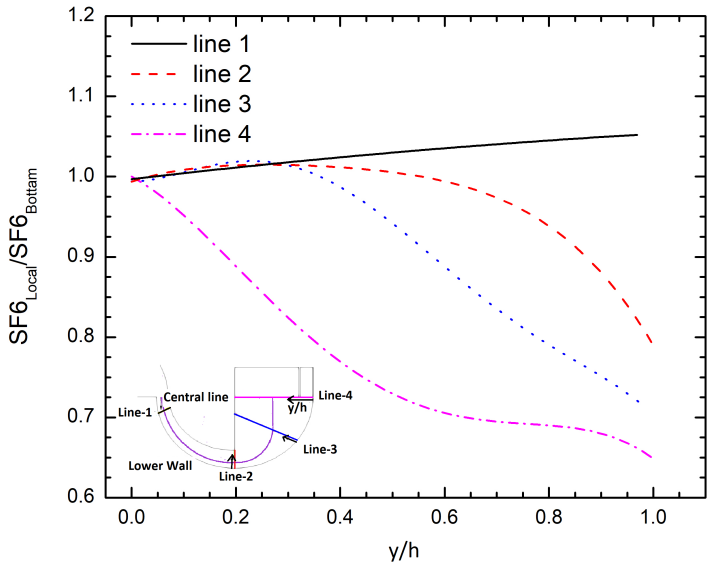

Figure 6.3: Normalized mole fraction of SF_6 along different lines perpendicular to the axis

through the domain, more separation will take place due to streamwise separation. Therefore bending of the streamline and velocity slip between the species facilitate the separation, and it is observed that the species with the highest mass will bend the least and will have the lowest molecular velocities. Fig. 6.4a and Fig. 6.4b shows the mole fraction contours of SF_6 and representative streamlines of different species at the exit of the curved nozzle. The heavier species SF_6 is found to be concentrated at the periphery of the domain, which can then be separated by a skimmer. Helium with the least molecular mass will bend the most, and the SF_6 will bend the least due to the highest molecular mass among the other species studied.

6.3 Different radius of curvature

In this section, the effect of the curvature of the nozzle is analyzed. An increased radius of curvature will force the streamline to bend more, enhancing the separation due to a higher centrifugal pressure gradient. The radius of the lower wall has been increased from $100\text{x}10^{-6}$ m to $140\text{x}10^{-6}$ m as shown in Fig. 6.5 to study the effect of the radius of curvature on species separation. $N_2 + SF_6$ mixture has been chosen for the study. Fig. 6.6

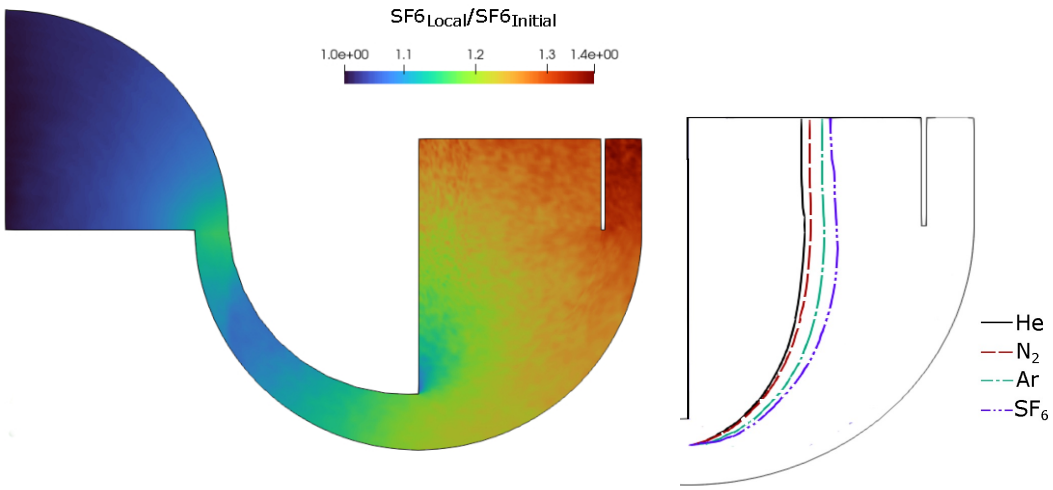

Figure 6.4: (a)Normalized mole fraction contours of SF_6 and (b) streamlines of different species

indicates the slip velocity between the species along the centreline. By decreasing the radius, the slip velocity between the species will increase, favoring the separation. The higher slip causes the enrichment of heavier species. However, as the curvature increases, the lateral separation effect is increased. Fig. 6.7 shows the mole fraction ratio of SF_6 variation perpendicular to the axis at two locations. It is observed that the difference between the concentration of the heavier species between the upper and lower wall increases with an increase in radius. At higher radii, the lateral separation effects dominate the streamwise separation.

6.4 Effect of wall temperature and back pressure

Simulations are conducted with three different wall temperatures, 300 K, 350 K, and 400 K, to study the wall temperature effect on species separation. Initially, the upper and lower walls are heated to the same temperature, and then the studies are repeated with different temperatures on the upper and lower walls. An equal molar mixture of N_2 and SF_6 is allowed to flow at an inlet pressure of 101 KPa through the nozzle. At higher temperatures, the molecule's kinetic energy will increase due to the heat transfer from the wall. Fig. 6.8 shows the increased velocity slip between the species at higher wall temperatures. High wall temperature will cause an increase in the binary mass diffusion coefficient. The cu-

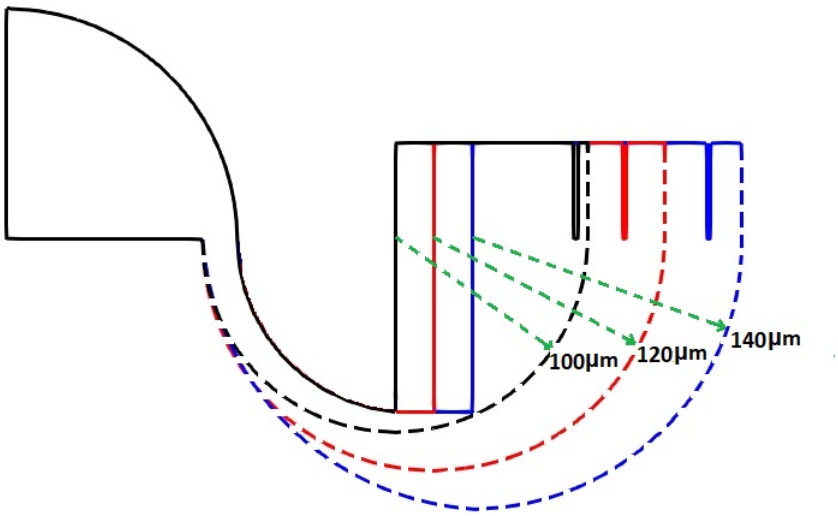

Figure 6.5: Different radius of curvature

mulative effect of these phenomena is an overall decrease in separation efficiency. Fig. 6.9 depicts the variation of the normalized mole fraction at the exit for different wall temperatures. Normalization is done with the mole fraction value of SF_6 at the bottom wall at a wall temperature of 300K. A temperature gradient between the top and bottom wall can induce a transport effect as the gases move towards the exit. The separation effects in a binary mixture depend on the molecular mass and the interaction between the molecules [202]. This phenomenon is usually known as the positive or negative Soret effect, depending on the movement of heavier or lighter components to lower or higher temperature regions. Different wall temperatures are used in simulations to determine the impact of thermal diffusion. Initially, the upper and lower walls are heated to the same temperature, and then the studies are repeated with different temperatures on the upper and lower walls. Terminologies such as HUT (High Upper wall Temperature), HLT (High Lower wall Temperature), and EULT (Equivalent Upper and Lower wall Temperature) have been considered to distinguish the different wall temperature conditions. The subscript ΔT will represent the temperature difference between the upper and lower walls, and in cases of equal wall temperatures, subscript T will stand in for the wall temperature. Different com-

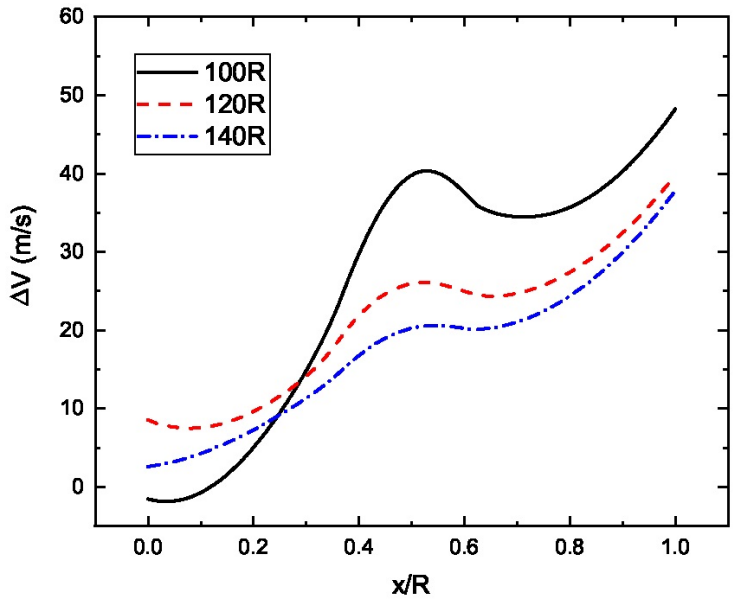

Figure 6.6: Slip velocity between the species along the central line for different radii of the lower wall

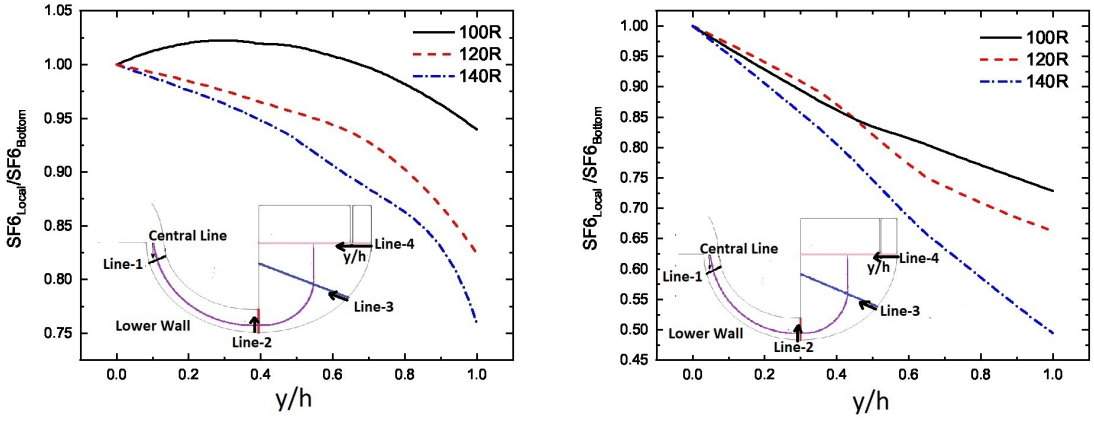

(a) Along Line-2 **(b)** Along Line-3

Figure 6.7: Normalized mole fraction SF_6 perpendicular to the axis at various locations for various curvatures of the nozzle

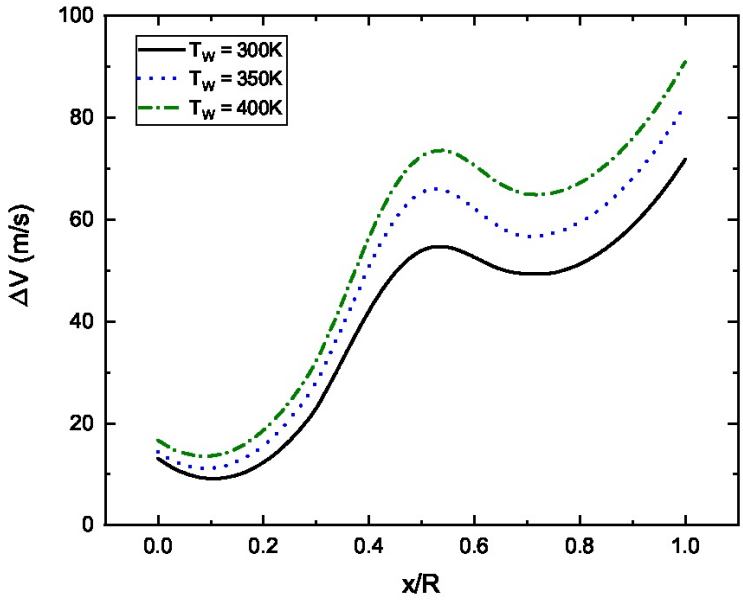

Figure 6.8: Slip velocity between the species along the central line for different wall temperatures

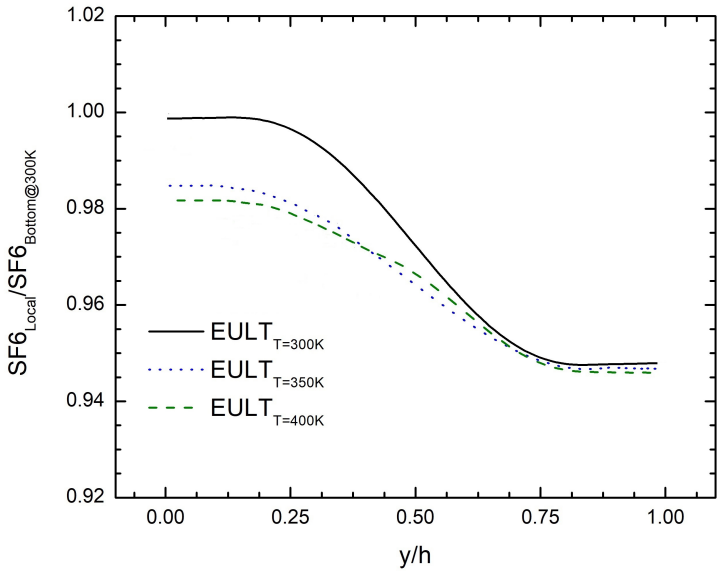

Figure 6.9: Normalized SF_6 mole fraction at the exit for different wall temperatures

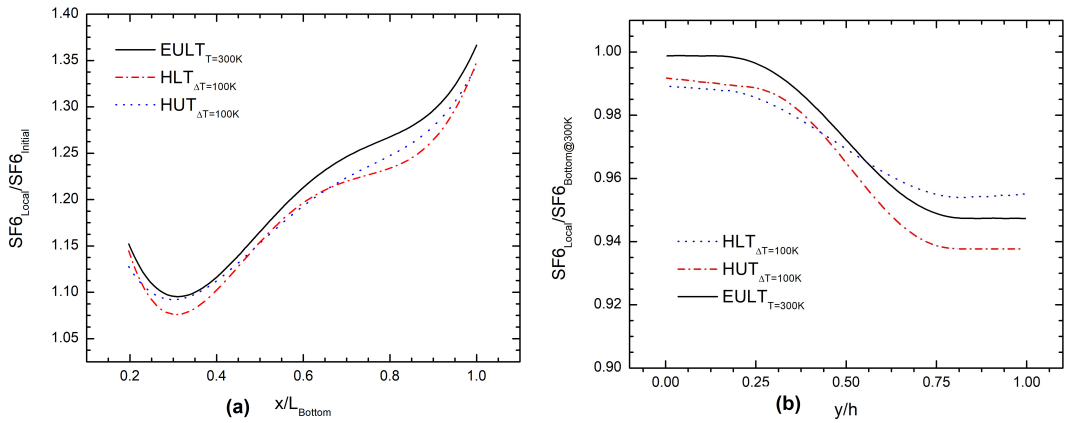

Figure 6.10: Normalized mole fraction of heavier species at different wall temperatures (a) at the bottom wall, (b) at the exit.

binations of wall heating have been simulated at temperatures of 300K, 350K, and 400K. Fig. 6.10a shows the normalized mole fraction of SF_6 on the lower wall of the nozzle, from the throat to the exit. The SF_6 mole fraction on the lower walls will drop if the top wall or lower wall is heated to a higher temperature, and this effect will be maximum when the lower wall is heated. SF_6 is the heavier species and is more concentrated on the lower wall, so a change in the lower wall temperature will affect the separation more than a change in the upper wall temperature, as shown in Fig. 6.10b. These changes may be due to thermal diffusion. Higher temperatures on the lower wall create a higher temperature gradient, facilitating the thermal diffusion of heavier species. This thermal diffusion will counteract the separation effect and force the heavier gas to move toward cold regions. The results indicate the influence of thermal diffusion, though insignificant in the present case. The effect may dominate when the convection effect reduces and may be helpful in applications that require the elimination of concentration gradients.

Ongoing simulations involve the variation of back pressure at exit conditions, specifically at 0, 5000, 10000, and 20000 Pa, while maintaining a constant inlet pressure of 100 kPa. As the simulations progress, it becomes evident that the maximum exit Kn number is attained under vacuum pressure conditions, reaching a value of 6. Additionally, a Kn number of 2 is observed when the back pressure is set at 20 kPa. In Fig. 6.11, the normalized mole fraction of SF_6 at the exit of the nozzle (referred to as line 1) is presented for different back pressure conditions. The graphical representation unmistakably illustrates that the highest mole fraction of SF_6 at the bottom wall occurs when the exit conditions are set to

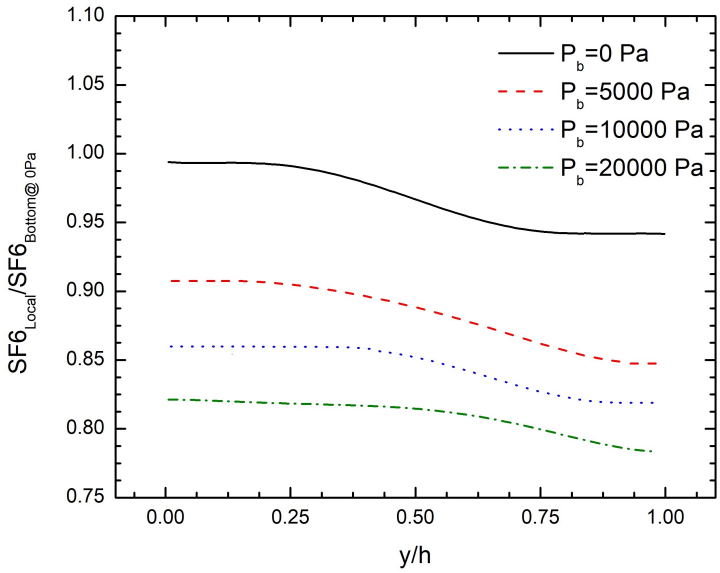

Figure 6.11: Normalized mole fraction of heavier species at the exit for different back pressures

a vacuum. Furthermore, an increase in backpressure correlates with a decrease in the SF_6 value at the bottom wall. This observation leads to the conclusion that rarefaction plays a significant role in promoting species separation. In other words, the conditions associated with lower pressure levels, particularly vacuum conditions, are conducive to a higher concentration of SF_6 at the bottom wall, whereas higher backpressure leads to a decrease in SF_6 concentration at the same location.

6.5 Comparison with linear design

The following study compares the effectiveness of linear and curved micronozzle designs to explore the efficiency of different configurations in separating species. The comparison involves evaluating two linear nozzle designs: one with a length equivalent to the curved nozzle and another with a divergent section length matching the total length of the curved nozzle. Additionally, the study analyzes the separation performance of two curved nozzle designs with divergent radii of 120μm and 140μm. The linear and curved nozzle designs maintain consistent dimensions, including throat height, exit, and inlet height, etc. Simulations are conducted under specific conditions, an inlet pressure of 100kPa, and an exit

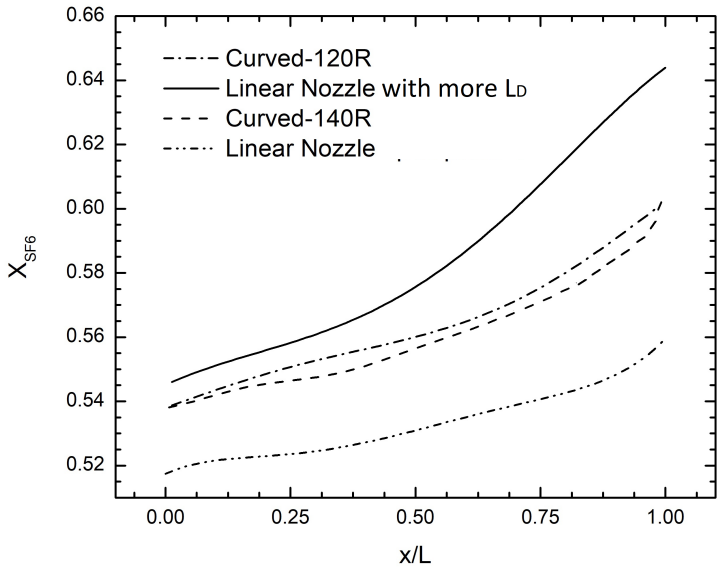

Figure 6.12: Variation of mole fraction of SF_6 varies along the centerline for various configurations

vacuum. The nozzle facilitates the flow of a binary gas mixture of N_2 and SF_6. By examining the mole fraction of SF_6 at different regions, a comparison is made to evaluate the separation performance of the two nozzles. Fig. 6.12 illustrates how the mole fraction of SF_6 varies along the centerline of linear nozzles and along the lower wall of a curved nozzle. In the curved nozzle, the lower wall is chosen because it has been observed that the heaviest species tends to deposit there, while deposition occurs at the centerline in the linear nozzle [201]. For both types of nozzles, the mole fraction of SF_6 increases as the nozzle length increases. When comparing nozzles with the same total length, the highly curved and linear nozzles perform similarly. However, among all the configurations discussed, the linear nozzle with a longer divergent section length exhibits the highest separation performance. The mole fraction of SF_6 at the exit plane of all nozzles is compared in Fig. 6.13. The results showed that the mole fraction decreased with an increase in exit height for the curved nozzle, while the linear nozzle exhibited a higher mole fraction at the center of the nozzle. This comparison also illustrates that linear nozzles with longer divergent lengths can outperform curved nozzles in species separation performance. The findings provide insights into the behaviour of gas flows in micro nozzles, which can be valuable for developing optimized nozzle designs for species separation applications.

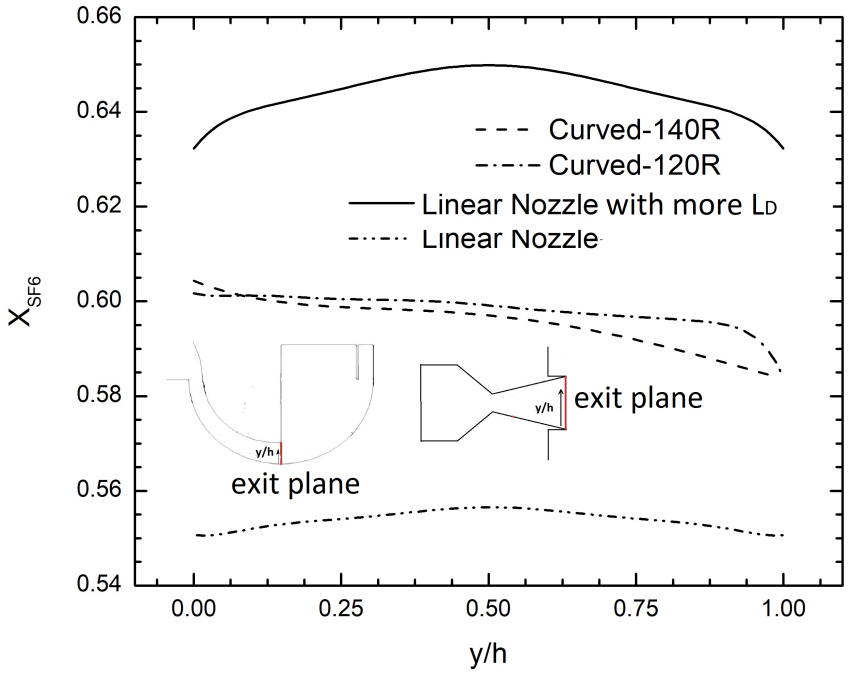

Figure 6.13: Variation of mole fraction of SF_6 varies along the exit plane for various configurations

Chapter 7
Conclusion

The aim of the present work is to find out an optimised size and shape of micronozzle for the thruster and species separation applications. Along with the experimental study, numerical studies are also conducted by using conventional Navier Stokes, DSMC, and hybrid methods. The knowledge gained helps us understand many important mechanisms that were previously speculative based on assumptions. This chapter presents a summary of the findings derived from this research. Additionally, suggestions for future endeavors are made to enhance and broaden the understanding of micronozzle flows related to satellite thrusters and aerodynamic separation processes.

7.1 Introduction

The study on micronozzles presented in this Ph.D. thesis holds significant relevance in the field. Micronozzles operate with a thick boundary layer dominated flow, which distinguishes them from conventional nozzles. The research aims to optimize the design of propulsion systems by considering factors such as nozzle throat dimension, divergence angle, length of the divergence section, and expansion ratio to address the build-up of the boundary layer. Previous literature shows varied findings on optimized divergence angles and the impact of back pressure, indicating the need for further investigation. Additionally, the study intends to explore the effects of divergent section contours, exit conditions, and curved geometry on flow features and separation performance, which have received limited attention in previous studies. The research employs computational methods to analyze the thrust production performance and aerodynamic separation process of micronozzles under different operating conditions, geometries, and wall conditions. The study identi-

fied the primary mechanisms involved in utilizing micronozzles for satellite propulsion and aerodynamic mixture separation. This research endeavor significantly contributes valuable insights to the field of micronozzle investigation. The significant outcomes of the study are described below.

7.2 Experimental approach

The experimental setup and measuring instruments created during the present study can be effectively utilized to pursue further investigations involving the testing of alternative micronozzle designs. The experimental investigation yielded the following outcomes.

- An experimental setup has been successfully designed for the study.
- A planar nozzle was designed and fabricated by using an EDM technique.
- The experiment is conducted and the nozzle exit velocity at a distance of 2.5,3.5 and 4.5mm away from the nozzle exit is measured.
- The interferometric Rayleigh scattering technique is found to be successful in the measurement of nozzle exit velocity with an uncertainty of 4.5%.
- Experimental results are used to validate the computational models developed.

7.3 Computational study on 2-D planar micronozzle for satellite propulsion

The performance of micro nozzles for thruster applications is investigated through a numerical study using NS with first-order slip boundary conditions, DSMC, and a hybrid approach. The study focused on examining the impact of various geometrical parameters such as throat depths (ranging from 2 to 200 μm), divergent angles (ranging from 5 to 30°), and divergent lengths. Additionally, the effect of nozzle wall heating and back pressure on the nozzle's performance is explored. Based on these investigations, the following conclusions are drawn:

- The lowest divergence angle of 5° produced the highest thrust under these conditions irrespective of the operating pressure differences and throat size.

- When the divergence lengths are high, the increase in divergence angle does not enhance the mitigation of viscous losses.
- A significant change in the subsonic layer and flow features is noticed on the divergent section with the changes in wall thermal condition.
- The decrease in subsonic layer size with a reduction in temperature creates a performance improvement.
- Literature suggests different divergence angles for achieving optimal performance. However, the present study's findings indicate that the specific operating conditions and the dimensions of the micronozzles employed primarily influence these variations.
- Under conditions of low-pressure differences, the flow within the divergent section of the micronozzle remains predominantly subsonic. However, it accelerates due to the effective area decrease caused by the expanding thick boundary layer.
- Micronozzle size effects are found to be significant while operating under lower pressure differences.
- The flow at higher pressure differences is characterized by clear flow separation and the occupation of the separated flow to a considerable portion of the divergent section.
- Re is very low as the nozzle size decreases to the nanoscale, and the subsonic layer fully occupies the divergent nozzle section even at very high-pressure differences.
- The error in thrust calculations due to viscous force effects is found to be negligible. However, the results suggest that these effects can become noticeable in the case of a nanoscale nozzle operating under conditions of vacuum exit.

The study is extended to the micronozzle in a cluster arrangement by the varying pitch of the nozzle arrangement (100-1000μm) and wall temperature (300-1000k) and this study leads to the conclusions that

- The thrust beyond 300μm thruster spacing and I_{sp} are found to be increasing with an increase in pitch.
- The thrust beyond 300μm thruster spacing and I_{sp} are found to be increasing with an increase in pitch. The decrease in thrust and a slight increase in Isp are observed with an increase in wall temperature.

- The thrust beyond 300μm thruster spacing and I_{sp} are found to be increasing with an increase in pitch. The maximum value of the Mach number of the flow is found to be increasing with an increase in pitch and decreasing wall temperature.

7.4 A correlation for thrust calculation

A new correlation for thrust calculation in micronozzles has been proposed with a correlation coefficient of 0.97. The proposed correlation for thrust per unit width can be expressed as follows

$$Thrust/width = AX^b \tag{7.1}$$

where A and b are 71587.8 and –0.6 respectively. The parameter X is defined as

$$X = \frac{sin^2\theta}{AR^2}\frac{P_0}{\Delta P}\frac{\epsilon}{\epsilon - 1} \tag{7.2}$$

This correlation is only applicable in the studied flow regimes such as throat depths (ranging from 2 to 200 μm), divergent angles (ranging from 5 to 30°), and pressure difference (70 and 30 kPa). It is observed that the performance is highly influenced by the area ratio, length of the divergent wall, and pressure difference across the nozzle.

7.5 Computational studies on aerodynamic separation

The binary separation characteristics of 2-D planar micronozzles with various divergent section contours (linear, bell, and trumpet), divergent angles (ranging from 15 to 45°), and back pressures (ranging from 0 to 30 kPa) are investigated computationally. The direct simulation Monte Carlo method is employed for simulations to analyze the effectiveness of separation. The study explores species separation in carrier gases such as N_2 and Kr. Additionally, investigations are conducted on curved micronozzles with varying radii of curvature in the divergent sections (ranging from 100 μm to 140 μm), wall temperatures (ranging from 300 K to 400 K), and back pressures (ranging from 0 to 20 kPa). The following conclusions are drawn from these studies:

- The aerodynamic separation effect is created mainly by (i) streamwise separation produced by the velocity slip between species and (ii) lateral separation created by the curving of streamlines. The two phenomena are depicted in Fig. 7.1. Streamwise separation increased with a decrease in throat size, whereas lateral separation

increased with an increase in throat size.

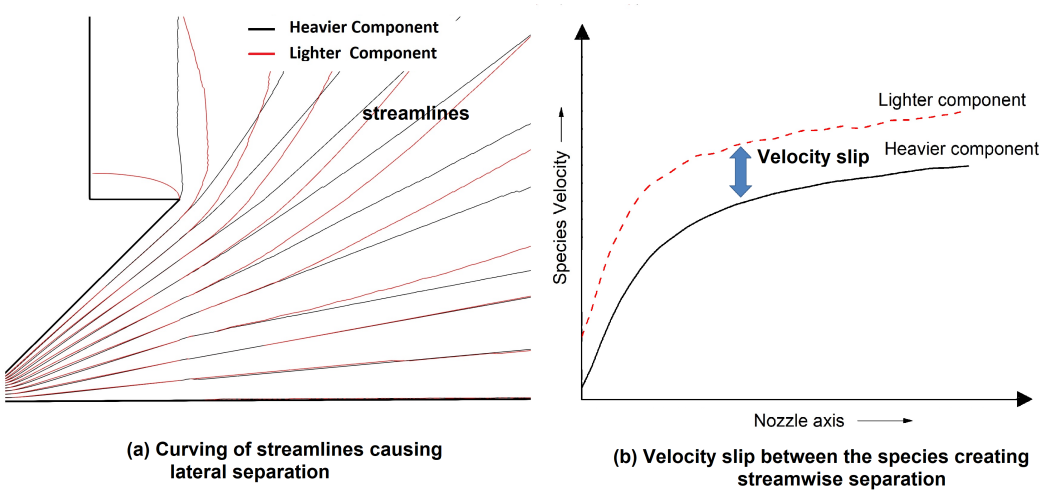

Figure 7.1: Types of species separation phenomenon of a mixture observed in micronozzles

- The studies with various micronozzles of different throat sizes indicate that the species separation performance depends on exit Kn. When the exit Kn is higher, a greater concentration of heavier species is anticipated near the axis. In contrast, a lower Kn value corresponds to a higher concentration of lighter species near the wall.
- Back pressure at the nozzle exit significantly affects streamline curvature and flow characteristics, particularly impacting mixture separation performance.
- Trumpet, truncated bell, and linear nozzle with high divergence angle showed higher lateral separation.
- For the trumpet nozzle, higher curving of the streamlines facilitates higher lateral separation.
- A thicker subsonic layer is present in the divergent section of the bell nozzle owing to higher flow alignment. This reduced the average exit Mach number, slip velocity, and separation performance.

- High back pressure conditions at the exit of the nozzle create a dominant subsonic flow region in the nozzle divergent part, flow turning, and deflection of the exit momentum in the transverse direction.
- The introduction of carrier gas has decreased the species separation effect at the nozzle exit.
- Adding a heavier carrier gas reduces the lateral separation effect due to the low turning of streamlines.
- The highest mole fraction for the linear nozzle is observed for the higher divergence angle (45°) studied for the linear nozzle.
- In the curved nozzle, the increase in wall temperature facilitated the separation of species by increasing the velocity slip between them.
- The separation performance in curved nozzles is significantly influenced by lateral separation resulting from mass ratio and mass diffusion.
- Streamwise separation, lateral separation, mass diffusion, and thermal diffusion can affect the separation performance of a curved nozzle. Further influencing the separation performance are factors such as the nozzle shape, nozzle overall length, wall temperature conditions, molecular mass ratio, and inlet mole fraction of the species.
- The separation performance improves with more curvature because of the compounding effect of the lateral separation effects.
- In terms of separation performance, it is found that linear nozzles with longer divergent lengths performed better compared to curved nozzles.

The optimum nozzle angle for the thruster application is found to be 5° for the studied flow regime at constant divergent length cases. But if the divergent angle is varied by varying divergent lengths, then the optimum angle is fall within 15-20°. On the contrary higher divergence angle is found to be shown higher species separation compared to lower angles in linear nozzles.

7.6 Conclusive Summary

The research findings indicate that the specific operating conditions and micronozzle dimensions greatly influence the optimized divergence angles and the impact of back pres-

sure. The study highlights the importance of the thick boundary layer dominated flow in micronozzles and its effects on thrust production and mixture separation. Additionally, the research explores the influence of divergent section contours, exit conditions, and curved geometry on flow characteristics and separation performance, which were previously understudied.

The experimental setup and measuring instruments developed in this study offer further opportunities for investigating alternative micronozzle designs. The study also proposes a correlation for thrust calculation in micronozzles, providing a useful tool for engineers. The computational studies on aerodynamic separation shed light on the significant role played by lateral separation due to mass ratio and mass diffusion.

In conclusion, the findings of this study hold significant implications for the advancement of micronozzle designs employed in satellite propulsion and aerodynamic separation processes. By evaluating the feasibility of micronozzles for continuous real-time applications, particularly in the realm of aerodynamic mixture separation, this research paves the way for developing compact and highly responsive sensors crucial for real-time detection purposes. These contributions will undoubtedly shape the future of micronozzle technology, enabling more efficient and effective propulsion systems and facilitating breakthroughs in real-time sensing capabilities.

7.7 Future work

In the current scenario, the qualitative experimental results on the micronozzle operating in the vacuum are limited. The DSMC method can be used to evaluate the micronozzle performance in the presence of wall surface roughness. This requires even more computational efforts which are out of the scope of the present thesis work. But, it can be done as an extension of the ongoing work. The hybrid approach can also be optimized with new modified Knudsen numbers. Some suggestions for future studies are listed below

1. Conduct a micronozzle flow experimental study in vacuum back pressure conditions to measure plume characteristics for space applications.

2. Complete the experimental study on micronozzle by using micro-PIV to investigate the internal flow features of micronozzle

3. Numerically study the effect of back pressure and divergent shape by incorporating wall surface roughness with the help of the DSMC method.

4. Reduce the computational effort of the hybrid approach by proper selection of NS-DSMC interface by using modified Knudsen number like Knudsen number based on entropy etc.

5. Reduce the computation effort of DSMC by implementing zone DSMC initialization scheme in the divergent part of the micronozzle.

Bibliography

[1] Y. Krishna, A. Sekar, G. Magnotti, and A. Vaidyanathan, "One-dimensional interferometric scattering velocimetry for high-speed flows," in *25th AIAA International Space Planes and Hypersonic Systems and Technologies Conference*, 2023, p. 3046.

[2] S. Grisnik, T. Smith, and S. Larry, "Experimental study of low reynolds number nozzles," in *19th International Electric Propulsion Conference*, 1987, p. 992.

[3] D. Zelesnik, M. M. Micci, and L. N. Long, "Direct simulation monte carlo model of low reynolds number nozzle flows," *Journal of Propulsion and Power*, vol. 10, no. 4, pp. 546–553, 1994.

[4] A. Zilic, D. Hitt, and A. Alexeenko, "Numerical simulations of supersonic flow in a linear aerospike micro nozzle," in *37th AIAA Fluid Dynamics Conference and Exhibit*, 2007, p. 3984.

[5] A. Z. Giovannini and R. S. Abhari, "Rarefied flow expansion in linear aerospikes," *Physics of Fluids*, vol. 27, no. 6, p. 062003, 2015.

[6] G. Angelino, "Approximate method for plug nozzle design," *AIAA Journal*, vol. 2, no. 10, pp. 1834–1835, 1964.

[7] S. Berry, V. V. Laurens, N. F. Tata, G. Tor-Arne, R. Pelle, S. Herbert, N. Muriel, V. Richard, M. Bert, S. John, B. Alexandra, and D. C. D. Maria, "Development of mems based electric propulsion," in *Space Propulsion Conference 2010*, no. CONF, 2010.

[8] A. Kogan, "Separation of a gas mixture in curved supersonic flow," *International Journal of Heat and Mass Transfer*, vol. 9, no. 1, pp. 1–10, 1966.

[9] M. Sabouri and M. Darbandi, "Numerical study of species separation in rarefied gas mixture flow through micronozzles using dsmc," *Physics of Fluids*, vol. 31, no. 4, p. 042004, 2019.

[10] T. Villela, C. A. Costa, A. M. Brandão, F. T. Bueno, and R. Leonardi, "Towards the thousandth cubesat: A statistical overview," *International Journal of Aerospace Engineering*, vol. 2019, 2019.

[11] M. A. Silva, D. C. Guerrieri, A. Cervone, and E. Gill, "A review of mems micropropulsion technologies for cubesats and pocketqubes," *Acta Astronautica*, vol. 143, pp. 234–243, 2018.

[12] C. Gentgen, S. Baber, W. E. Parker, E. Sirieys, S. Vigil, B. Yu, M. R. Apodaca Moreno, D. Erkel, M. A. Hoying, S. Lombardo, A. Makikalli, U. Ovienmhada, E. Crawley, O. L. De Weck, and C. Onecin, "A path to flight for reconfigurable satellite constellations: Mission design and systems architecture," in *ASCEND 2021*, 2021, p. 4146.

[13] C. Xie, "Characteristics of micronozzle gas flows," *Physics of Fluids*, vol. 19, no. 3, p. 037102, 2007.

[14] S. Li, *Design, fabrication and testing of micronozzles for gas sensing applications*. University of Maryland, College Park, 2006.

[15] G. W. Hunter, S. Akbar, S. Bhansali, M. Daniele, P. D. Erb, K. Johnson, C.-C. Liu, D. Miller, O. Oralkan, P. J. Hesketh *et al.*, "Editors' choice—critical review—a critical review of solid state gas sensors," *Journal of The Electrochemical Society*, vol. 167, no. 3, p. 037570, 2020.

[16] S.-I. Ohira and K. Toda, "Micro gas analyzers for environmental and medical applications," *Analytica Chimica Acta*, vol. 619, no. 2, pp. 143–156, 2008.

[17] N. Bykov and V. Zakharov, "Rarefied gas mixtures with large species mass ratio: Outflow into vacuum," *Physics of Fluids*, vol. 34, no. 5, p. 057106, 2022.

[18] D. E. Rothe, "Electron-beam studies of viscous flow in supersonic nozzles," *AIAA Journal*, vol. 9, no. 5, pp. 804–811, 1971.

[19] E. W. Spisz, P. F. Brinich, and J. R. Jack, "Thrust coefficients of low-thrust nozzles," NASA, Lewis research Center, Tech. Rep., 1965.

[20] C. Murch, J. Broadwell, A. Silver, and T. Marcisz, "Low-thrust nozzle performance," *AIAA paper*, no. AIAA-1968-91, 1968.

[21] M. V. Whalen, "Low reynolds number nozzle flow study. ms thesis," NATIONAL AERONAUTICS AND SPACE ADMINISTRATION, NASA-TR- 10D130, Tech. Rep., 1987.

[22] B. Reed, "Decomposing solid micropropulsion nozzle performance issue, aiaa 2003-0672," in *41st Aerospace Sciences Meeting & Exhibit, Reno, NV,*, 2003.

[23] A. R. Bruccoleri, R. Leiter, M. Drela, and P. Lozano, "Experimental effects of nozzle geometry on flow efficiency at low reynolds numbers," *Journal of Propulsion and Power*, vol. 28, no. 1, pp. 96–105, 2012.

[24] J. D. Mirczak, "Milli-newton thrust stand for electric propulsion," Ph.D. dissertation, Massachusetts Institute of Technology, 2003.

[25] L. T. Williams, M. McDonald, and M. Osborn, "Performance characterization of a low reynolds number micro-nozzle flo," in *51st AIAA/SAE/ASEE Joint Propulsion Conference*, 2015, p. 3924.

[26] L. T. Williams, M. S. McDonald, and M. F. Osborn, "Performance and vibration characterization of a low-thrust torsional thrust balance," in *35th International Electric Propulsion Conference*, 2017.

[27] Z. Bao-jun, L. Xing-chen, H. Yi-yong, and X. Xiang-ming, "Experimental research on micro-nozzle applied on micro-propulsion systems based on mems," in *IOP Conference Series: Materials Science and Engineering*, vol. 187, no. 1. IOP Publishing, 2017, p. 012044.

[28] K. Nishii, H. Koizumi, and K. Komurasaki, "Experimental characterization of nozzle performance at low reynolds numbers for water microthrusters," *Journal of Propulsion and Power*, vol. 37, no. 4, pp. 595–603, 2021.

[29] D. Seo, Y. Ryu, J. Choi, and J. Lee, "Design, fabrication, and calibration of a micro-load cell for micro-resistojet development," *Review of Scientific Instruments*, vol. 92, no. 11, p. 115002, 2021.

[30] A. J. Jamison, A. D. Ketsdever, and E. Muntz, "Gas dynamic calibration of a nano-newton thrust stand," *Review of Scientific Instruments*, vol. 73, no. 10, pp. 3629–3637, 2002.

[31] M. Gamero-Castano, "A torsional balance for the characterization of micronewton thrusters," *Review of scientific instruments*, vol. 74, no. 10, pp. 4509–4514, 2003.

[32] A. P. Pancotti, M. Gilpin, and M. S. Hilario, "Comparison of electrostatic fins with piezoelectric impact hammer techniques to extend impulse calibration range of a torsional thrust stand," *Review of Scientific Instruments*, vol. 83, no. 3, p. 035109, 2012.

[33] J. E. Polk, A. Pancotti, T. Haag, S. King, M. Walker, J. Blakely, and J. Ziemer, "Recommended practice for thrust measurement in electric propulsion testing," *Journal of Propulsion and Power*, vol. 33, no. 3, pp. 539–555, 2017.

[34] P.-F. Hao, Y.-T. Ding, Z.-H. Yao, F. He, and K.-Q. Zhu, "Size effect on gas flow in micro nozzles," *Journal of Micromechanics and Microengineering*, vol. 15, no. 11, p. 2069, 2005.

[35] C. Huang, J. W. Gregory, and J. P. Sullivan, "Flow visualization and pressure measurement in micronozzles," *Journal of visualization*, vol. 10, no. 3, pp. 281–288, 2007.

[36] H. Nagai, R. Naraoka, K. Sawada, and K. Asai, "Pressure-sensitive paint measurement of pressure distribution in a supersonic micronozzle," *AIAA journal*, vol. 46, no. 1, pp. 215–222, 2008.

[37] Y. Matsuda, T. Uchida, S. Suzuki, R. Misaki, H. Yamaguchi, and T. Niimi, "Pressure-sensitive molecular film for investigation of micro gas flows," *Microfluidics and Nanofluidics*, vol. 10, no. 1, pp. 165–171, 2011.

[38] M. Namura and T. Toriyama, "Experimental study on aerodynamics of microelectromechanical systems based single-crystal-silicon microscale supersonic nozzle," *Journal of fluids engineering*, vol. 135, no. 8, 2013.

[39] J. Gomez and R. Groll, "Pressure drop and thrust predictions for transonic micronozzle flows," *Physics of Fluids*, vol. 28, no. 2, p. 022008, 2016.

[40] I. Timofeev and V. Aniskin, "Experimental research of the supersonic core length in the supersonic jet flowing from the rectangular micro-nozzles with different aspect ratios," in *Journal of Physics: Conference Series*, vol. 1404, no. 1. IOP Publishing, 2019, p. 012099.

[41] T. Nagata, M. Kasai, T. Okudera, H. Sato, T. Nonomura, and K. Asai, "Optimum pressure range evaluation toward aerodynamic measurements using psp in low-pressure conditions," *Measurement Science and Technology*, vol. 31, no. 8, p. 085303, 2020.

[42] I. D. Boyd, D. B. VanGilder, and E. J. Beiting, "Computational and experimental investigations of rarefied flows in small nozzles," *AIAA journal*, vol. 34, no. 11, pp. 2320–2326, 1996.

[43] A. Broc, S. De Benedictis, G. Dilecce, M. Vigliotti, R. Sharafutdinov, and P. Skovorodko, "Experimental and numerical investigation of an o _{2}/no supersonic free jet expansion," *Journal of Fluid Mechanics*, vol. 500, pp. 211–237, 2004.

[44] A. Choudhuri, B. Baird, S. Gollahalli, and S. Schneider, "Effects of geometry and ambient pressure on micronozzle flow," in *37th Joint Propulsion Conference and Exhibit*, 2001, p. 3331.

[45] W. R. Lempert, N. Jiang, S. Sethuram, and M. Samimy, "Molecular tagging velocimetry measurements in supersonic microjets," *AIAA journal*, vol. 40, no. 6, pp. 1065–1070, 2002.

[46] T. Handa, Y. Matsuda, and Y. Egami, "Phenomena peculiar to underexpanded flows in supersonic micronozzles," *Microfluidics and Nanofluidics*, vol. 20, no. 12, p. 166, 2016.

[47] A. Z. Nazari, Y. Ishino, Y. Ishiko, F. Ito, H. Kondo, R. Yamada, T. Motohiro, Y. Miyazato, and S. Nakao, "Multi-schlieren ct measurements of supersonic microjets from circular and square micro nozzles," *Journal of Flow Control, Measurement & Visualization*, vol. 8, no. 03, p. 77, 2020.

[48] H. Maeda, H. Fukuda, S. Nakao, Y. Miyazato, and Y. Ishino, "Rainbow schlieren measurements in underexpanded jets from square supersonic micro nozzles," in *EPJ Web of Conferences*, vol. 180. EDP Sciences, 2018, p. 02058.

[49] V. Kozlov, G. Grek, M. Litvinenko, Y. A. Litvinenko, and A. Shmakov, "Experimental study of diffusion combustion of high-speed hydrogen round microjet efflux from supersonic laval micronozzle," *Journal of Engineering Thermophysics*, vol. 29, no. 2, pp. 245–253, 2020.

[50] A. Z. Nazari, Y. Ishino, F. Ito, H. Kondo, R. Yamada, T. Motohiro, Y. Saiki, Y. Miyazato, and S. Nakao, "Quantitative schlieren image-noise reduction using inverse process and multi-path integration," *Journal of Flow Control, Measurement & Visualization*, vol. 8, no. 2, pp. 25–44, 2020.

[51] G. S. Settles and M. J. Hargather, "A review of recent developments in schlieren and shadowgraph techniques," *Measurement Science and Technology*, vol. 28, no. 4, p. 042001, 2017.

[52] G. A. Bird and J. Brady, *Molecular gas dynamics and the direct simulation of gas flows*. Clarendon press Oxford, 1994, vol. 42.

[53] M. C. Cline, "Computation of two-dimensional, viscous nozzle flow," *AIAA Journal*, vol. 14, no. 3, pp. 295–296, 1976.

[54] S. C. Kim, "Calculations of low-reynolds-number resistojet nozzles," *Journal of Spacecraft and Rockets*, vol. 31, no. 2, pp. 259–264, 1994.

[55] S. Gokhale and R. Suresh, "Numerical computations of internal flows for axisymmetric and two-dimensional nozzles," *International journal for numerical methods in fluids*, vol. 25, no. 5, pp. 599–610, 1997.

[56] B. Maté, I. A. Graur, T. Elizarova, I. Chirokov, G. Tejeda, J. Fernandez, and S. Montero, "Experimental and numerical investigation of an axisymmetric supersonic jet," *Journal of Fluid Mechanics*, vol. 426, pp. 177–197, 2001.

[57] A. Tsimpoukis and D. Valougeorgis, "Pulsatile pressure driven rarefied gas flow in long rectangular ducts," *Physics of Fluids*, vol. 30, no. 4, p. 047104, 2018.

[58] S. Naris, D. Valougeorgis, D. Kalempa, and F. Sharipov, "Flow of gaseous mixtures through rectangular microchannels driven by pressure, temperature, and concentration gradients," *Physics of fluids*, vol. 17, no. 10, p. 100607, 2005.

[59] L. Wu, J. Zhang, H. Liu, Y. Zhang, and J. M. Reese, "A fast iterative scheme for the linearized boltzmann equation," *Journal of Computational Physics*, vol. 338, pp. 431–451, 2017.

[60] R. K. Agarwal, K.-Y. Yun, and R. Balakrishnan, "Beyond navier–stokes: Burnett equations for flows in the continuum–transition regime," *Physics of Fluids*, vol. 13, no. 10, pp. 3061–3085, 2001.

[61] X.-j. Gu and D. R. Emerson, "A high-order moment approach for capturing non-equilibrium phenomena in the transition regime," *Journal of fluid mechanics*, vol. 636, pp. 177–216, 2009.

[62] C. P. Zinner and H. C. Öttinger, "Entropic boundary conditions for 13 moment equations in rarefied gas flows," *Physics of Fluids*, vol. 31, no. 2, p. 021215, 2019.

[63] Y. Yuan and S. Rahman, "Extended application of lattice boltzmann method to rarefied gas flow in micro-channels," *Physica A: Statistical Mechanics and its Applications*, vol. 463, pp. 25–36, 2016.

[64] M. Watari, "Is the lattice boltzmann method applicable to rarefied gas flows? comprehensive evaluation of the higher-order models," *Journal of Fluids Engineering*, vol. 138, no. 1, 2016.

[65] A. D. Ketsdever, M. T. Clabough, S. F. Gimelshein, and A. Alexeenko, "Experimental and numerical determination of micropropulsion device efficiencies at low reynolds numbers," *AIAA journal*, vol. 43, no. 3, pp. 633–641, 2005.

[66] C. Ngalande, T. Lilly, M. Killingsworth, S. Gimelshein, and A. Ketsdever, "Nozzle plume impingement on spacecraft surfaces: Effects of surface roughness," *Journal of spacecraft and rockets*, vol. 43, no. 5, pp. 1013–1018, 2006.

[67] J. C. Maxwell, "Vii. on stresses in rarified gases arising from inequalities of temperature," *Philosophical Transactions of the royal society of London*, no. 170, pp. 231–256, 1879.

[68] R. Deissler, "An analysis of second-order slip flow and temperature-jump boundary conditions for rarefied gases," *International Journal of Heat and Mass Transfer*, vol. 7, no. 6, pp. 681–694, 1964.

[69] J. Maurer, P. Tabeling, P. Joseph, and H. Willaime, "Second-order slip laws in microchannels for helium and nitrogen," *Physics of Fluids*, vol. 15, no. 9, pp. 2613–2621, 2003.

[70] R. Myong, J. Reese, R. W. Barber, and D. Emerson, "Velocity slip in microscale cylindrical couette flow: The langmuir model," *Physics of fluids*, vol. 17, no. 8, p. 087105, 2005.

[71] X. Li, J. Yuan, X. Ren, and G. Cai, "Simulation applicability verification of various slip models in micro-nozzle," *Acta Astronautica*, vol. 192, pp. 68–76, 2022.

[72] P. Bahukudumbi, "A unified engineering model for steady and quasi-steady shear-driven gas microflows," *Microscale Thermophysical Engineering*, vol. 7, no. 4, pp. 291–315, 2003.

[73] A. Agrawal and S. Prabhu, "Deduction of slip coefficient in slip and transition regimes from existing cylindrical couette flow data," *Experimental thermal and fluid science*, vol. 32, no. 4, pp. 991–996, 2008.

[74] N. T. Le, C. White, J. M. Reese, and R. S. Myong, "Langmuir–maxwell and langmuir–smoluchowski boundary conditions for thermal gas flow simulations in hypersonic aerodynamics," *International Journal of Heat and Mass Transfer*, vol. 55, no. 19-20, pp. 5032–5043, 2012.

[75] C. Cercignani and A. Daneri, "Flow of a rarefied gas between two parallel plates," *Journal of Applied Physics*, vol. 34, no. 12, pp. 3509–3513, 1963.

[76] H. Brenner, "Navier–stokes revisited," *Physica A: Statistical Mechanics and its Applications*, vol. 349, no. 1-2, pp. 60–132, 2005.

[77] H. Brenner, "Fluid mechanics revisited," *Physica A: Statistical Mechanics and its Applications*, vol. 370, no. 2, pp. 190–224, 2006.

[78] F. Durst, J. Gomes, and R. Sambasivam, "Thermofluiddynamics: Do we solve the right kind of equations?" in *Turbulence Heat and Mass Transfer 5. Proceedings of the International Symposium on Turbulence Heat and Mass Transfer*. Begel House Inc., 2006.

[79] R. Bayt, A. Ayon, K. Breuer, R. Bayt, A. Ayon, and K. Breuer, "A performance evaluation of mems-based micronozzles," in *33rd Joint Propulsion Conference and Exhibit*, 1997, p. 3169.

[80] J. A. Moríñigo and J. Hermida-Quesada, "Solid–gas surface effect on the performance of a mems-class nozzle for micropropulsion," *Sensors and Actuators A: Physical*, vol. 162, no. 1, pp. 61–71, 2010.

[81] G. E. Karniadakis, A. Beskok, and M. Gad-el Hak, "Micro flows: fundamentals and simulation," *Appl. Mech. Rev.*, vol. 55, no. 4, pp. B76–B76, 2002.

[82] A. A. Alexeenko, D. A. Levin, S. F. Gimelshein, R. J. Collins, and B. D. Reed, "Numerical modeling of axisymmetric and three-dimensional flows in microelectromechanical systems nozzles," *AIAA journal*, vol. 40, no. 5, pp. 897–904, 2002.

[83] A. Alexeenko, D. Levin, D. Fedosov, S. Gimelshein, and R. Collins, "Performance analysis of microthrusters based on coupled thermal-fluid modeling and simulation," *Journal of Propulsion and Power*, vol. 21, no. 1, pp. 95–101, 2005.

[84] T. Coakley, "Turbulence modeling methods for the compressible navier-stokes equations," in *16th Fluid and Plasmadynamics Conference*, 1983, p. 1693.

[85] W. Louisos and D. Hitt, "Viscous effects on performance of three-dimensional supersonic micronozzles," *Journal of Spacecraft and Rockets*, vol. 49, no. 1, pp. 51–58, 2012.

[86] H. Yan, W.-M. Zhang, Z.-K. Peng, and G. Meng, "Effect of three-dimensional surface topography on gas flow in rough micronozzles," *Journal of Fluids Engineering*, vol. 137, no. 5, 2015.

[87] S. K. Singh and A. K. R, "A parametric study on the fluid dynamics and performance characteristic of micronozzle flows," *Journal of Fluids Engineering*, vol. 144, no. 3, 2022.

[88] R. Groll, S. Kunze, and B. Besser, "Correction of second-order slip condition for higher knudsen numbers by approximation of free-molecular diffusion," *Physics of Fluids*, vol. 32, no. 9, p. 092008, 2020.

[89] G. Bird, "Approach to translational equilibrium in a rigid sphere gas," *Physics of fluids*, vol. 6, pp. 1518–1519, 1963.

[90] A. B. Weaver, "Assessment of high-fidelity collision models in the direct simulation monte carlo method," 2015.

[91] C.-H. Chung, S. C. Kim, R. M. Stubbs, and K. J. De Witt, "Low-density nozzle flow by the direct simulation monte carlo and continuum methods," *Journal of Propulsion and Power*, vol. 11, no. 1, pp. 64–70, 1995.

[92] G. A. Bird, "Molecular gas dynamics," *NASA STI/Recon Technical Report A*, vol. 76, 1976.

[93] K. Koura, "Null-collision technique in the direct-simulation monte carlo method," *The Physics of fluids*, vol. 29, no. 11, pp. 3509–3511, 1986.

[94] V. Yanitskiy, "Operator approach to direct simulation monte carlo theory in rarefied gas dynamics," in *Proc. 17th Symp. on Rarefied Gas Dynamics*. VCH New York, 1990, pp. 770–777.

[95] K. Nanbu, "Direct simulation scheme derived from the boltzmann equation. i. monocomponent gases," *Journal of the Physical Society of Japan*, vol. 49, no. 5, pp. 2042–2049, 1980.

[96] M. Ivanov and S. Rogasinskii, "Theoretical analysis of traditional and modern schemes of the dsmc method," in *Rarefied gas dynamics*, 1991, pp. 629–642.

[97] O. M. Belotserkovskii and V. Yanitskii, "The statistical particles-in-cells method for solving rarefied gas dynamics problems," *USSR Computational Mathematics and Mathematical Physics*, vol. 15, no. 5, pp. 101–114, 1975.

[98] S. K. Stefanov, "Particle monte carlo algorithms with small number of particles in grid cells," in *International Conference on Numerical Methods and Applications*. Springer, 2010, pp. 110–117.

[99] E. Roohi and S. Stefanov, "Collision partner selection schemes in dsmc: From micro/nano flows to hypersonic flows," *Physics Reports*, vol. 656, pp. 1–38, 2016.

[100] G. LeBeau, K. Jacikas, and F. Lumpkin, "Virtual sub-cells for the direct simulation monte carlo method," in *41st Aerospace Sciences Meeting and Exhibit*, 2003, p. 1031.

[101] G. Bird, "Visual dsmc program for two-dimensional and axially symmetric flows," *The DS2V Program User's Guide, Version 3.8, GAB Consulting, Sydney, Australia, October 2006*, 2006.

[102] B. Goshayeshi, E. Roohi, and S. Stefanov, "A novel simplified bernoulli trials collision scheme in the direct simulation monte carlo with intelligence over particle distances," *Physics of Fluids*, vol. 27, no. 10, p. 107104, 2015.

[103] S. A. Saadati and E. Roohi, "Detailed investigation of flow and thermal field in micro/nano nozzles using simplified bernoulli trial (sbt) collision scheme in dsmc," *Aerospace Science and Technology*, vol. 46, pp. 236–255, 2015.

[104] G. N. Markelov and M. S. Ivanov, "Numerical study of 2d/3d micronozzle flows," in *AIP Conference Proceedings*, vol. 585, no. 1. American Institute of Physics, 2001, pp. 539–546.

[105] T. Hyakutake and K. Yamamoto, "Numerical simulation of rarefied plume flow exhausting from a small nozzle," in *AIP Conference Proceedings*, vol. 663, no. 1. American Institute of Physics, 2003, pp. 604–611.

[106] A. A. Alexeenko, D. Levin, S. Gimelshein, R. Collins, and G. Markelov, "Numerical simulation of high-temperature gas flows in a millimeter-scale thruster," *Journal of Thermophysics and Heat Transfer*, vol. 16, no. 1, pp. 10–16, 2002.

[107] A. Alexeenko, D. Levin, S. Gimelshein, and B. Reed, "Numerical investigation of physical processes in high-temperature mems-based nozzle flows," in *AIP Conference Proceedings*, vol. 663, no. 1. American Institute of Physics, 2003, pp. 760–767.

[108] M. Wang and Z. Li, "Numerical simulations on performance of mems-based nozzles at moderate or low temperatures," *Microfluidics and Nanofluidics*, vol. 1, no. 1, pp. 62–70, 2004.

[109] C. Borgnakke and P. S. Larsen, "Statistical collision model for monte carlo simulation of polyatomic gas mixture," *Journal of computational Physics*, vol. 18, no. 4, pp. 405–420, 1975.

[110] G. W. Finger, J. S. Kapat, and A. Bhattacharya, "Molecular dynamics simulation of adsorbent layer effect on tangential momentum accommodation coefficient," *J. Fluids Eng.*, vol. 129, no. 1, pp. 31–39, 2007.

[111] B.-Y. Cao, J. Sun, M. Chen, and Z.-Y. Guo, "Molecular momentum transport at fluid-solid interfaces in mems/nems: a review," *International journal of molecular sciences*, vol. 10, no. 11, pp. 4638–4706, 2009.

[112] A. Agrawal, "A comprehensive review on gas flow in microchannels," *International Journal of Micro-Nano Scale Transport*, 2012.

[113] l. D. Boyd, P. F. Penko, D. L. Meissner, and K. J. DeWitt, "Experimental and numerical investigations of low-density nozzle and plume flows of nitrogen," *AIAA journal*, vol. 30, no. 10, pp. 2453–2461, 1992.

[114] Z. Yang and Y. H. Wei, "Gas flow simulation in a micro nozzle," *Aircraft Engineering and Aerospace Technology*, 2006.

[115] D. Watvisave, U. Bhandarkar, and B. Puranik, "Investigation of wall effects on flow characteristics of a high knudsen number nozzle," *Nanoscale and microscale thermophysical engineering*, vol. 17, no. 2, pp. 124–140, 2013.

[116] A. Alexeenko, R. Collins, S. Gimelshein, and D. Levin, "Challenges of three-dimensional modeling of microscale propulsion devices with the dsmc method," in *AIP Conference Proceedings*, vol. 585, no. 1. American Institute of Physics, 2001, pp. 464–471.

[117] E. Titov and D. Levin, "Application of the dsmc and ns techniques to the modeling of a dense, low reynold's number mems device," in *AIP Conference Proceedings*, vol. 762, no. 1. American Institute of Physics, 2005, pp. 761–766.

[118] C. Shen, J. Fan, and C. Xie, "Statistical simulation of rarefied gas flows in micro-channels," *Journal of Computational Physics*, vol. 189, no. 2, pp. 512–526, 2003.

[119] M. Darbandi and E. Roohi, "Study of subsonic–supersonic gas flow through micro/nanoscale nozzles using unstructured dsmc solver," *Microfluidics and nanofluidics*, vol. 10, no. 2, pp. 321–335, 2011.

[120] V. Lijo, T. Setoguchi, and H. Kim, "Analysis of supersonic micronozzle flows," *Journal of Propulsion and Power*, vol. 31, no. 2, pp. 754–757, 2015.

[121] T. D. Holman and M. F. Osborn, "On the validation of direct simulation monte carlo method for low reynolds number micro-nozzle resisto-jets," in *35th International Electric Propulsion Conference, Georgia*, 2017.

[122] T. Holman and M. Osborn, "Comparison of dsmc and experimental data for low reynolds number micro-nozzle," in *2018 Joint Propulsion Conference*, 2018, p. 4816.

[123] J. M. Burt, E. Josyula, and I. D. Boyd, "Novel cartesian implementation of the direct simulation monte carlo method," *Journal of thermophysics and heat transfer*, vol. 26, no. 2, pp. 258–270, 2012.

[124] D. Baganoff and J. McDonald, "A collision-selection rule for a particle simulation method suited to vector computers," *Physics of Fluids A: Fluid Dynamics*, vol. 2, no. 7, pp. 1248–1259, 1990.

[125] J. F. Padilla and I. D. Boyd, "Assessment of gas-surface interaction models for computation of rarefied hypersonic flow," *Journal of Thermophysics and Heat Transfer*, vol. 23, no. 1, pp. 96–105, 2009.

[126] C. Virgile, A. Albert, and L. Julien, "Optimisation of a hybrid ns–dsmc methodology for continuous–rarefied jet flows," *Acta Astronautica*, vol. 195, pp. 295–308, 2022.

[127] M. Gad-el Hak, "The fluid mechanics of microdevices—the freeman scholar lecture," *Journal of Fluids Engineering*, vol. 121, no. 1, pp. 5–33, 1999.

[128] M. Liu, X. Zhang, G. Zhang, and Y. Chen, "Study on micronozzle flow and propulsion performance using dsmc and continuum methods," *Acta Mechanica Sinica*, vol. 22, no. 5, pp. 409–416, 2006.

[129] F. La Torre, S. Kenjereš, J.-L. Moerel, and C. Kleijn, "Hybrid simulations of rarefied supersonic gas flows in micro-nozzles," *Computers & fluids*, vol. 49, no. 1, pp. 312–322, 2011.

[130] K. M. Rafi, M. Deepu, and G. Rajesh, "Effect of heat transfer and geometry on micro-thruster performance," *International Journal of Thermal Sciences*, vol. 146, p. 106063, 2019.

[131] M. G. De Giorgi, D. Fontanarosa, and A. Ficarella, "Comparison of numerical predictions of the supersonic expansion inside micronozzles of micro–resistojets," in *MATEC Web of Conferences*, vol. 304. EDP Sciences, 2019, p. 02012.

[132] P. L. Bhatnagar, E. P. Gross, and M. Krook, "A model for collision processes in gases. i. small amplitude processes in charged and neutral one-component systems," *Physical review*, vol. 94, no. 3, p. 511, 1954.

[133] L. H. Holway Jr, "New statistical models for kinetic theory: methods of construction," *The physics of fluids*, vol. 9, no. 9, pp. 1658–1673, 1966.

[134] E. Shakhov, "Generalization of the krook kinetic relaxation equation," *Fluid dynamics*, vol. 3, no. 5, pp. 95–96, 1968.

[135] J. Burt and I. Boyd, "Evaluation of a particle method for the ellipsoidal statistical bhatnagar-gross-krook equation," in *44th AIAA Aerospace Sciences Meeting and Exhibit*, 2006, p. 989.

[136] M. Gallis and J. Torczynski, "The application of the bgk model in particle simulations," in *34th Thermophysics Conference*, 2000, p. 2360.

[137] R. Kumar, E. Titov, D. Levin, N. Gimelshein, and S. Gimelshein, "Assessment of bhatnagar-gross-krook approaches for near continuum regime nozzle flows," *AIAA journal*, vol. 48, no. 7, pp. 1531–1541, 2010.

[138] L. Mieussens, "Discrete-velocity models and numerical schemes for the boltzmann-bgk equation in plane and axisymmetric geometries," *Journal of Computational Physics*, vol. 162, no. 2, pp. 429–466, 2000.

[139] A. Shershnev and A. Kudryavtsev, "Kinetic simulation of near field of plume exhausting from a plane micronozzle," *Microfluidics and Nanofluidics*, vol. 19, no. 1, pp. 105–115, 2015.

[140] A. N. Kudryavtsev and A. A. Shershnev, "A numerical method for simulation of microflows by solving directly kinetic equations with weno schemes," *Journal of Scientific Computing*, vol. 57, no. 1, pp. 42–73, 2013.

[141] W. W. Liou and Y. Fang, *Microfluid mechanics: principles and modeling*. McGraw-Hill Education, 2006.

[142] R. Agarwal and K. Yun, "Burnett simulations of flows in microdevices," *The MEMS Handbook*, 2002.

[143] O. San, I. Bayraktar, and T. Bayraktar, "Size and expansion ratio analysis of micro nozzle gas flow," *International communications in heat and mass transfer*, vol. 36, no. 5, pp. 402–411, 2009.

[144] W. F. Louisos, A. A. Alexeenko, D. L. Hitt, and A. Zilic, "Design considerations for supersonic micronozzles," *International Journal of Manufacturing Research*, vol. 3, no. 1, pp. 80–113, 2008.

[145] K. Comeaux, D. Chapman, Ma, and R. Cormack, "An analysis of the burnett equations based on the second law of thermodynamics," in *33rd Aerospace sciences meeting and exhibit*, 1995, p. 415.

[146] M. Pfeiffer, A. Mirza, and P. Nizenkov, "Evaluation of particle-based continuum methods for a coupling with the direct simulation monte carlo method based on a nozzle expansion," *Physics of Fluids*, vol. 31, no. 7, p. 073601, 2019.

[147] F. Fei and P. Jenny, "A hybrid particle approach based on the unified stochastic particle bhatnagar-gross-krook and dsmc methods," *Journal of Computational Physics*, vol. 424, p. 109858, 2021.

[148] M. Pfeiffer, "A particle-based ellipsoidal statistical bhatnagar–gross–krook solver with variable weights for the simulation of large density gradients in micro-and nano-nozzles," *Physics of Fluids*, vol. 32, no. 11, p. 112009, 2020.

[149] W. F. Louisos and D. L. Hitt, "Numerical studies of supersonic flow in bell-shaped micronozzles," *Journal of Spacecraft and Rockets*, vol. 51, no. 2, pp. 491–500, 2014.

[150] I. Kim, J. Lee, M. Choi, and S. Kwon, "Optimum nozzle angle of a micro solid-propellant thruster," *Nanoscale and Microscale Thermophysical Engineering*, vol. 15, no. 3, pp. 165–178, 2011.

[151] I. Kim, S. Kwon, and J. Lee, "Effect of unsteadiness and nozzle asymmetry on thrust of a microthruster," *Nanoscale and Microscale Thermophysical Engineering*, vol. 16, no. 1, pp. 50–63, 2012.

[152] F. La Torre, "Gas flow in miniaturized nozzles for micro-thrusters," Ph.D. dissertation, Technische Universiteit Delft, 2011.

[153] L. T. Williams and M. F. Osborn, "Performance impacts of geometry and opeiting conditions on a low reynolds number micro-nozzle flow," *IEPC*, vol. 120, pp. 1–12, 2017.

[154] E. I. Sokolov and M. V. Chernyshov, "Optimization of micronozzle performance at zero ambient pressure," *Acta Astronautica*, vol. 150, pp. 97–104, 2018.

[155] J. M. Pearl, "Two-dimensional numerical study of micronozzle geometry," Ph.D. dissertation, University of Vermont, 2016.

[156] I. B. Sebastião and W. F. Santos, "Numerical simulation of heat transfer and pressure distributions in micronozzles with surface discontinuities on the divergent contour," *Computers & Fluids*, vol. 92, pp. 125–137, 2014.

[157] I. B. Sebastião and W. F. Santos, "Impact of surface discontinuities on flowfield structure of a micronozzle array," *Nanoscale and microscale thermophysical engineering*, vol. 18, no. 1, pp. 54–79, 2014.

[158] T. J. Croteau, "Micro-nozzle simulation and test for an electrothermal plasma thruster," Ph.D. dissertation, California Polytechnic State University, San Luis Obispo, 2018.

[159] D. T. Banuti, M. Grabe, and K. Hannemann, "Flow characteristics of monopropellant micro-scale planar nozzles," *Aerospace Science and Technology*, vol. 86, pp. 341–350, 2019.

[160] F. L. Torre, S. Kenjeres, C. R. Kleijn, and J.-L. P. Moerel, "Effects of wavy surface roughness on the performance of micronozzles," *Journal of Propulsion and Power*, vol. 26, no. 4, pp. 655–662, 2010.

[161] Y. Cai, Z. Liu, Q. Song, Z. Shi, and Y. Wan, "Fluid mechanics of internal flow with friction and cutting strategies for micronozzles," *International Journal of Mechanical Sciences*, vol. 100, pp. 41–49, 2015.

[162] Y. Cai, Z. Liu, and Z. Shi, "Effects of dimensional size and surface roughness on service performance for a micro laval nozzle," *Journal of Micromechanics and Microengineering*, vol. 27, no. 5, p. 055001, 2017.

[163] R. L. Bayt, "Fabrication, and testing of a mems-based micropropulsion system," Massachusetts Institute of Technology, FDRL TR 99-1, Ph. D. Thesis, Tech. Rep., 1999.

[164] J. Kujawa, D. Hitt, and G. Cretu, "Numerical simulation of supersonic flow in realistic mems nozzle geometries with heat loss," in *33rd AIAA Fluid Dynamics Conference and Exhibit*, 2003, p. 3585.

[165] W. Louisos and D. Hitt, "Heat transfer & viscous effects in 2d & 3d supersonic micro-nozzle flows," in *37th AIAA Fluid Dynamics Conference and Exhibit*, 2007, p. 3987.

[166] A. H. Hameed, R. Kafafy, W. Asrar, and M. Idres, "Improving the efficiency of micronozzle by heated sidewalls," in *AIP Conference Proceedings*, vol. 1440, no. 1. American Institute of Physics, 2012, pp. 409–417.

[167] B. Greenfield, W. Louisos, and D. Hitt, "Numerical simulations of multiphase flow in supersonic micro-nozzles," in *49th AIAA Aerospace Sciences Meeting including the New Horizons Forum and Aerospace Exposition*, 2011, p. 189.

[168] J. C. Pascoa, O. Teixeira, and G. Filipe, "A review of propulsion systems for cubesats," in *ASME International Mechanical Engineering Congress and Exposition*, vol. 52002. American Society of Mechanical Engineers, 2018, p. V001T03A039.

[169] A. Shershnev and A. Kudryavtsev, "Kinetic simulation of near field of plume exhausting from a plane micronozzle," *Microfluidics and Nanofluidics*, vol. 19, no. 1, pp. 105–115, 2015.

[170] K. H. Lee, S. N. Lee, M. J. Yu, S. K. Kim, and S. W. Baek, "Combined analysis of thruster plume behavior in rarefied region by preconditioned navier-stokes and dsmc methods," *Transactions of the Japan Society for Aeronautical and Space Sciences*, vol. 52, no. 177, pp. 135–143, 2009.

[171] K. H. Lee, "Satellite design verification study based on thruster plume flow impingement effects using parallel dsmc method," *Computers & Fluids*, vol. 173, pp. 88–92, 2018.

[172] M. Ivanov, A. Kudryavtsev, G. Markelov, P. Vashchenkov, D. Khotyanovsky, and A. Schmidt, "Numerical study of backflow for nozzle plumes expanding into vacuum," in *37th AIAA Thermophysics Conference*, 2004, p. 2687.

[173] M. Zhang, G. Cai, B. He, Z. Tang, and H. Zhou, "Experimental and numerical analysis of the heat flux characteristic of the plume of a 120-n thruster," *Science China Technological Sciences*, vol. 62, no. 10, pp. 1854–1860, 2019.

[174] M. Grabe, G. Dettlef, and K. Hannemann, "Comparison of computed free thruster plume expansion to experiments," in *Space Propulsion Conference*, 2014.

[175] K. H. Lee, "Numerical simulation on thermal and mass diffusion of mmh–nto bipropellant thruster plume flow using global kinetic reaction model," *Aerospace Science and Technology*, vol. 93, p. 104882, 2019.

[176] J. Chae and S. W. Baek, "Dsmc analysis of bipropellant thruster plume impingement on a geostationary spacecraft," *Journal of Mechanical Science and Technology*, vol. 30, no. 10, pp. 4621–4632, 2016.

[177] J. Wu, G. Cai, B. He, and Zhou, "Experimental and numerical investigations of vacuum plume interaction for dual hydrogen/oxygen thrusters," *Vacuum*, vol. 128, pp. 166–177, 2016.

[178] M. Grabe, G. Dettleff, and K. Hannemann, "Impact of nozzle separation on the plumes of two parallel thrusters," in *AIP Conference Proceedings*, vol. 1786, no. 1. AIP Publishing LLC, 2016, p. 170005.

[179] A. B. Weaver and I. D. Boyd, "Unsteady simulations of rocket plume expansions in geostationary earth orbit," *Journal of Spacecraft and Rockets*, vol. 54, no. 6, pp. 1258–1266, 2017.

[180] V. H. Reis and J. B. Fenn, "Separation of gas mixtures in supersonic jets," *The Journal of Chemical Physics*, vol. 39, no. 12, pp. 3240–3250, 1963.

[181] F. S. Sherman, "Hydrodynamical theory of diffusive separation of mixtures in a free jet," *The Physics of Fluids*, vol. 8, no. 5, pp. 773–779, 1965.

[182] S. Li, J. C. Day, J. J. Park, C. P. Cadou, and R. Ghodssi, "A fast-response microfluidic gas concentrating device for environmental sensing," *Sensors and Actuators A: Physical*, vol. 136, no. 1, pp. 69–79, 2007.

[183] V. Kosyanchuk and A. Yakunchikov, "Separation of a binary gas mixture outflowing into vacuum through a micronozzle," *Physics of Fluids*, vol. 33, no. 8, p. 082007, 2021.

[184] V. Kosyanchuk and A. Yakunchikov, "Aeroseparation of gas mixture during supersonic outflow in vacuumed reservoir with skimmer," *Vacuum*, vol. 199, p. 110959, 2022.

[185] Y. Krishna, X. Luo, and G. Magnotti, "One-dimensional interferometric rayleigh scattering velocimetry using a virtually imaged phased array," *Optics Letters*, vol. 46, no. 20, pp. 5252–5255, 2021.

[186] A. Kurganov and E. Tadmor, "New high-resolution central schemes for nonlinear conservation laws and convection–diffusion equations," *Journal of computational physics*, vol. 160, no. 1, pp. 241–282, 2000.

[187] J. G. Ehlers, S. Gordon, S. Heimel, and B. Mc Bride, "Thermodynamic properties to 6000 deg k for 210 substances involving the first 18 elements," Tech. Rep., 1963.

[188] W. Sutherland, "Lii. the viscosity of gases and molecular force," *The London, Edinburgh, and Dublin Philosophical Magazine and Journal of Science*, vol. 36, no. 223, pp. 507–531, 1893.

[189] G. B. Macpherson, N. Nordin, and H. G. Weller, "Particle tracking in unstructured, arbitrary polyhedral meshes for use in cfd and molecular dynamics," *Communications in Numerical Methods in Engineering*, vol. 25, no. 3, pp. 263–273, 2009.

[190] G. Bird, "Perception of numerical methods in rarefied gasdynamics," *Progress in Astronautics and Aeronautics*, vol. 117, pp. 211–226, 1989.

[191] C. Borgnakke and P. S. Larsen, "Statistical collision model for monte carlo simulation of polyatomic gas mixture," *Journal of computational Physics*, vol. 18, no. 4, pp. 405–420, 1975.

[192] C. White, M. K. Borg, T. J. Scanlon, S. M. Longshaw, B. John, D. R. Emerson, and J. M. Reese, "dsmcfoam+: An openfoam based direct simulation monte carlo solver," *Computer Physics Communications*, vol. 224, pp. 22–43, 2018.

[193] M. Wang and Z. Li, "Simulations for gas flows in microgeometries using the direct simulation monte carlo method," *International Journal of Heat and Fluid Flow*, vol. 25, no. 6, pp. 975–985, 2004.

[194] E. Piekos and K. Breuer, "Dsmc modeling of micromechanical devices," in *30th Thermophysics Conference*, 1995, p. 2089.

[195] J. Xu and C. Zhao, "Two-dimensional numerical simulations of shock waves in micro convergent–divergent nozzles," *International Journal of Heat and Mass Transfer*, vol. 50, no. 11-12, pp. 2434–2438, 2007.

[196] J. Pearl, W. Louisos, and D. Hitt, "Thrust calculation for low-reynolds-number micronozzles," *Journal of Spacecraft and Rockets*, vol. 54, no. 1, pp. 287–298, 2017.

[197] D. A. John and D. Anderson, "Modern compressible flow," 2003.

[198] G. Verma, *Autodesk fusion 360 black book*. BPB Publications, 2018.

[199] R. Gullberg, "Computational fluid dynamics in openfoam," *Report No. TKP*, vol. 4555, 2017.

[200] H. Davarzani, M. Marcoux, P. Costeseque, and M. Quintard, "Experimental measurement of the effective diffusion and thermodiffusion coefficients for binary gas mixture in porous media," *Chemical Engineering Science*, vol. 65, no. 18, pp. 5092–5104, 2010.

[201] M. K. Sukesan, “Effect of back pressure and divergent section contours on aerodynamic mixture separation using convergent–divergent micronozzles,” *AIP Advances*, vol. 12, no. 8, p. 085207, 2022.

[202] A. L. Jones and E. C. Milberger, “Separation of organic liquid mixtures by thermal diffusion,” *Industrial & Engineering Chemistry*, vol. 45, no. 12, pp. 2689–2696, 1953.

List of Publications

Journals

1. M.K. Sukesan, and S. R. Shine. "Micronozzle for satellite propulsion and mixture separation: a review." *Journal of Thermal Analysis and Calorimetry* (2023): 1-34, https://doi.org/10.1007/s10973-023-12227-9.

2. M. K. Sukesan, S R Shine, Geometry effects on flow characteristics of micro-scale planar nozzles, *Journal of Micromechanics and Microengineering*, 31(12),2021, https://doi.org/10.1088/1361-6439/ac2bac.

3. M. K. Sukesan, S R Shine, Effect of back pressure and divergent section contours on aerodynamic mixture separation using convergent–divergent micronozzles, *AIP Advances*, 12(8), 085207, https://doi.org/10.1063/5.0097772.

4. M K Sukesan, S R Shine, Performance of curved micronozzle used for gas separation, *Computational Thermal Sciences: An International Journal*,(manuscript no. CTS-49067), communicated.

Conferences

1. M. K. Sukesan,M.Kaswan, S. R. Shine, Thermal effects on flow through micronozzles with various geometries , *proceedings of the 26th national and 4th International Heat and Mass Transfer Conference* , IIT Madras,17th-20th December,2021.

2. M. K. Sukesan, S. R. Shine, Plume interaction study on a cluster of heated Micronozzles , *proceedings of the 26th national and 4th International Heat and Mass Transfer Conference* , IIT Madras,17th-20th December,2021.

3. M. K. Sukesan,A. Kumar, S. R. Shine, Effect of Divergence Angle, Carrier Gas and Back Pressure on Species Separation using Convergent Divergent Micro Nozzle ,

Proceedings of the 49th national and 9th international conference of Fluid Mechanics and Fluid Power, IIT Roorkee,14th-16th December,2022.

4. A. Kumar,M. K. Sukesan, S. R. Shine, Analysis of micro-nozzle flow using Navier Stokes and DSMC method and locating the separation plane based on modified Knudsen number , *Proceedings of the 49th national and 9th international conference of Fluid Mechanics and Fluid Power* , IIT Roorkee,14th-16th December,2022.

5. Manu K Sukesan, S R Shine, Geometry effects on flow characteristics of micro-scale planar nozzles, *ASSET 2023*, IIST Trivandrum, 13th February, 2023.

6. Manu K Sukesan, S R Shine, Effect of back pressure and divergent section contours on aerodynamic mixture separation using convergent-divergent micronozzle, *ASSET 2023*, IIST Trivandrum, 13th February, 2023.

About the Author

Manu K Sukesan obtained his Bachelor's degree in Mechanical Engineering from Mahatma Gandhi University in 2011, where he developed a solid foundation in the principles of mechanical systems and their applications. Recognizing his aptitude for advanced research, he pursued a Master's degree from the prestigious Indian Institute of Technology, Roorkee, which he successfully completed in 2014. After completing his Master's degree, he embarked on a professional journey as a safety engineer at DP World, a leading global port operator and logistics company. During his tenure, he gained valuable industry experience and honed his practical skills in ensuring operational safety and efficiency. In July 2019, he began his Ph.D. research under the supervision of Dr. Shine S R at the Aerospace Department, Indian Institute of Space Science and Technology, India. His research interests primarily revolve around computational fluid dynamics (CFD) and its application in space technology. Specifically, he focuses on the design, numerical analysis, and experimental investigation of micronozzle and MEMS micro propulsion systems for micro- and nanosatellite applications. His work aims to enhance the performance and maneuverability of these miniature propulsion systems, enabling more efficient and precise control of small satellites in space.

Appendix A

DSMC Details

A.1 Molecular Properties

The molecular properties used for the current DSMC simulations are given below

Molecule	mass (x10^{-27}kg)	d_{ref} (x10^{-10}m)	ω	α	T_{ref}(K)
N_2	46.5	4.17	0.74	1	273.15
O_2	53.12	4.07	0.77	1	273.15
Ar	66.3	4.11	0.81	1.4	273.15
He	6.65	2.3	0.66	1.26	273.15
Kr	139.1	4.76	0.8	1.32	273.15
SF_6	242.538	6.75	0.9	1.5	273.15